공학박사학위논문

Development of efficient Thomson scattering diagnostic system on VEST

VEST 장치의 톰슨 산란 진단 장치 개발

2019년 2월

서울대학교 대학원

에너지시스템공학부

김 영 기

Development of efficient Thomson scattering diagnostic system on VEST

VEST 장치의 톰슨 산란 진단 장치 개발

지도 교수 나용수

이 논문을 공학박사 학위논문으로 제출함
2018 년 10 월

서울대학교 대학원
에너지시스템공학부
김영기

김영기의 박사 학위논문을 인준함
2019 년 1 월

위원장 황용석 (인)
부위원장 나용수 (인)
위원 정경재 (인)
위원 김영철 (인)
위원 이종하 (인)

Abstract

Development of efficient Thomson scattering diagnostic system on VEST

Young-Gi Kim
Department of Energy System Engineering
(Fusion & Plasma Engineering)
The Graduate School
Seoul National University

A Thomson scattering (TS) diagnostic system was developed to measure the plasma of the VEST device, and the electron temperature and density of Ohmic plasma were measured. VEST is the first spherical torus manufactured in Korea and it is studied to generate high-performance plasma through various plasma start-up scenarios as well as heating and current drive. In order to support the researches, heating systems such as electron Bernstein wave (EBW), lower hybrid fast wave (LHFW), and neutral beam injection (NBI) and the diagnostic systems such as TS system, spectroscopy, and multi-channel interferometer have been developed. The main purpose of this dissertation is investigation of the design, development, and optimization of the TS system that provide the reliable electron temperature and density, which is basic and important information for analyzing heating efficiencies and plasma transports in VEST.

The TS system measures the electron temperature from the Doppler broadening

of the scattered light by the free electrons inside the plasma with utilizing the high-power pulse laser. In addition, the electron density can be determined through absolute calibration of the system. It does not affect the target plasmas, in principle, unlike Langmuir probes or other beam diagnostics. Furthermore, because of its high spatial resolution, it is adopted as an essential diagnostics in tokamaks around the world.

On VEST, the Thomson scattering system that consists of a laser injection system, a collecting optics system, and a polychromator is carefully designed and developed. It employed a laser with the energy of 0.85 J and a budget of about 60 million won, which are relatively low compared to the general Thomson scattering diagnostic systems. Therefore, methods to maximize the performance of the each part are explored in order to increase the signal level, while simultaneously minimizing noises to obtain a sufficient signal-to-noise ratio. In the laser injection system, the fundamental wavelength of Nd: YAG laser, 1064 nm, is used to avoid the energy loss during the frequency doubling. The beam path was designed so that the Rayleigh range of the Gaussian beam is formed around the measurement target points, thereby improving the efficiencies of the collecting optics. There was trade-off between the collecting optics and the polychromator. Compromises in performance were necessary to meet the requirements within a limited budget. The collecting optics was developed with the priority, because the small number of collected photons cannot be analyzed even if the wavelength resolution of the polychromator is excellent. It was developed to maximize the collecting solid angle in the VEST vacuum vessel with minimal aberrations. It consists of two large aspheric lenses with an effective diameter of 109 mm and optical fibers with a core diameter of 1500 μm and a numerical aperture of 0.39. It maintains collecting performance in the major radius of 0.23-0.5 m where the product of the collecting solid angle and the scattering length is about 300 mm msr. The optical transmission part of the polychromator was made based on the polychromator of KSTAR in National Fusion Research Institute. However, the band pass filters were designed to be suitable for the measurement of the temperature range of 1-200 eV. In order to reduce the budget, low cost commercial filters with low transmittance, low blocking rate, and poor wavelength resolution due to overlapping of pass band were utilized. For reducing the stray light that passes through the filters due to the low blocking ratio, the components for the stray light reduction were developed and installed inside and outside the VEST vacuum vessel. It lowered the stray light intensity to about 1/100 of the initial value.

The Rayleigh scattering measurement was performed by changing the pressure of nitrogen for the absolute calibration of the system. Moreover, a circuit for the time synchronization between the VEST control system and the TS diagnostic system was developed. The TS signal were measured where the electron density is higher than 2×10^{18} m^{-3}. The signals are analyzed by Bayesian method to determine the electron temperature and density. In case of the electron density was lower than 2×10^{18} m^{-3}, accumulation of the scattering signals was required to obtain a sufficient signal-to-noise ratio (SNR). The time variation of the electron temperature and density measured by TS diagnostic system from repetitive experiments was compared with the tendency of the stored energy, which is calculated by the diamagnetic loop measurement with the equilibrium analysis.

TS system on VEST is expected to improve the performance through partial

upgrades because the main parts are accessible and easy to modify. First, when a burst laser is started to operate, the time variation of the electron temperature and density can be measured within a single discharge, and further increase in SNR is expected. Then, the introduction of a fast digitizer will follow to measure the burst laser signal. In addition, use of an optical fiber bundle could help signal level increase. As the number of polychromators increases, the radial profile will be measured.

Keywords: Thomson scattering, Thomson scattering diagnostic system, Plasma diagnostics, Spherical Torus, VEST
Student Number: 2012-20992

Contents

List of Tables

List of Figures

Chapter 1. Introduction

One of the important issues of realization of the nuclear power fusion plant is development of accurate plasma control systems and diagnostic system. Since the theories of plasma physics are still developing, observation of the plasmas in devices of various scale is essential to improve the hypothesis. The objective of the diagnostics is obtaining desired information from the practical measurement by developing proper tools. In order to make a reliable diagnostic system, not only a deep understanding of the principles of the diagnostic method, but also the design and development of the device are necessary.

Various properties can be measured from the plasmas, including magnetic fields and flux, electric potentials, light intensities from emissions or scatterings, refractive index, and so on. In this dissertation, as a part of light intensity measurement, development of Thomson scattering diagnostic system on VEST device is descripted in detail.

1.1. Versatile Experiment Spherical Torus

Versatile experiment spherical torus (VEST) is a compact spherical torus that has been constructed for studying the innovative start-up and no-inductive current drive methods [1, 2]. The heating and current drive systems including the electron Bernstein wave (EBW), lower hybrid fast wave (LHFW) current drive, and neutral beam injection (NBI) are under preparation for high beta operation in VEST. In addition, stable operation scenarios with high beta plasma are planned for controlling the safety factor profile with additional heating and current drive systems. For successful high beta experiments, the accurate plasma properties are important to understand and analyze the plasma state.

The plasma diagnostics have been developed on VEST to obtain information from the plasmas [3, 4]. At the initial phase, the magnetic diagnostics including magnetic probes, flux loops, and Rogowski coils that are not only the simplest, but also useful diagnostics are designed and fabricated to measure the magnetic field inside and outside a vacuum vessel. Additionally, basic optical diagnostics such as a fast camera and line monitoring systems and probe systems such as triple Langmuir probes and Mach probes are installed and operated. However, until now days, experiments on VEST are usually analyzed by using data obtained by such basic diagnostics. The electron temperature and density of the ions or electrons at the core region have not been measured yet in the ohmic discharges due to the lack of advanced diagnostic system such as the Thomson scattering system, a charge exchange spectroscopy, or an interferometer.

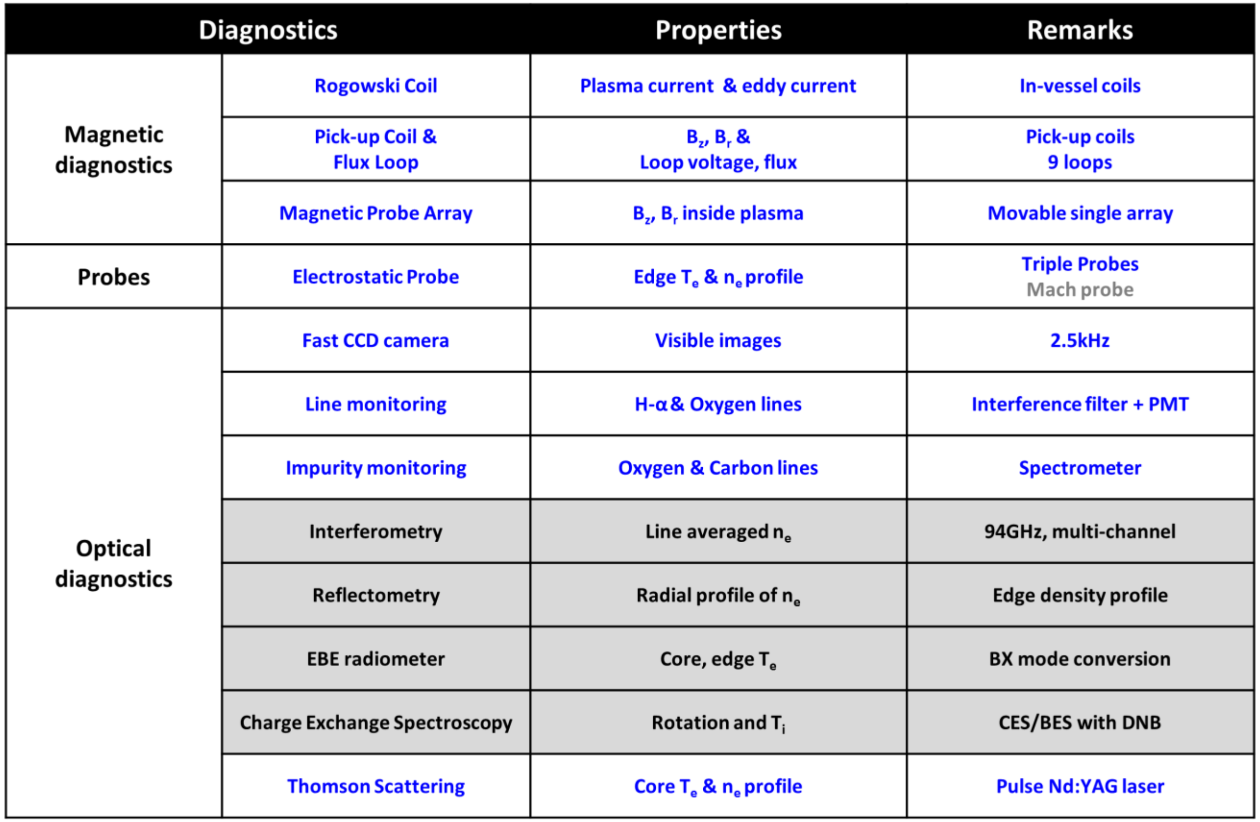

Diagnostics		Properties	Remarks
Magnetic diagnostics	Rogowski Coil	Plasma current & eddy current	In-vessel coils
	Pick-up Coil & Flux Loop	B_z, B_r & Loop voltage, flux	Pick-up coils 9 loops
	Magnetic Probe Array	B_z, B_r inside plasma	Movable single array
Probes	Electrostatic Probe	Edge T_e & n_e profile	Triple Probes Mach probe
Optical diagnostics	Fast CCD camera	Visible images	2.5kHz
	Line monitoring	H-α & Oxygen lines	Interference filter + PMT
	Impurity monitoring	Oxygen & Carbon lines	Spectrometer
	Interferometry	Line averaged n_e	94GHz, multi-channel
	Reflectometry	Radial profile of n_e	Edge density profile
	EBE radiometer	Core, edge T_e	BX mode conversion
	Charge Exchange Spectroscopy	Rotation and T_i	CES/BES with DNB
	Thomson Scattering	Core T_e & n_e profile	Pulse Nd:YAG laser

Figure 1.1 Overview of the diagnostics on VEST. Shaded diagnostics are under development state.

1.2. Thomson scattering

Scatterings of incident waves by charged particles can be roughly classified into four types depending on whether it is elastic collision and whether it happens by a free charged particle. Firstly, Rayleigh scattering and Raman scattering are the scattering of photons by an atom or molecule. Rayleigh and Raman scattering can be divided again by if the scattering is elastic or inelastic, respectively. Similarly, Thomson scattering and Compton scattering are the scattering of incident photons by a free charged particles. Thomson scattering is the elastic scattering and Compton scattering is the inelastic scattering. Note that, strictly speaking, Thomson scattering is the low energy limit of Compton scattering.

By comparing the wavelength of the incident wave with the Debye length of the plasma, Thomson scattering could be divided into two types: Collective Thomson scattering and incoherent Thomson scattering. In plasma diagnostics, the former is used to measure the ion properties and the latter is applied to measure the electron temperature and density. Generally, wavelength of the infrared laser is much shorter than the Debye length of the fusion plasmas.

1.2.1. Electric and magnetic fields of a moving electron

Electric field and magnetic field from a moving charged particle can be directly calculated by using Jefimenko's equation. However, since it is known as complicated, so the Lienard-Wichert potentials are generally used to get the field of the point charge [5]. Considering the configuration of Figure 1.2, the fields measured at the position $\vec{r}$ at time t is information of the charge at $\vec{w}(t_r)$, where t_r is the retarded time which can be found from following equations.

$$\vec{R} = \vec{r} - \vec{w}(t_r)\ . \tag{1.1}$$

$$\left|\vec{R}\right| = \left|\vec{r} - \vec{w}(t_r)\right| = c(t - t_r) = c\Delta t\ , \tag{1.2}$$

where c is the speed of light.

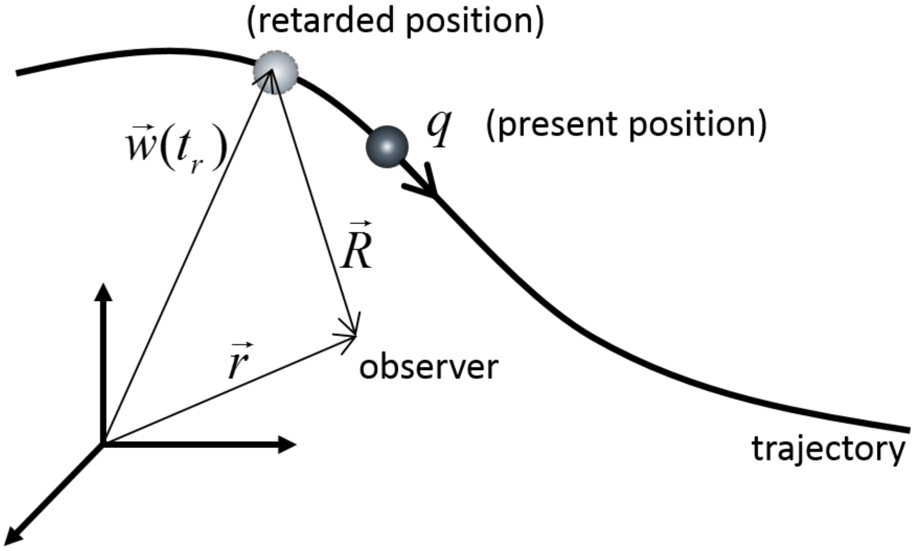

Figure 1.2 Trajectory of a moving charged particle

Since the electric potential $V(\vec{r},t)$ is determined at $\vec{w}(t), t_r,$ and a volume $d\tau'$, it is expressed as follows

$$V(\vec{r},t) = \frac{1}{4\pi\varepsilon_0}\int \frac{\rho(\vec{r},t_r)}{R}\,d\tau'\ . \tag{1.3}$$

Because of the geometrical effect, an approaching object appears longer and an object going away from the observer seems shorter. From Figure 1.3, the factor that should be considered is $(1-\hat{R}\cdot\vec{v}/c)^{-1}$, where $\hat{R}$ is the unit vector of direction of $\vec{R}$ and $\vec{v}$ is the velocity of the charged particle at t_r.

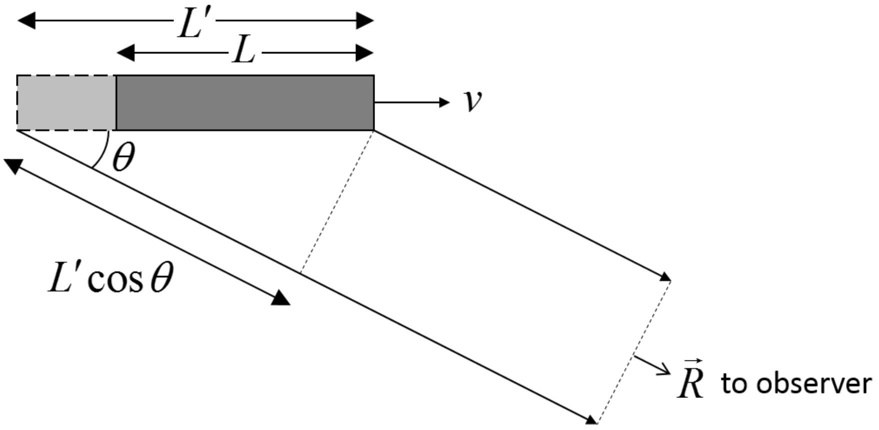

Figure 1.3 Observer sees the light from the front side with the light from the back started earlier due to the optical path length difference.

The time required to compensate the path length difference is

$$\Delta t = \frac{L'-L}{v} = \frac{L'\cos\theta}{c}. \tag{1.4}$$

Then,

$$L' = \frac{L}{1-(v/c)\cos\theta}. \tag{1.5}$$

This affects to the direction of motion, the volume is changed into

$$d\tau' = \frac{d\tau}{1-(v/c)\cos\theta} = \frac{d\tau}{1-\hat{R}\cdot\vec{v}/c}. \tag{1.6}$$

Therefore,

$$V(\vec{r},t)=\frac{1}{4\pi\varepsilon_0}\frac{qc}{Rc-\vec{R}\cdot\vec{v}}. \tag{1.7}$$

Similarly, the vector potential of the moving charged particle is

$$\vec{A}(\vec{r},t)=\frac{\mu_0}{4\pi}\frac{qc\vec{v}}{Rc-\vec{R}\cdot\vec{v}}=\frac{\vec{v}}{c^2}V(\vec{r},t). \tag{1.8}$$

Eq. (1.7) and Eq. (1.8) are Lienard-Wiechert potentials.

From the potentials, the electric field and magnetic field of the moving point charge can be calculated. Recall $\vec{R}=\vec{r}-\vec{w}(t_r)$, $R=\left|\vec{R}\right|=|\vec{r}-\vec{w}(t_r)|=c(t-t_r)$, $\vec{v}=\dot{\vec{w}}(t_r)$, and t_r is the function of t and $\vec{r}$. Firstly, calculation of the electric field is as follows,

$$\nabla V=\frac{qc}{4\pi\varepsilon_0}\frac{-1}{(Rc-\vec{R}\cdot\vec{v})^2}\nabla(Rc-\hat{R}\cdot\vec{v}). \tag{1.9}$$

$$\nabla(Rc-\hat{R}\cdot\vec{v})=c\nabla R-\left[(\vec{R}\cdot\nabla)\vec{v}+(\vec{v}\cdot\nabla)\vec{R}+\vec{R}\times(\nabla\times\vec{v})+\vec{v}\times(\nabla\times\vec{R})\right]. \tag{1.10}$$

Putting following relations into each term of Eq. (1.10),

$$c\nabla R=c\nabla(c(t-t_r))=-c^2\nabla t_r,$$

$$(\vec{R}\cdot\nabla)\vec{v}=\vec{a}(\vec{R}\cdot\nabla t_r),$$

$$(\vec{v}\cdot\nabla)\vec{R}=(\vec{v}\cdot\nabla)\vec{r}-(\vec{v}\cdot\nabla)\vec{w}=\vec{v}-\vec{v}(\vec{v}\cdot\nabla t_r),$$

$$\vec{R}\times(\nabla\times\vec{v})=-\left[\vec{a}(\vec{R}\cdot\nabla t_r)-\nabla t_r(\vec{R}\cdot\vec{a})\right],$$

$$\vec{v}\times(\nabla\times\vec{R})=\vec{v}\times(\vec{v}\times\nabla t_r)=\left[\vec{v}(\vec{v}\cdot\nabla t_r)-\nabla t_r(v^2)\right].$$

Eq. (1.10) is simplified as follows

$$\nabla(Rc-\hat{R}\cdot\vec{v})=-\left[\vec{v}+(c^2-v^2+\vec{R}\cdot\vec{a})\nabla t_r\right]. \tag{1.11}$$

Now, ∇t_r is obtained from following equations. Since $R=c(t-t_r)$,

$$-c\nabla t_r=\nabla R=\nabla\sqrt{\vec{R}\cdot\vec{R}}=\frac{1}{2\sqrt{\vec{R}\cdot\vec{R}}}\nabla(\vec{R}\cdot\vec{R})=\frac{2}{2R}\left[(\vec{R}\cdot\nabla)\vec{R}+\vec{R}\times(\nabla\times\vec{R})\right]$$

$$=\frac{1}{2\sqrt{\vec{R}\cdot\vec{R}}}\nabla(\vec{R}\cdot\vec{R})$$

$$=\frac{2}{2R}\left[(\vec{R}\cdot\nabla)\vec{R}+\vec{R}\times(\nabla\times\vec{R})\right].$$

Each term can be represented as

$$(\vec{R}\cdot\nabla)\vec{R}=(\vec{R}\cdot\nabla)\vec{r}-(\vec{R}\cdot\nabla)\vec{w}=\vec{R}-\vec{v}(\vec{R}\cdot\nabla t_r),$$

$$\vec{R}\times(\nabla\times\vec{R})=\vec{R}\times(\vec{v}\times\nabla t_r)=\vec{v}(\vec{R}\cdot\nabla t_r)-\nabla t_r(\vec{R}\cdot\vec{v}).$$

Therefore,

$$-c\nabla t_r=\frac{1}{R}\left[\vec{R}-(\vec{R}\cdot\vec{v})\nabla t_r\right],$$

$$(Rc-\vec{R}\cdot\vec{v})\nabla t_r=-\vec{R}.$$

Following relation is obtained.

$$\nabla t_r=\frac{-\vec{R}}{(Rc-\vec{R}\cdot\vec{v})}. \tag{1.12}$$

Therefore, gradient of the electric potential is

$$\nabla V=\frac{qc}{4\pi\varepsilon_0}\frac{1}{(Rc-\vec{R}\cdot\vec{v})^2}\left[\vec{v}+(c^2-v^2+\vec{R}\cdot\vec{a})\left(\frac{-\vec{R}}{Rc-\vec{R}\cdot\vec{v}}\right)\right]$$

$$=\frac{qc}{4\pi\varepsilon_0}\frac{1}{(Rc-\vec{R}\cdot\vec{v})^3}\left[(Rc-\vec{R}\cdot\vec{v})\vec{v}-(c^2-v^2+\vec{R}\cdot\vec{a})\vec{R}\right]. \tag{1.13}$$

Secondly, the time derivative of the vector potential is obtained as follows

$$\frac{\partial\vec{A}}{\partial t}=\frac{\partial\vec{A}}{\partial t}\left(\frac{\vec{v}}{c^2}V\right)=\frac{1}{c^2}\left(\frac{\partial\vec{v}}{\partial t}V+\vec{v}\frac{\partial V}{\partial t}\right)=\frac{1}{c^2}\left(\frac{\partial\vec{v}}{\partial t_r}\frac{\partial t_r}{\partial t}V+\vec{v}\frac{\partial V}{\partial t}\right)$$

$$=\frac{1}{c^2}\left[\vec{a}\frac{\partial t_r}{\partial t}\frac{1}{4\pi\varepsilon_0}\frac{qc}{\vec{R}\cdot\vec{u}}+\vec{v}\frac{1}{4\pi\varepsilon_0}\frac{-qc}{(\vec{R}\cdot\vec{u})^2}\frac{\partial}{\partial t}(Rc-\vec{R}\cdot\vec{v})\right]$$

$$=\frac{1}{c^2}\frac{qc}{4\pi\varepsilon_0}\left[\frac{\vec{a}}{\vec{R}\cdot\vec{u}}\frac{\partial t_r}{\partial t}-\frac{\vec{v}}{(\vec{R}\cdot\vec{u})^2}\left(c\frac{\partial R}{\partial t}-\frac{\partial\vec{R}}{\partial t}\cdot\vec{v}-\vec{R}\cdot\frac{\partial\vec{v}}{\partial t}\right)\right].$$

$$\frac{\partial\vec{A}}{\partial t}=\frac{qc}{4\pi\varepsilon_0}\frac{1}{(Rc-\vec{R}\cdot\vec{v})^3}\left[(Rc-\vec{R}\cdot\vec{v})(-\vec{v}+\frac{R\vec{a}}{c})+(c^2-v^2+\vec{R}\cdot\vec{a})\frac{\vec{v}}{c}R\right]. \tag{1.14}$$

Lastly, Eq. (1.13) and Eq. (1.14) are summarized into the electric field as follows

$$\vec{E}=-\nabla V-\frac{\partial\vec{A}}{\partial t}=-\frac{q}{4\pi\varepsilon_0}\frac{1}{(Rc-\vec{R}\cdot\vec{v})^3}\left[(Rc-\vec{R}\cdot\vec{v})(-\vec{v}+\frac{R\vec{a}}{c})+(c^2-v^2+\vec{R}\cdot\vec{a})\left(-\vec{R}+\frac{\vec{v}}{c}R\right)\right]$$

$$=\frac{q}{4\pi\varepsilon_0}\frac{R}{(Rc-\vec{R}\cdot\vec{v})^3}\left[(c^2-v^2)\vec{u}+\vec{R}\times(\vec{u}\times\vec{a})\right]. \tag{1.15}$$

By using the similar vector calculations, the magnetic field of the moving charged particle is obtained. And it can be expressed by electric field as following below,

$$\vec{B} = \nabla \times \vec{A} = \frac{1}{c^2}\left[V(\nabla \times \vec{v}) - \vec{v} \times \nabla V\right] = \frac{1}{c}\frac{q}{4\pi\varepsilon_0}\frac{R}{(Rc - \vec{R}\cdot\vec{v})^3}\hat{R}\times\left[(c^2 - v^2)\vec{u} + \vec{R}\times(\vec{u}\times\vec{a})\right]$$

$$= \frac{1}{c}\hat{R}\times\vec{E}(\vec{r},t)\,. \tag{1.16}$$

Here, second terms of $\vec{E}$ and $\vec{B}$ that proportional to R^{-1} remain in the far field, so they are called the radiation field or the acceleration field. The detailed derivation can be found in [5].

1.2.2. Radiation power and cross section

The radiation power of the moving point charge is calculated by the Poynting vector.

$$\vec{S} = \frac{1}{\mu_0}(\vec{E}\times\vec{B}) = \frac{1}{\mu_0 c}\left(\vec{E}\times(\hat{R}\times\vec{E})\right) = \frac{1}{\mu_0 c}\left[E^2\hat{R} - (\hat{R}\cdot\vec{E})\vec{E}\right]. \tag{1.17}$$

However, at the far field, the only radiation field terms of $\vec{E}$ and $\vec{B}$ represent the radiation, and the other terms go to zero as integrating them at the infinitely large sphere. Then the radiation field is considered as follows,

$$\vec{E}_{rad} = \frac{q}{4\pi\varepsilon_0}\frac{R}{(\vec{R}\cdot\vec{u})^3}\left[\vec{R}\times(\vec{u}\times\vec{a})\right], \tag{1.18}$$

where $\vec{u} = c\hat{R} - \vec{v}$, and $\vec{a}$ is the acceleration of the particle. Since $\vec{E}$ is always perpendicular to $\vec{R}$,

$$\vec{S}_{rad} = \frac{1}{\mu_0 c}E_{rad}^2\hat{R}\,. \tag{1.19}$$

For $v \ll c,\ u = c\hat{R} - \vec{v} \cong c\hat{R}$

$$\vec{S}_{rad} = \frac{1}{\mu_0 c}\left(\frac{q}{4\pi\varepsilon_0 c^2 R}\left[(\hat{R}\cdot\vec{a})\hat{R}-\vec{a}\right]\right)^2 \hat{R}$$

$$= \frac{\mu_0 q^2}{16\pi^2 c R^2}\left[a^2 - (\hat{R}\cdot\vec{a})^2\right]\hat{R}$$

$$= \frac{\mu_0 q^2 a^2}{16\pi^2 c R^2}\left[1-\cos^2\theta\right]\hat{R}$$

$$= \frac{\mu_0 q^2 a^2}{16\pi^2 c}\frac{\sin^2\theta}{R^2}\hat{R}. \tag{1.20}$$

where θ is the angle between the direction of the electric field and the direction of the outgoing radiation. It hold to good approximation as long as $v \ll c$ [5]. The radiation power per unit solid angle is obtained from the Poynting vector as following below,

$$dP_{rad} = \vec{S}_{rad}\cdot d\vec{A} = \left(\frac{\mu_0 q^2 a^2}{16\pi^2 c}\frac{\sin^2\theta}{R^2}\hat{R}\right)\cdot \hat{R}R^2 d\Omega, \tag{1.21}$$

$$\frac{dP_{rad}}{d\Omega} = \frac{\mu_0 q^2 a^2}{16\pi^2 c}\sin^2\theta. \tag{1.22}$$

The cross section can be expressed as below

$$\sigma\ [\mathrm{m}^2] = \frac{(\text{Re-radiation power [J/s]})}{(\text{Flux of incident wave [J/m}^3\cdot\text{m/s]})}. \tag{1.23}$$

Therefore,

$$\frac{d\sigma}{d\Omega} = \frac{dP_{rad}/d\Omega}{u\cdot c}, \tag{1.24}$$

where u is the energy density of the incident wave. If the external electric field is expressed as $\vec{E} = E_0 \sin\left(\vec{k}\cdot\vec{r} - wt\right)\hat{e}$, the acceleration of the charged particle is obtained from the equation of the motion.

$$m\frac{\partial^2\vec{r}}{\partial t^2} = q\vec{E} \,. \tag{1.25}$$

$$\vec{a} = \frac{\partial^2\vec{r}}{\partial t^2} = \frac{qE_0}{m}\sin(\vec{k}\cdot\vec{r} - wt)\hat{e} \,. \tag{1.26}$$

Then, the time average of a^2 is

$$< a^2 >= \left(\frac{qE_0}{m}\right)^2 < \sin^2(\vec{k}\cdot\vec{r} - wt) >= \frac{q^2E_0^2}{2m^2} \,. \tag{1.27}$$

Hence, the time averaged radiation power per unit solid angle is represented as follows

$$\left\langle \frac{dP_{rad}}{d\Omega} \right\rangle = \frac{q^2}{16\pi^2c^3\varepsilon_0}\left(\frac{q^2E^2}{2m^2}\right)\sin^2\theta = \left(\frac{q^2}{4\pi\varepsilon_0 mc^2}\right)^2\left(\frac{\varepsilon_0 E_0^2}{2}c\right)\sin^2\theta \,. \tag{1.28}$$

The energy density of the incident wave is obtained as following,

$$u = \frac{1}{2}\varepsilon_0E^2 + \frac{1}{2\mu_0}B^2 = \frac{1}{2}\varepsilon_0E^2 + \frac{1}{2\mu_0c^2}E^2 = \varepsilon_0E^2 \,,$$

And, the mean energy flux of the incident wave can be written as

$$\langle u\rangle = \varepsilon_0\left\langle E^2\right\rangle = \frac{\varepsilon_0E_0^2}{2} \,. \tag{1.29}$$

Now, from Eq. (1.23), if the charge particle is the electron, $q = e$ and $m = m_e$, the differential cross section becomes

$$\frac{d\sigma}{d\Omega} = \left(\frac{q^2}{4\pi\varepsilon_0 mc^2}\right)^2 \sin^2\theta = r_e^2\sin^2\theta \,, \tag{1.30}$$

where, $r_e = \frac{q^2}{4\pi\varepsilon_0 m_e c^2}$ is the classical electron radius. If observers measure moving electrons in the direction of the electric field ($\phi = 0$), no scattered light will be collected. However, in case of the right angle about the electric field ($\phi = \pi/2$) the maximum intensity of the scattered light will be measured. The total cross section is obtained by integration of the differential cross section over a unit sphere. Integration with respect to the total solid angle gives the total cross section,

$$\sigma = \int_{4\pi} \frac{d\sigma}{d\Omega} d\Omega = r_e^2 \int_0^{2\pi} \int_0^{\pi} \sin^2\theta \sin\theta d\theta d\phi = \frac{8}{3}\pi r_e^2 = 6.65\times10^{-29}\,\mathrm{m}^2 . \quad (1.31)$$

1.2.3. Incoherent Thomson scattering

When Debye length is much longer than the wavelength of the incident wave as depicted in Figure 1.4, the scattered photons from a Debye sphere are randomly distributed. It is called incoherent scattering or non-collective scattering. The condition is represented by Eq. (1.32) [6, 7, 8].

$$\alpha = \frac{1}{k\lambda_{De}} << 1 . \quad (1.32)$$

The α is called Salpeter parameter, k is a wavenumber of the incident wave, and λ_{De} is a Debye length of electrons expressed as

$$\lambda_{De} = \sqrt{\frac{\varepsilon_0 T_e}{e n_e}} , \quad (1.33)$$

where ϵ_0, T_e, e, and n_e are the permittivity of free space, the electron temperature in the unit of *eV*, the elementary charge, and the electron density, respectively.

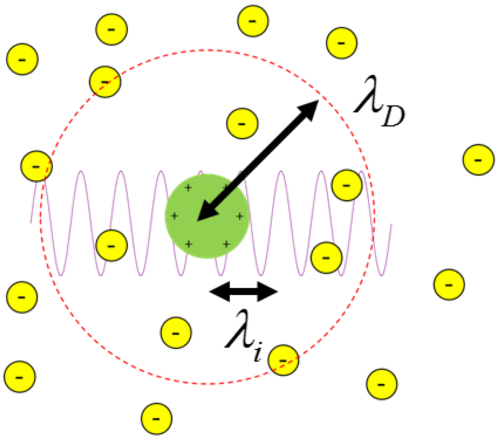

Figure 1.4 Schematic of the condition for incoherent Thomson scattering.

1.2.4. Relativistic Thomson scattering spectrum

The mechanism of the Thomson scattering is that the free electrons are accelerated by the electric field of the incident wave, and the wave of the same frequency is emitted from the oscillation of the electron. The origin of the spectral broadening of the Thomson scattering in this mechanism is the Doppler broadening from the electrons. Since the energy is conserved during the scattering, the frequency and the wavenumber of the incident and scattered waves are same as depicted in Figure 1.5. The spectral broadening measured by an observer reflects that the electron velocity parallel to the $\vec{k}$ direction.

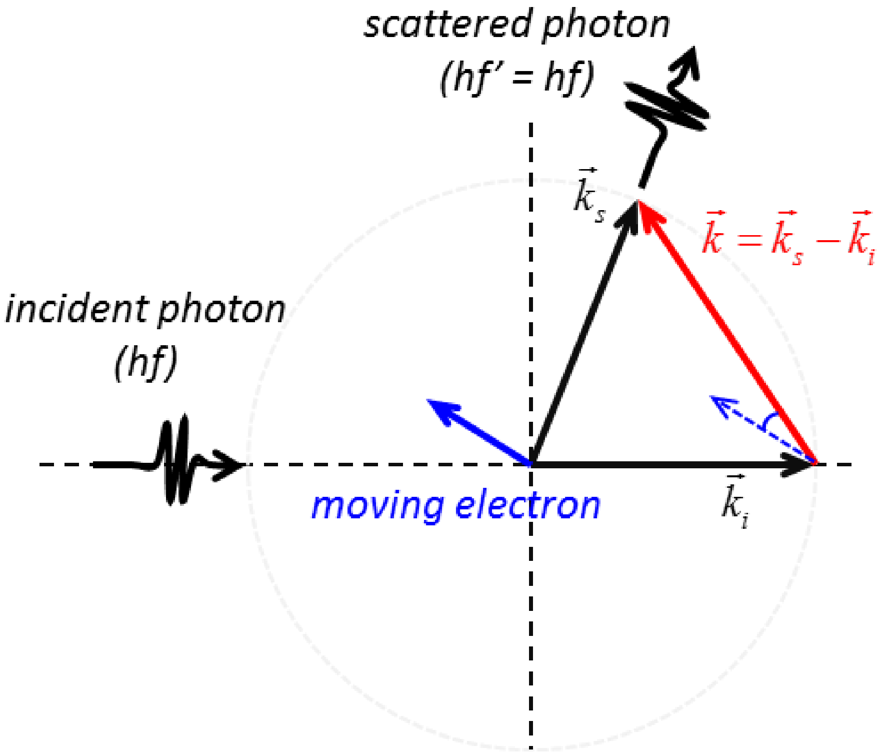

Figure 1.5 Schematic vector plot of Thomson scattering. Doppler broadening of the electron reflects the moving direction parallel to the $\vec{k}$ vector.

In plasma measurement, there are fast electron closed to the speed of light in electron velocity distribution, therefore, the relativistic effect should be considered to find the accurate Thomson scattering spectrum. The relativistic effect is came from the relativistic aberration; the rays of the scattered light that reach the observer are tilted towards the direction of the electron motion [9]. Consequently, it distorts the spectrum of the Thomson scattering, blue shift for instance. The relativistic effect is usually considered at the electron temperature higher than 500 eV, it can also be used for analysis of the low temperature plasmas to increase the accuracy of analysis of low temperature plasmas. The second order approximate relativistic spectra are computed by Matoba [10] is adopted.

$$S_N(\varepsilon) = \left(\frac{\alpha}{\pi}\right)^{1/2} \frac{1}{\sqrt{2(1-\cos\theta)}} \exp\left\{\frac{-\alpha\varepsilon^2}{2(1-\cos\theta)}\right\}. \tag{1.34}$$

$$\begin{aligned} A(\varepsilon) = {} & 1 - \frac{7}{2}\varepsilon + \frac{\alpha\varepsilon^3}{2(1-\cos\theta)} \\ & - \frac{1}{8\alpha}\left(\frac{39}{4} - 5\cos\theta\right) + \frac{1}{8}\left(29 + \frac{5}{1-\cos\theta}\right)\varepsilon^2 \\ & - \frac{1}{16(1-\cos\theta)}\left(28 - \frac{1}{1-\cos\theta}\right)\alpha\varepsilon^4 + \frac{\alpha^2\varepsilon^6}{8(1-\cos\theta)^2}. \end{aligned} \tag{1.35}$$

$$S_R^{(2)}(\varepsilon) = S_N(\varepsilon)A(\varepsilon). \tag{1.36}$$

$$\alpha = \frac{m_e c^2}{2T_e}. \tag{1.37}$$

$$\varepsilon = \frac{\lambda}{\lambda_0}. \tag{1.38}$$

Eq. (1.34) is the nonrelativistic spectral density function, and Eq. (1.36) is the second order approximate relativistic spectral density function. Here, m_e is the static electron mass and c is the speed of light. ϵ indicates the normalized wavelength divided by the wavelength of the incident wave. θ is angle between directions of the incident wave and the scattered wave, called scattering angle.

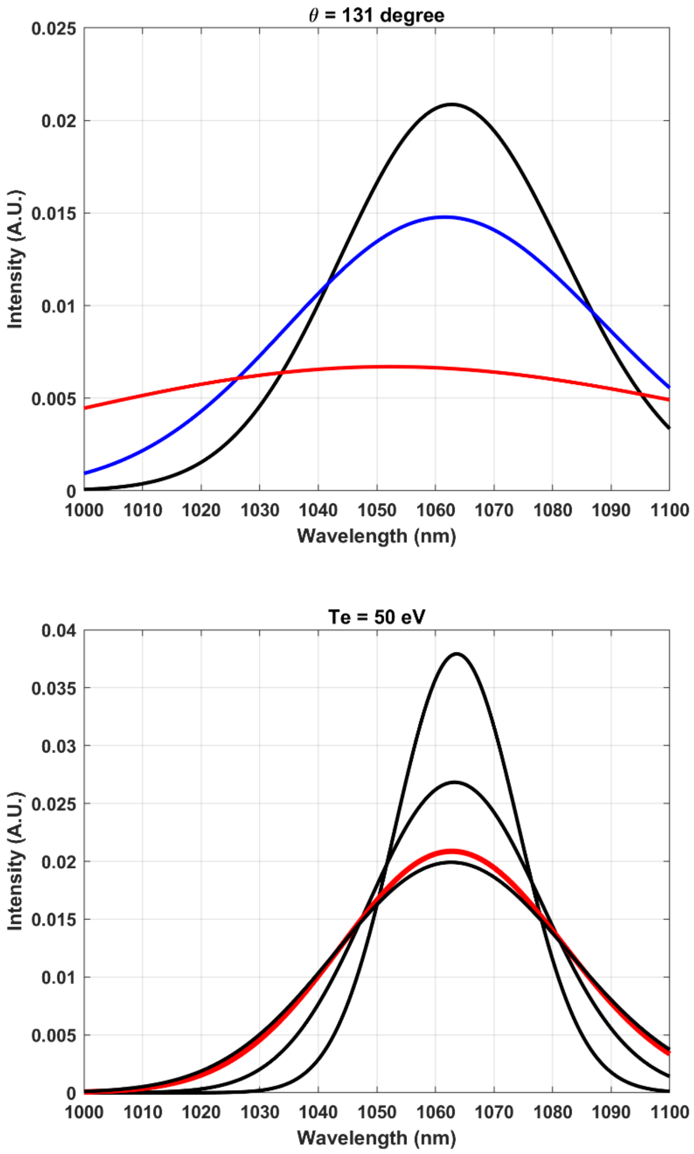

Figure 1.6 Relativistic Thomson scattering spectra (top) as a function of the electron temperature with the fixed scattering angle and (bottom) as a function of the scattering angle with the fixed electron temperature.

As seen in Figure 1.6, the spectrum has dependency on both the electron temperature and the scattering angle. Firstly, it can be seen in the left figure that the broader spectrum is appeared as the temperature increases. In addition, it should be noted that the central wavelength shifted towards shorter wavelength (blue shift) in 100 eV and 500 eV. Secondly, at the fixed electron temperature, the larger the scattering angle, the greater the broadening. This feature can be used to increase the broadening on purpose when measurement of the low temperature plasmas are desired.

1.2.5. Principle of Thomson scattering diagnostics

The principle of the Thomson scattering diagnostics is similar to the spectroscopy. The electron temperature is determined by analyzing the Doppler broadening of the scattered light. And, the electron density is determined from the height of the measured spectrum, if the system is well calibrated. It requires a light source, a collection optics, and detectors. First, since the total cross section of Thomson scattering is extremely small as already explained in section 1.2.3, usually powerful lasers with the energy of > 1.5 J are utilized as an incident light source. Secondly, the scattered photons are collected by a set of lens or a mirror. Large size optics are preferred to collect the sufficient number of photons. Then, the collected photons are transferred to the detector that analyzes the spectrum. Finally, the electron temperature and density could be deduced by using a ratio evaluation method or Bayesian analysis [11].

1.2.6. Review of Thomson scattering diagnostic systems

Since the Thomson scattering diagnostic system is firstly demonstrated in high temperature measurement on the Russian tokamak T3 in 1969 [12], the various types of the systems have been developed and utilized as one of the most fundamental and critical diagnostics in a fusion experiments [13, 14, 15, 16, 17, 18, 19, 20, 21, 22].

The system has lots of merit in measuring the plasmas. Because Thomson scattering is the elastic scattering, the input beam does not transfer the energy to the plasmas. It is a stand-alone system because the concept of the Thomson scattering system does not require physical assumptions. In addition, the absolute values of the electron temperature and density are directly obtained from the well-calibrated system. Besides, since the pulse durations of the lasers are generally 8-20 ns, it provide information of very short moment. And, the spatial location and resolution is accurate as well.

On the other hand, successful detection of the Thomson scattering is difficult due to its small cross section. Therefore, it is resource consuming diagnostic system. Not only the powerful lasers or the large collecting optics for increasing light intensity, but also the superior quality of detecting and spectral analysis system demand high cost. Furthermore, stray light and the emission from the plasma could affect the measurement.

The key parameters for increasing the Thomson scattering signals could be summarized in three factors: the energy of the incident laser, the geometrical factor including a collecting solid angle and a scattering length, and the electron density. The performance of several Thomson scattering systems [13, 14, 15, 16, 17, 18, 19, 20, 21] are compared in Figure 1.7.

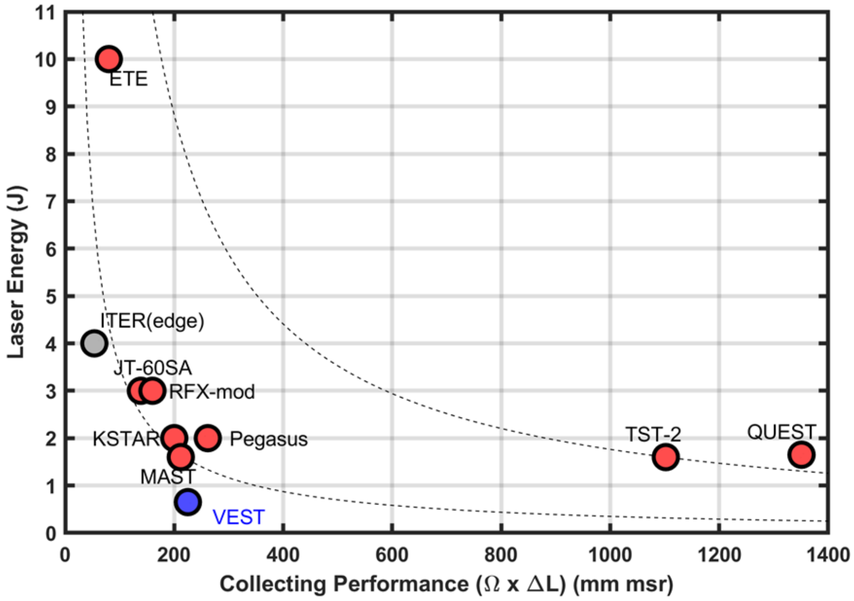

Figure 1.7 Performance of the Thomson scattering systems on various devices.

The abscissa of the figure means the geometrical factor, the product of the collecting solid angle and the scattering length. The machine performance is directly proportional to the product of the laser energy and the collecting performance, in other word, the area. Interestingly, almost Thomson scattering systems are distributed on the curve that having similar values of the product of the laser energy and the collecting performance. From the position of the data point, the concept of each Thomson scattering system could be guessed. For example, contrary to the KSTAR, JT-60SA, ITER, and MAST whose target electron density is about 1×10^{19} m^{-3}, TST-2 and QUEST have the large collecting performance, since they designed the system that could measure the low electron density of about 10^{17} m^{-3} for non-inductively sustained plasmas.

In case of VEST, the collecting performance is similar to large tokamaks, but the laser energy is lower than other devices. Furthermore, since both the ohmic electric field and the toroidal magnetic field are lower than the large devices, such as KSTAR and MAST, the expected plasma current is low. Therefore, the Thomson scattering signal measurement on VEST seemed pessimistic considering that the target density and the system performance.

1.3. Motivation

The successful measurement depends on not the signal level, but signal-to-noise ratio (SNR). Even if a large signal is expected, it is difficult to be distinguished where the noise level is comparable to the signal. On the contrary, the SNR can be increased if the noise level is much smaller than the expected signal.

$$SNR \propto \frac{E_L \Delta\Omega \Delta L n_e}{\sigma_{noise}}. \tag{1.39}$$

Except the electron density that depends on the plasma performance, SNR can be relatively simply increased by utilizing a high power laser and large collecting optics. However, it requires too high cost, so development of other necessary parts could be delayed in this research. Thus, increase of SNR is attempted by lowering the noise to the theoretically expected level, while maximizing the components on the numerator within a given budget.

1.4. Objectives

The main purpose of this dissertation is investigation of the design, development and optimization of the TS system that can provide the reliable electron temperature and density. Based on understanding of the principle and the physics regarding the TS system, the details of development, optimization, and calibration are presented. And, practical techniques to treat the noisy environment and signal analysis are described. It could help someone desire to develop the efficient and cost-effective Thomson scattering diagnostic system.

Chapter 2. Configuration of Thomson scattering system on VEST

2.1. Requirements for measurement

The minimum criteria for successful measurement could be considered to $\mathrm{SNR} > 1$. The prediction of the SNR could be performed using the values in the specification sheet [23] and the theoretical expression of the noises. The expected signal is express as Eq. (2.1) [24].

$$V_{TS} = G(Q.E. \times eM)R\eta N_{TS} = Gk\eta N_{TS}\,, \tag{2.1}$$

where G, $Q.E.$, e, and M are the amplifier gain, the quantum efficiency of an avalanche photodiode, electron charge, and the multiplication of the avalanche photodiode, respectively. η is determined by the low pass characteristics of an amplifier. In this computation, $\eta = 1(mV)/3.284 \times 10^{-2}(nVs)$ is used as a conversion constant between the peak voltage in mV and the time-integrated signal in nVs of a pulse signal. N_{TS} is the number of collected Thomson scattered photons.

For random noise sources, three dominant noises are selected: thermal noise, dark current noise, and shot noise. The thermal noise, also called Johnson-Nyquist noise, is generated by the thermal motion of the charge carriers in the resistors even if any voltage is not applied. The standard deviation of the noise is proportional to the square root of the room temperature and the bandwidth of the digitizer as expressed in Eq. (2.2).

$$V_{thermal} = G\sqrt{4k_B TR\Delta f}\,, \tag{2.2}$$

where k_B, T, and Δf are Boltzmann constant, the room temperature in K, and the bandwidth. The dark current noise originates from small current inside the photodiode even if no photons are detected by the detector, because of the random generation of electron-hole pairs in the depletion region. It changes depending on the room temperature, and measured with the voltage as Eq. (2.3).

$$V_{dark} = G i_{dark} R \,. \tag{2.3}$$

For conservative estimation of the SNR, the typical value of the dark current, i_{dark} of the APD was assumed the standard deviation. Shot noise, also called Poisson noise or statistical noise, occurs in photon counting since light has also the particle nature. [ref] According to the Poisson distribution, when the expected number of event is N, the standard deviation of shot noise is equal to the square root of N. Unlike that DC component, when the high frequency noise from the background light such as the stray light and plasma emission may not be attenuated by the filters. Therefore, similar to Eq. (2.1), the standard deviation of the shot noise is express as Eq. (2.4)

$$V_{shot} = Gk\eta\sqrt{N_{TS} + N_{stray} + N_{plasma}} \,. \tag{2.4}$$

where N_{stray} and N_{plasma} are the number of photons and the plasma detected by the same system as the N_{TS}. Finally, the total noise level is obtained by the sum of the standard deviations as Eq. (2.5)

$$V_{noise} = \sqrt{V_{thermal}^2 + V_{dark}^2 + V_{shot}^2} \,. \tag{2.5}$$

By using the Eq. (2.1) and Eq. (2.5), the minimum number of Thomson scattered photons that required to satisfy $SNR > B$ can be computed as following equations.

$$SNR = \left(\frac{V_{TS}}{V_{noise}} \right) > B. \tag{2.6}$$

$$\frac{k^2\eta^2}{B^2} N_{TS}^2 - k^2\eta^2 N_{TS} - \left[4k_B TR\Delta f + i_{dark}^2 R^2 + k^2\eta^2 (N_{stray} + N_{plasma}) \right] > 0 . \tag{2.7}$$

It can be noticed that the condition is expressed by the quadratic function in terms of N_{TS}. The computed results are depicted in Figure 2.1.

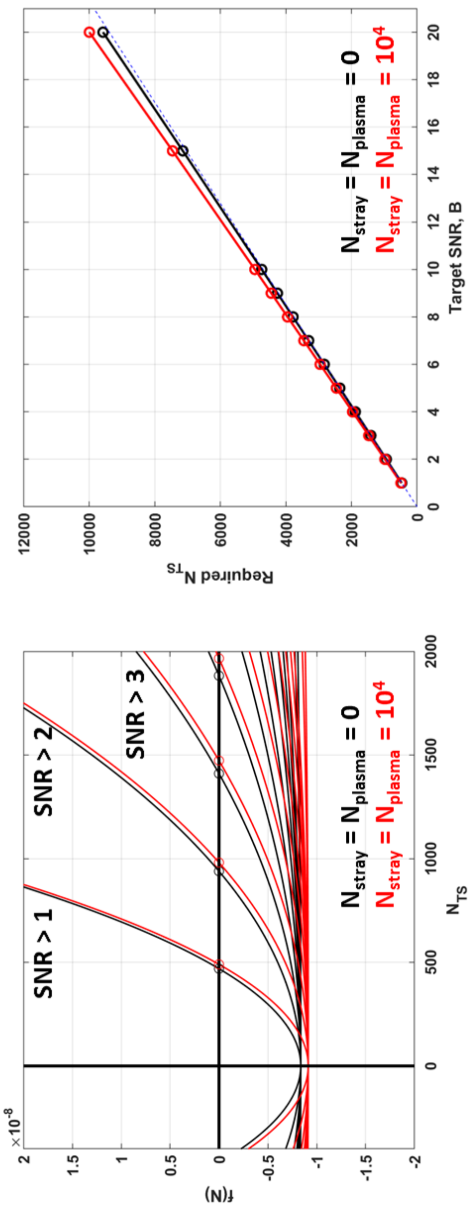

Figure 2.1 (Left) The computed results of Eq. (2.7) by changing B and (right) the number of Thomson scattered photons to satisfy SNR > B.

In the left figure, the black curves are the case of without the stray light and the plasma emission and the red curves are the case of $N_{stray} = N_{plasma} = 10^4$. The root of the equation increases as the more N_{stray} and N_{plasma} in fixed B, since the noise level is increased. The ordinate of the right figure indicates the root of the equation, and the abscissa does the target SNR. As N_{TS} increases, V_{shot} increases as well, therefore, it is indicating that the rate of increase of N_{TS} is larger than the rate of the SNR.

To measure the Thomson scattering signals in VEST with the stray light and the plasma emission, at least 450 photons should be transferred to each APD to satisfy SNR > 1, and about 1000 photons are required to obtain SNR > 2.

2.2. Overview of the system

The Thomson scattering system on VEST consists of a laser injection system, a collection optics, a polychromator, and a data acquisition system. The schematic of the system is illustrated in Figure 2.2.

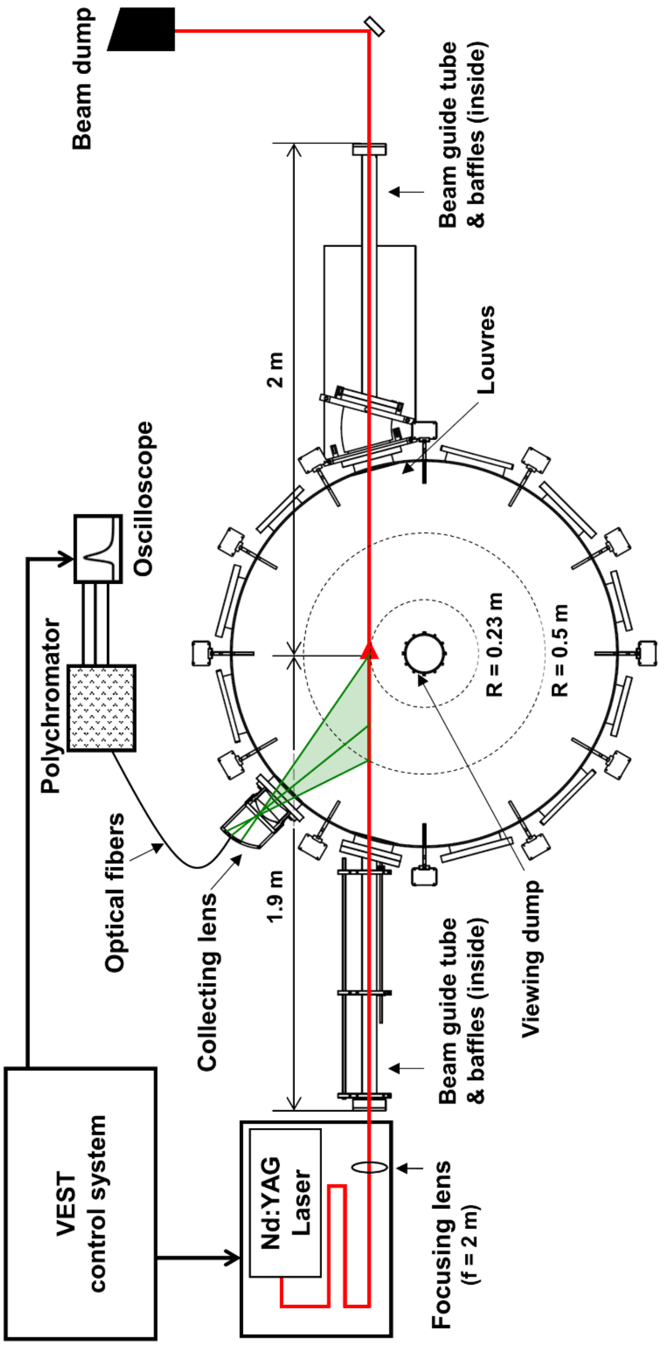

Figure 2.2 The schematic of the Thomson scattering diagnostic system on VEST.

When the laser beam is injected into the plasma, the scattered photons from plasmas are collected and transferred to the polychromator by the collecting optics system. Each channel of the polychromator selectively detects the scattered photons in the desired spectral bandwidth. Then, the signals are digitized by an oscilloscope to analyze the Doppler broadening which is related to the electron temperature. The main parameters of the system is summarized in Table 2.1.

Table 2.1 Main parameters of the Thomson scattering diagnostic system on VEST

Parameters	Value
Laser energy (J)	0.85
Laser wavelength (nm)	1064
Laser repetition rate (Hz)	10
Collecting f-number	4.7-3.6
Scattering length (mm)	12-4
Viewing range (m)	$0.23 < R < 0.5$
Viewing range (normalized)	$-0.61 < \rho < 0.2$
Number of polychromator	1 (+1)

2.2.1. Laser injection system

The purpose of the laser injection system is maximize the laser energy reaching to the plasma for increasing the scattered photons as many as possible. Therefore, it is designed to use as few optical elements as possible to minimize the loss along the beam path to the vacuum window. As a probing beam, the system utilizes a pulsed Nd:YAG laser with the energy of 0.85 J which is relatively weak for TS measurements. The pulse duration and repetition rate of the laser is 7.8 ns and 10 Hz, respectively, and the fundamental wavelength of 1064 nm is used to avoid the power loss during the frequency conversion. The details of the laser is presented in Table 2.2.

Table 2.2 Specification of the Nd:YAG laser

Parameters	Value
Output energy (J)	< 0.85
Laser wavelength (nm)	1064
Laser repetition rate (Hz)	10
Energy stability (%)	± 2
Pulse width (ns)	11
Divergence (mrad)	< 0.5
Beam diameter	10
Measured M-squared	10

Along the beam path of 4.4 m from the laser head, the laser enters through the vacuum chamber by passing a Faraday isolator, a half-wave plate, six mirrors, and a plano-convex lens with the focal length of 2 m as illustrated in Figure 2.3 and Figure 2.4. Instead of using the Brewster windows, the anti-reflection (AR) coated windows have been adopted (Figure 2.5).

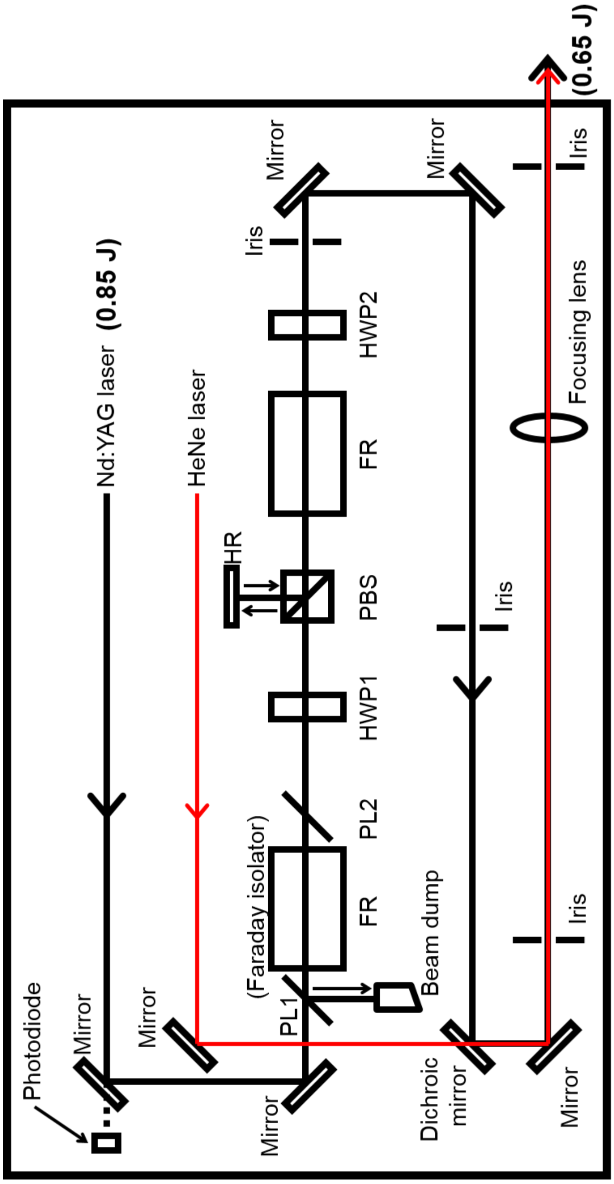

Figure 2.3 The schematic of the laser injection optics. The beam path of (black) the Nd:YAG laser and (red) the HeNe laser.

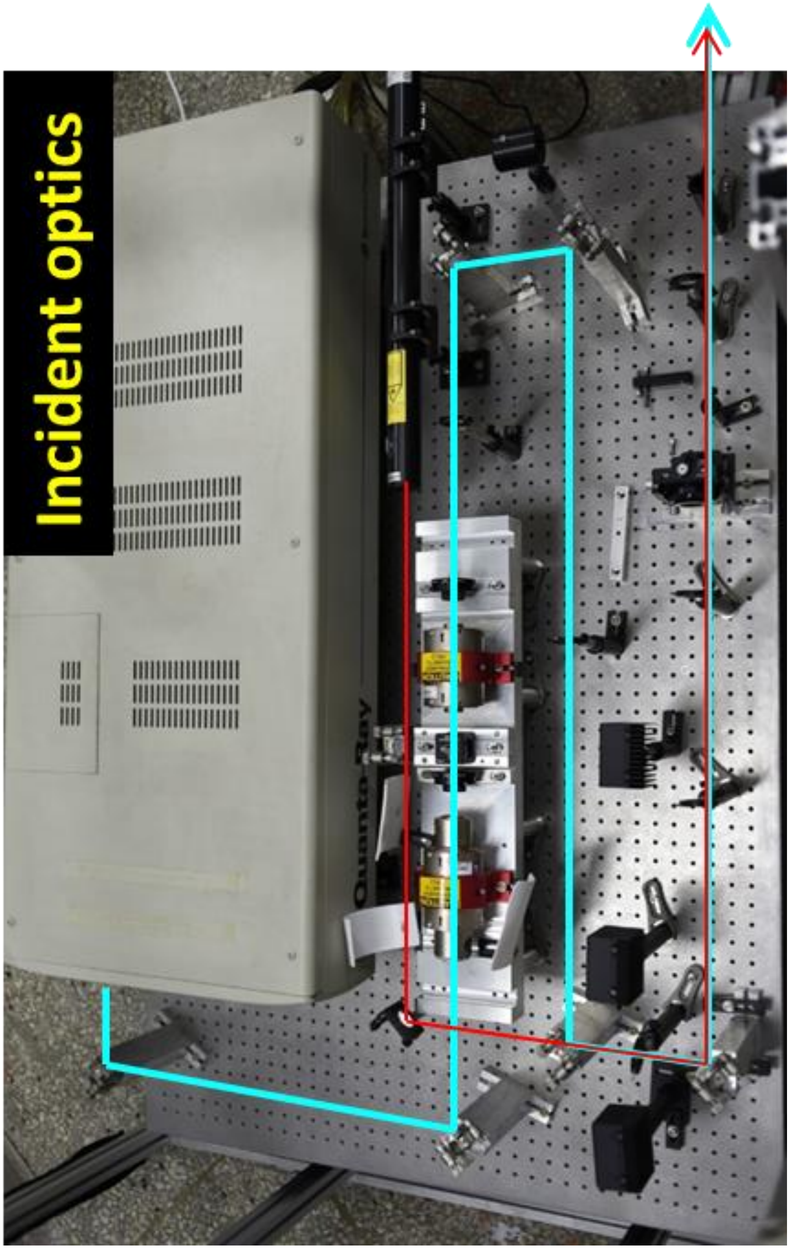

Figure 2.4 The installed laser injection optics. The beam path of (cyan) the Nd:YAG laser and (red) the HeNe laser.

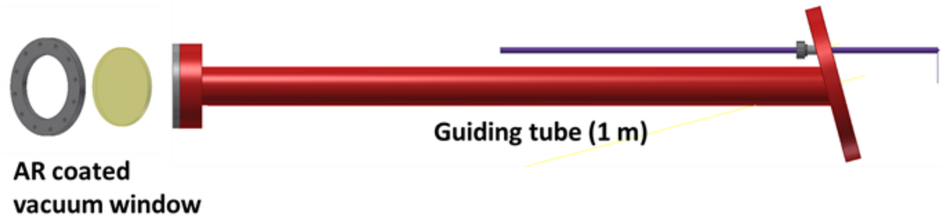

Figure 2.5 Anti-reflection coated window is installed on the laser guiding tube as vacuum entrance / exit windows.

The transmission of the AR coated windows is > 99.4% at the laser wavelength. It also used to minimize the alignment error that may be caused by the different refractive index between the Rayleigh scattering and the Thomson scattering as shown in Figure 2.6. Due to the total loss along the beam path, the maximum beam energy measured inside the vacuum vessel is 0.65 J. As shown in Figure 2.2, the entrance window and the exit window are symmetrically installed at the end of 1-m-length guiding tubes. The distance between two windows is ~3.9 m, and the focal point of the beam is 1.9 m far from the entrance window. Focusing of the laser using the convex lens not only collimates the beam along the beam path, but also helps to collect the scattered photons with a single core fiber by decreasing the beam diameter. After the beam exits the vacuum vessel, it is tilted at about 90 degree by a mirror and trapped by a beam dump, which is shown in Figure 2.7. To minimize the misalignment of the beam caused by the machine vibration, both the laser optic table and the dump are unconnectedly installed from the vacuum vessel except for the vacuum windows.

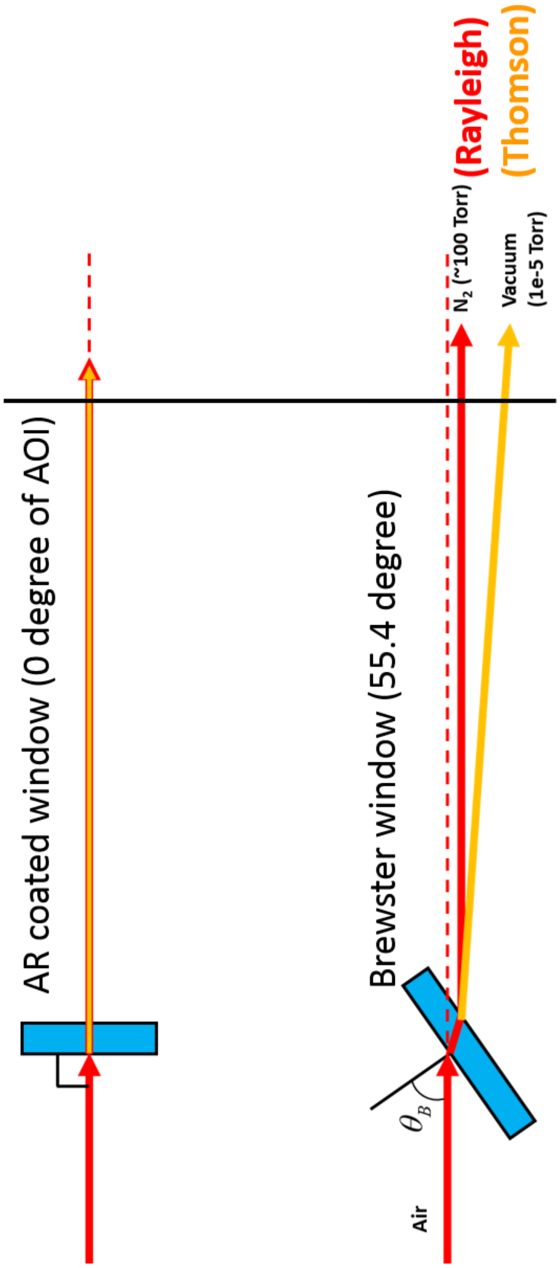

Figure 2.6 The difference of the beam path during Thomson scattering and Rayleigh scattering. Alignment error caused by the different refractive index of between nitrogen and vacuum can be ignored in case of angle of incidence = 0.

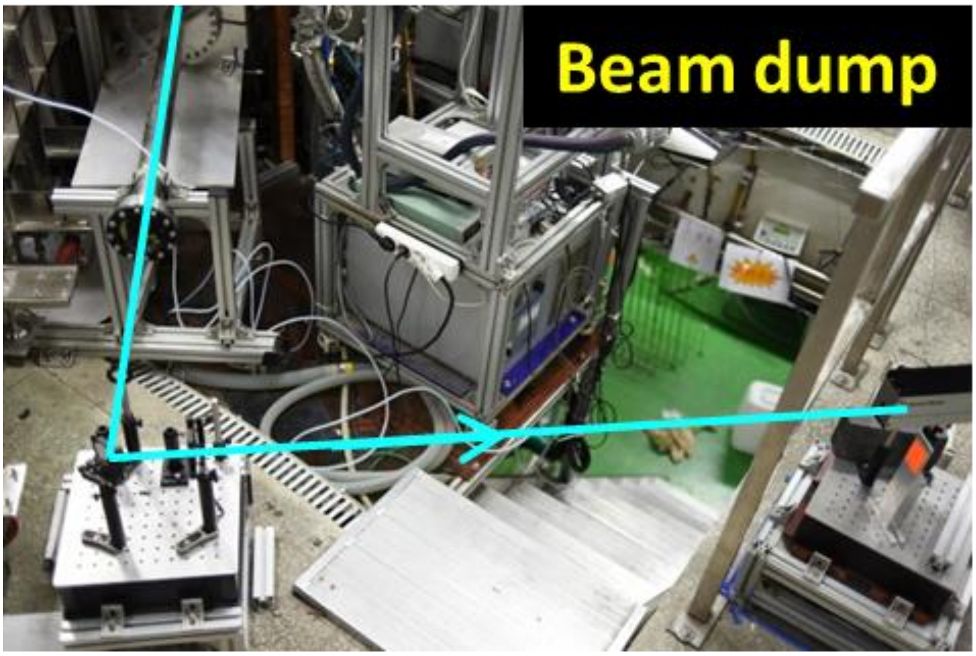

Figure 2.7 The beam dump of the lasers; Both Nd:YAG and HeNe lasers are trapped by the beam dump after they passed through the vacuum window and tilted by a mirror.

The focal point and the distance between the exit window and the beam dump have been set so that the two vacuum windows and the beam dump are safe. The M-squared factor of the Gaussian beam has been obtained from the measurement of the beam radius along the distance and fitting as illustrated in Figure 2.8. The beam diameter along the beam path is calculated by using the measured beam diameter and the M-squared of the Gaussian beam as shown in Figure 2.9. The beam diameter is fitted by using Eq. (2.8). The beam propagation is calculated by referring the Self's paper [25] with consideration of the measured M-squared factor.

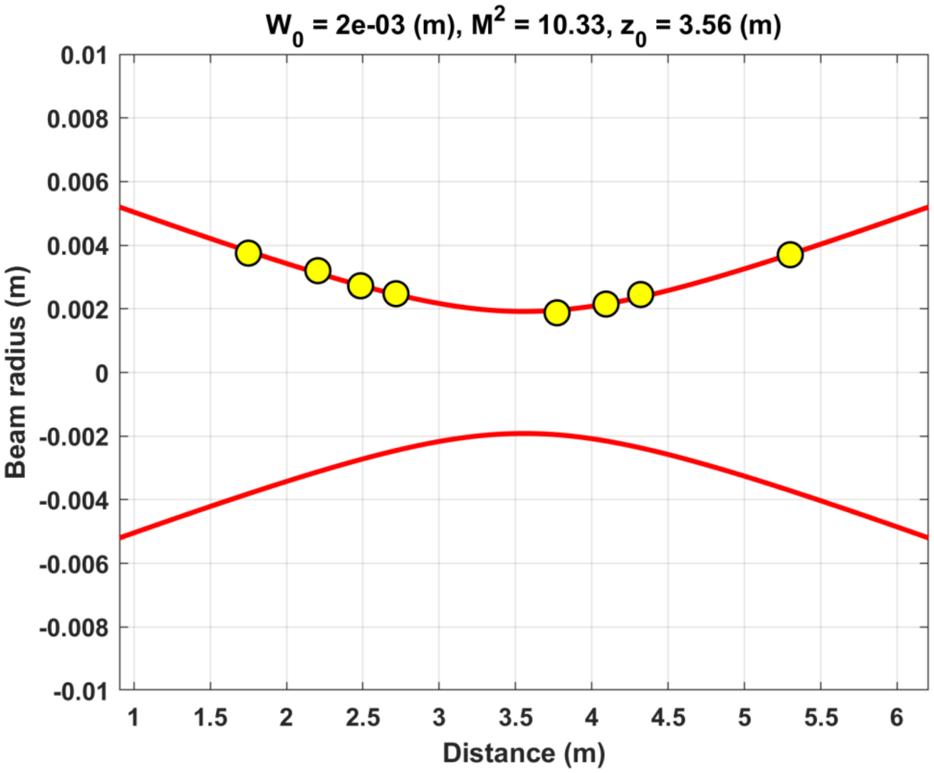

Figure 2.8 Measured result of M-squared of the Gaussian beam

$$W(z) = W_0 \sqrt{1 + \frac{M^2 \lambda}{\pi W_0^2}(z - z_0)^2} \ . \tag{2.8}$$

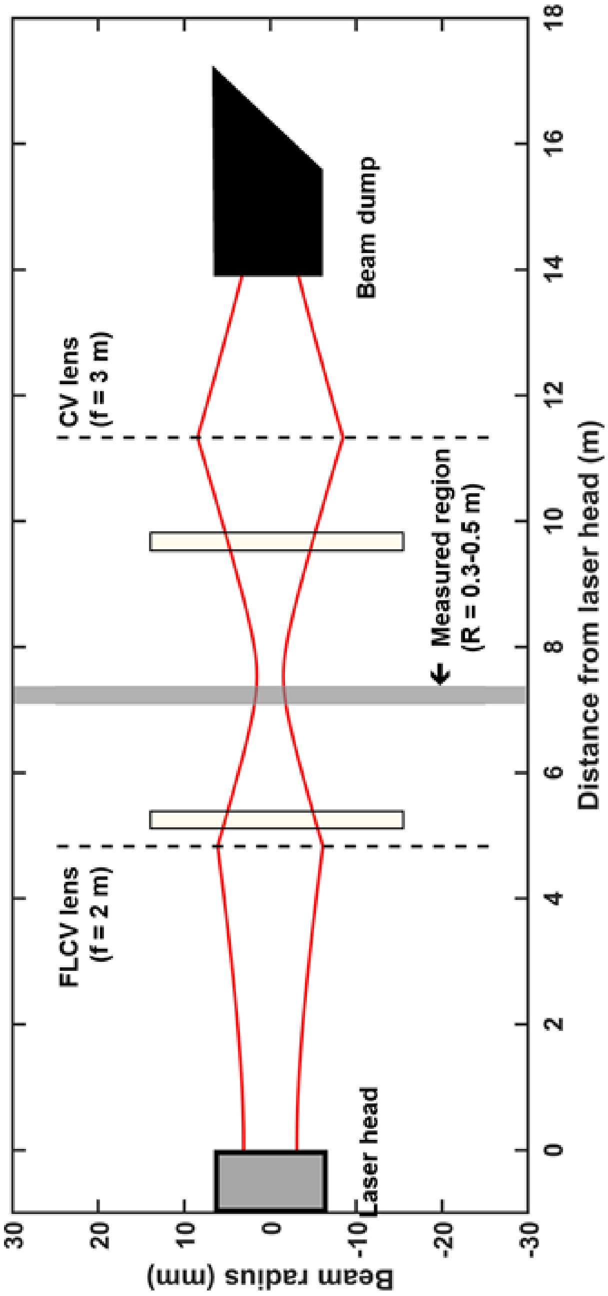

Figure 2.9 The beam diameter of the Nd:YAG laser along the beam path.

2.2.2. Collecting optics

The collecting optics system is designed focusing on two points of views: to increase the spectral broadening and to maximize the collection solid angle. Firstly, as mentioned in section 1.2.4, since the TS spectrum is the function of not only the electron temperature, but also the scattering angle, the observing direction affects the measured spectrum. In case of VEST plasmas, the expected spectral broadening of the target temperature range is too small to analyze the spectrum using a set of interference filters. Therefore, the proper lens position is determined so that the scattering angle is about 130 degree to get a much broader spectrum, as illustrated in Figure 2.10. The different measurement position has the different scattering angle. Therefore, every scattering angle should be larger than 90 degree at the desired measurement range. In order to use the 3D CAD program, the scattering angles are measured in several scattering position. It is checked that the difference between the measured and the designed angle is lower than 0.2 degree (Figure 2.11). Based on actual measurement results, the scattering angle of every measurement point is estimated by using the designed values, and the results is shown in Figure 2.12.

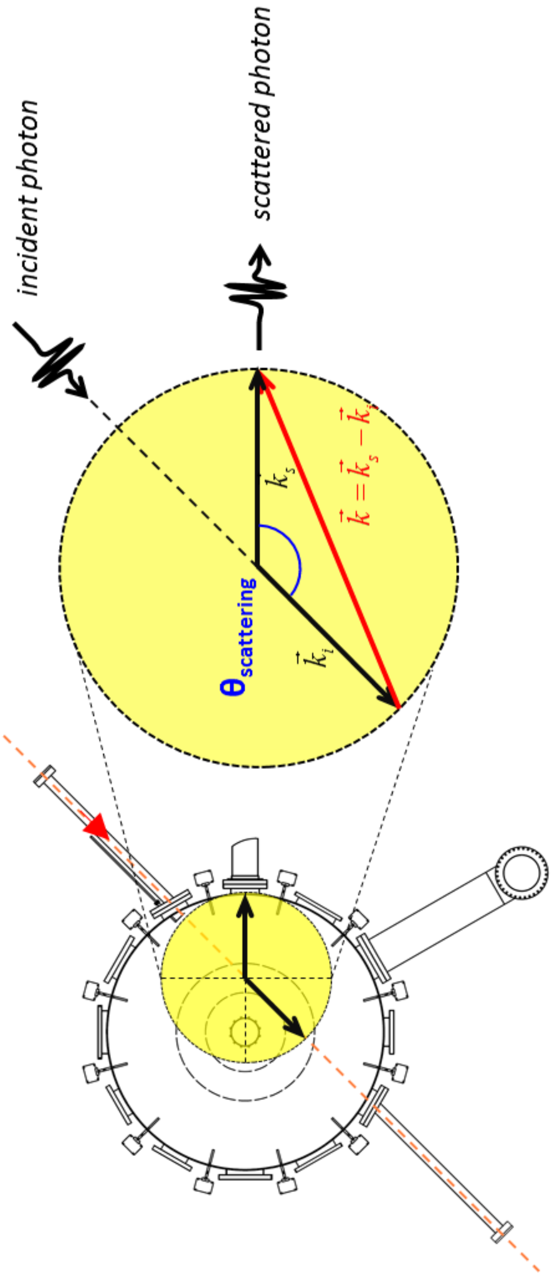

Figure 2.10 The scattering geometry of the system. The location of the collecting lens is determined by considering the large scattering angle.

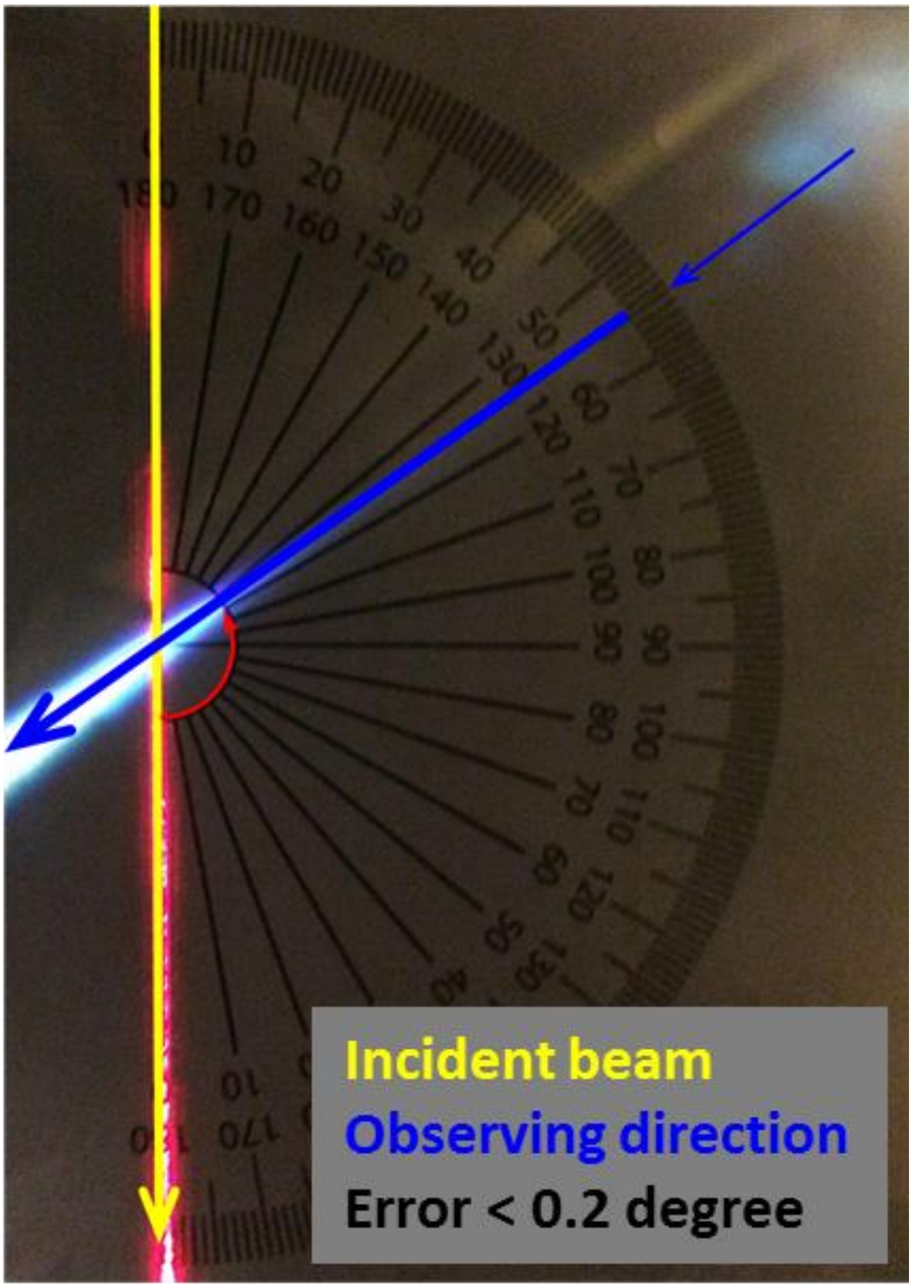

Figure 2.11 Measurement of the scattering angle at the scattering position of R = 0.4 m. The error between the measurement and the design has been lower than 0.2 degree.

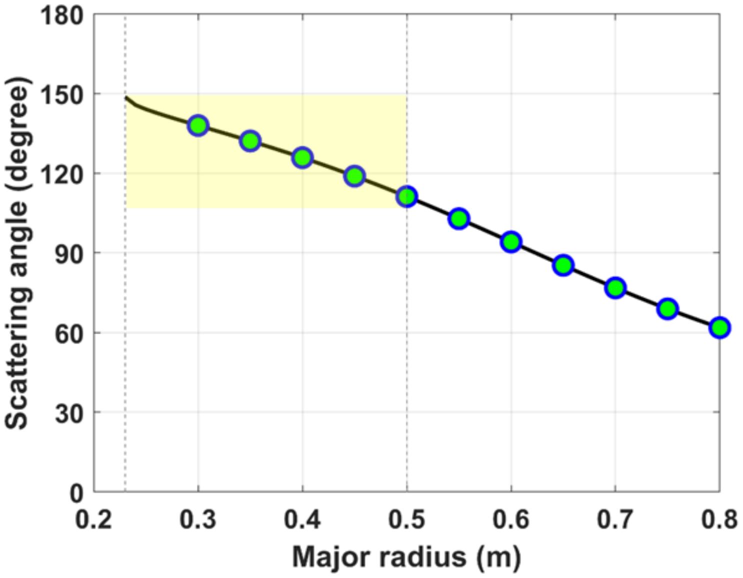

Figure 2.12 Scattering angle as a function of major radius. The data are gathered using Autodesk Inventor, the 3D CAD program.

Secondly, the lens specifications are determined to have a maximum solid angle at its position. The collecting lens consists of two customized aspheric lenses as illustrated in Figure 2.13 for minimizing spherical aberration as well as astigmatism. The effective focal length and the diameter are f = 123.6 mm and d = 109 mm, respectively. Near the optical axis of the lens, the magnification and the collecting f-number are 3.3×, and f/4, respectively. Each lens is AR coated by the wavelength of 1064 nm for reduction of the photon loss. In the VEST chamber, the plasma boundary is typically located between $0.1 \leq R(m) \leq 0.76$ due to the limiters on the center stack and the low field side wall. The coverage region of the collecting optics system is $0.23 \leq R(m) \leq 0.5$ ($-0.61 \leq \rho \leq 0.21$) as depicted by green area in Figure 2.2. Figure 2.14 is the ray diagram for the collecting lens is simulated by using LightTools for R = 0.3, 0.4, and 0.5 m. The lower limit is determined by the radius of the smallest circle that the laser meets tangentially. On the other hand, outside the R = 0.5 m, the solid angle greatly decreases due to the limitation of the angle of view.

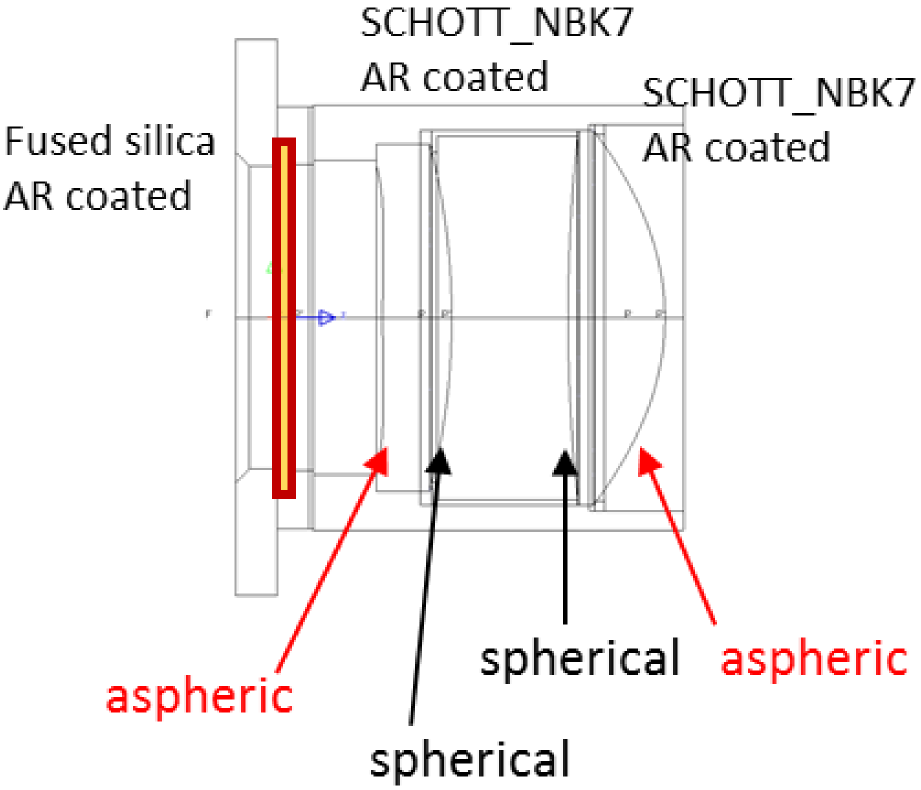

Figure 2.13 The drawing of assembly of the vacuum window and collecting lens housing.

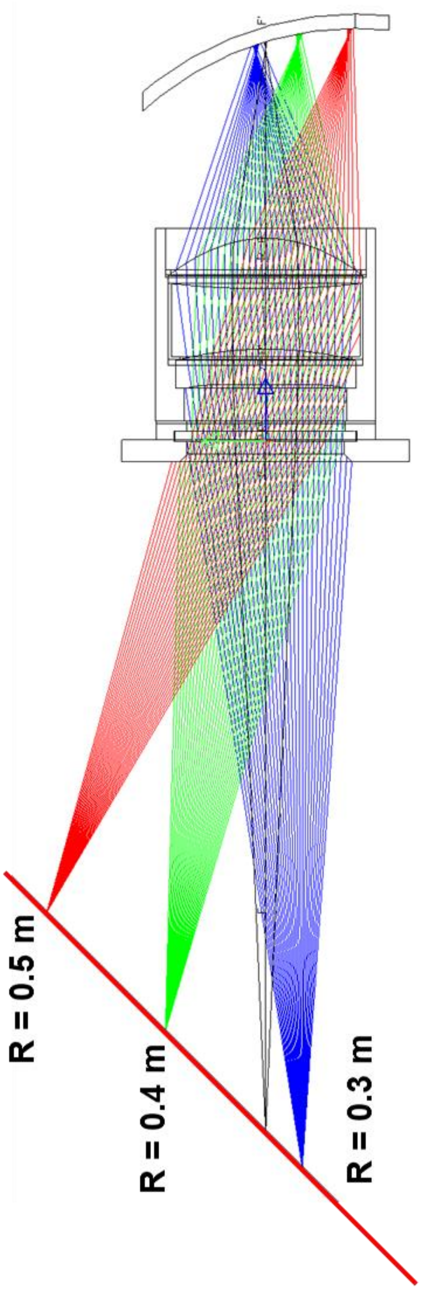

Figure 2.14 The ray diagram of the collecting lens simulated by LightTools about the three measurement positions: R = 0.3, 0.4, and 0.5 m.

The lenses are also AR coated like as the vacuum windows. The upper graph of Figure 2.15 is the transmittance of a single window. Red dots are the data points measured by the coating company, Green optics. The lower figure is the transmittance of the lens. In case of the lens, the collected light would not be monochromatic. Therefore, the transmittance between the wavelengths from 900 nm to 1064 nm is compensated during the analysis of the Thomson scattering signals.

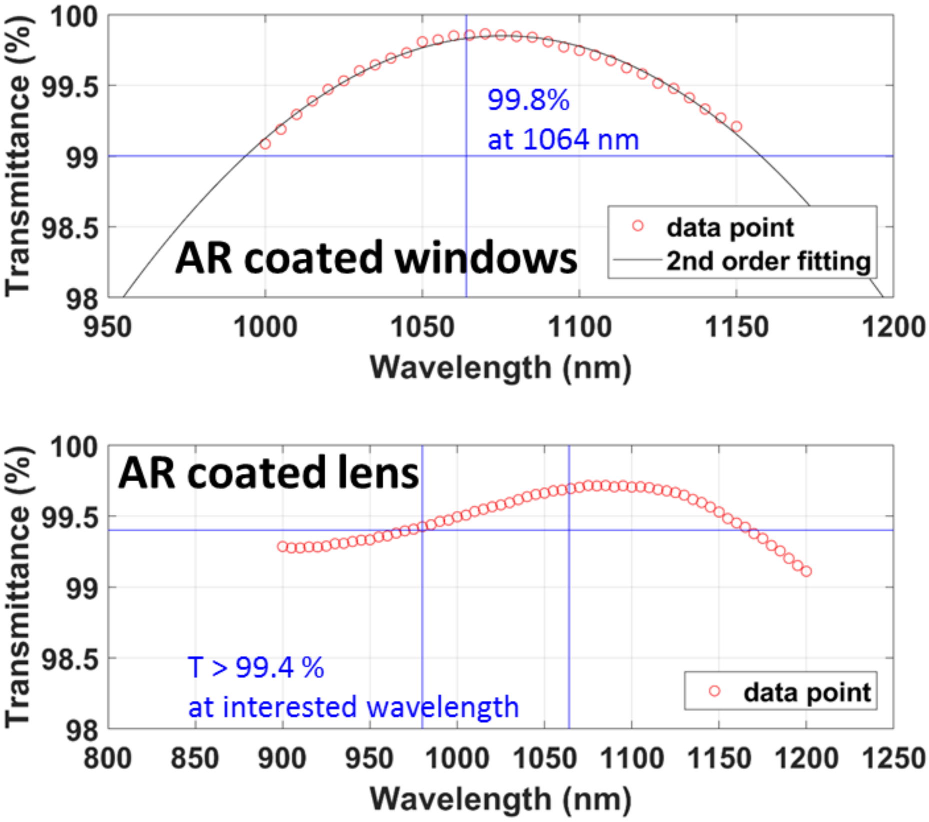

Figure 2.15 The measured transmittance of (top) the AR coated vacuum windows of both laser injection system and collecting optics and (bottom) the AR coated lens.

The collected light by the lens is transferred to the polychromator by a 1.5-m length single core optical fiber with a core diameter of 1500 um and a numerical aperture (N.A.) of 0.39 (FT1500UMT, Thorlabs). The scattering length is mainly determined by the size of the optical fiber, and with the magnification of the lens and the scattering angle [26]. Figure 2.16 and Figure 2.17 show the scattering length and the collecting solid angle within the viewing range. In addition, the product of the scattering length and the solid angle is illustrated in Figure 2.18. The optical power collected by the lens is conserved during the transmission as the minimum etendue [27] is determined by the collecting lens; the etendue of the collecting optics is summarized in Table 2.3. The fibers are connected to a fiber holder in the shape of an image-plane, and the holder is installed on the solid optical stage as shown in Figure 2.19. Besides, inside the vessel, a replaceable AR coated vacuum window (d = 127 mm) is installed in front of the lens to prevent the degradation of the lens transmission, and a mechanical shutter protects it during the wall conditioning with the glow discharge plasma.

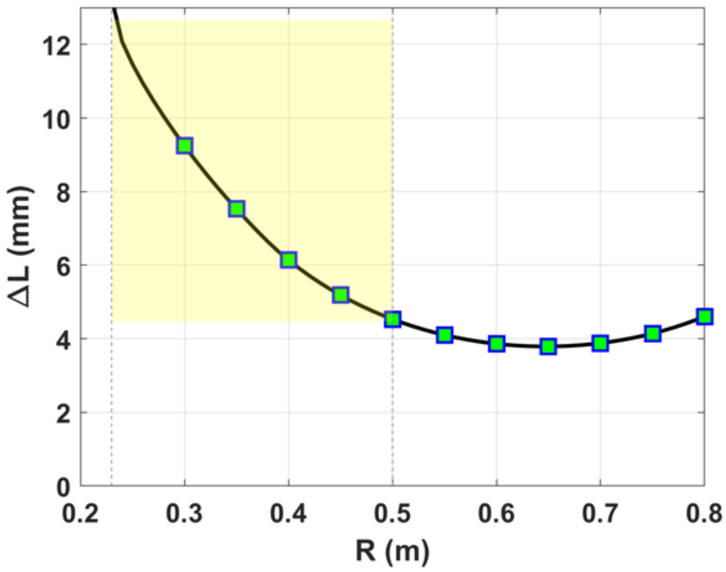

Figure 2.16 Scattering length as a function of major radius.

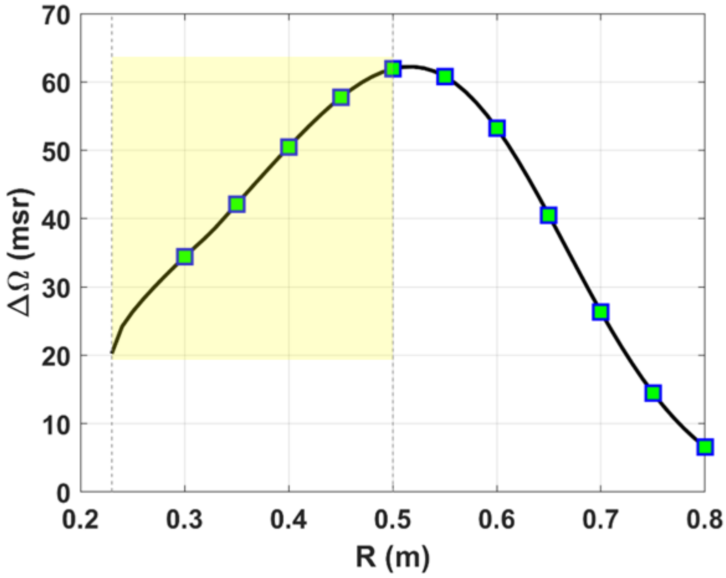

Figure 2.17 Solid angle as a function of major radius.

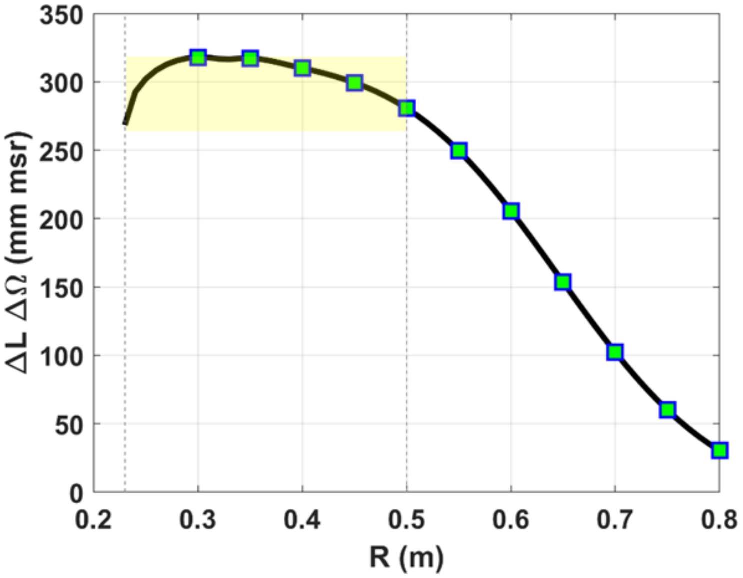

Figure 2.18 Product of the scattering length and the solid angle

Table 2.3 The etendue of the collecting optics.

Source	**Target**	**ΔA_{source} (mm^2)**	**ΔA_{target} (mm^2)**	**distance (mm)**	**N.A.**	**Etendue (mm^2sr)**
Plasma	Collecting lens	9	1.4×10^4	58	0.12	0.42
Collecting lens	Optical fiber	1.4×10^4	1.8	16	0.39	0.84
Optical fiber	Collimating lens 1	1.8	8.5×10^2	27	0.39	0.84
Collimating lens 2	APD	8.5×10^2	7.0686	24	0.56	6.9

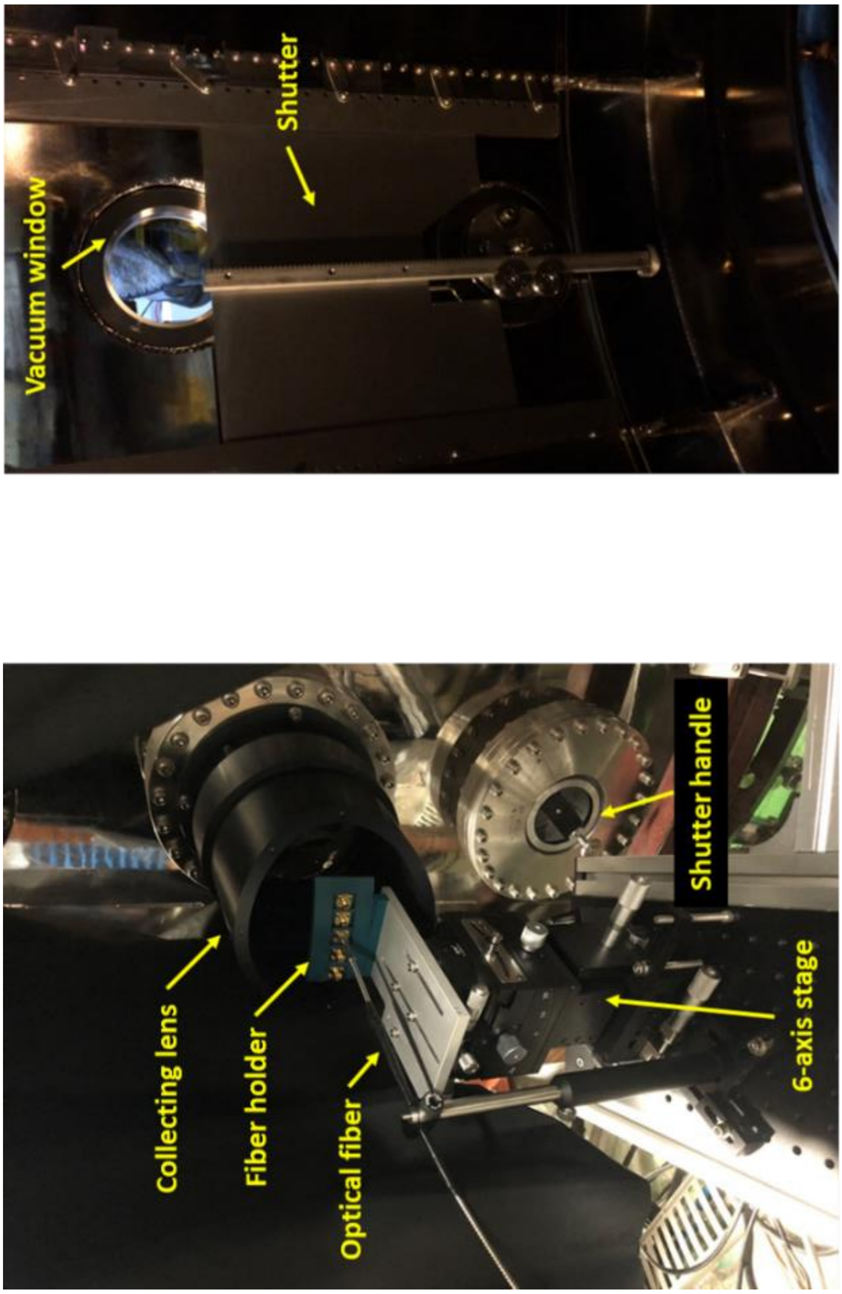

Figure 2.19 The collecting optics (left) outside the vacuum vessel and (right) inside the vessel.

2.2.3. Polychromator

Polychromator is usually employed type of the spectrum analyzer in Thomson scattering diagnostics in fusion devices. The most generally used spectrometer with the charge-coupled devices (CCD) could not be adopted, because the expected number of photons is not sufficient to be detected by the CCD. On the other hand, the filter polychromator can increase the amount of light entering one sensor although it cannot directly measure the spectrum due to the small number of spectral channels. The polychromator for VEST is developed based on the polychromator of KSTAR [28]. The mimic of the relay and collimating optics of KSTAR polychromator have been installed. However, a set of interference filters is different because the target electron temperature of VEST is much lower than the temperature of KSTAR. The specification of the filters are summarized in Table 2.4. The objectives of filter 1 and filter 2-4 are absolute calibration for electron density measurement and spectral calibration for electron temperature measurement that are described in Chapter 3.

Table 2.4 The specification of the filters equipped in the polychromator

Filter number	Type	Center wavelength / FWHM
1	Band pass filter	1064 / 4
2	Band pass filter	1060 / 10
3	Band pass filter	1050 / 10
4	Band pass filter	1025 / 50
	Short pass filter	1040 (cutoff)

There was a trade-off in use of the research fund between the development of collecting lens and purchasing a set of customized interference filters. For instance, if the well-designed filter sets [29] were prepared, the expected transmittance and reflectance are satisfactory. However, due to the extremely high cost of small number of the customized filter, the sufficiently large collecting solid angle could not be obtained. On the other hand, the collecting lens with the large solid angle has been developed to increase the feasibility of the signal measurement, taking the decrease of the filter specification, which is related to both the spectral resolution and the photon loss. It can be noticed that the full width at half maximum (FWHM) of the filters are quite large, thus, the overlap between the filters causes difficulties in measurement. The problems caused by the filter specifications will be discussed in more detail in Chapter 3.

2.2.4. Data acquisition

The typical pulse width of the discharges of VEST is 10-20 ms and the repetition rate of the laser is fixed as 10 Hz. It means that only one pulse can match the time of the plasma with accurate synchronization. The synchronous system is developed as illustrated in Figure 2.20 and Figure 2.21. The time sequence of the system is presented in Figure 2.22. At the warm up phase, an external 10 Hz oscillator is entered as a trigger signal for the flash lamp. The Q-switching trigger occurs automatically inside the laser power supply. When the plasma discharge signal is activated in the VEST control system, a master signal is transferred to a pulse generator 17 sec before the discharge. Then the trigger for the flash lamp is switched from the external oscillator to the pulse generator that generates 10 Hz signal exactly synchronized with the VEST control system. Finally, after 17 sec of the master signal, additional trigger signal is transferred to an oscilloscope (Tektronix DPO7104C) to activate the data recording. While the maximum sampling rate is 10 GS/s, the sampling rate of 1 GS/s has been used to avoid unwanted distortion of the waveform due to its bandwidth of 1 GHz.

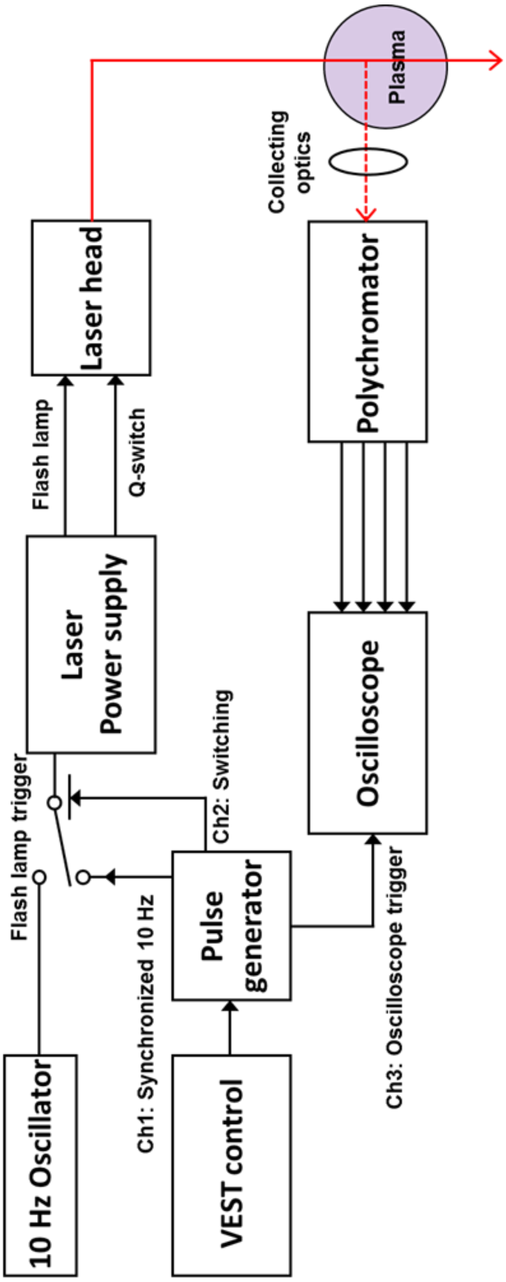

Figure 2.20 The circuit diagram of the synchronous system.

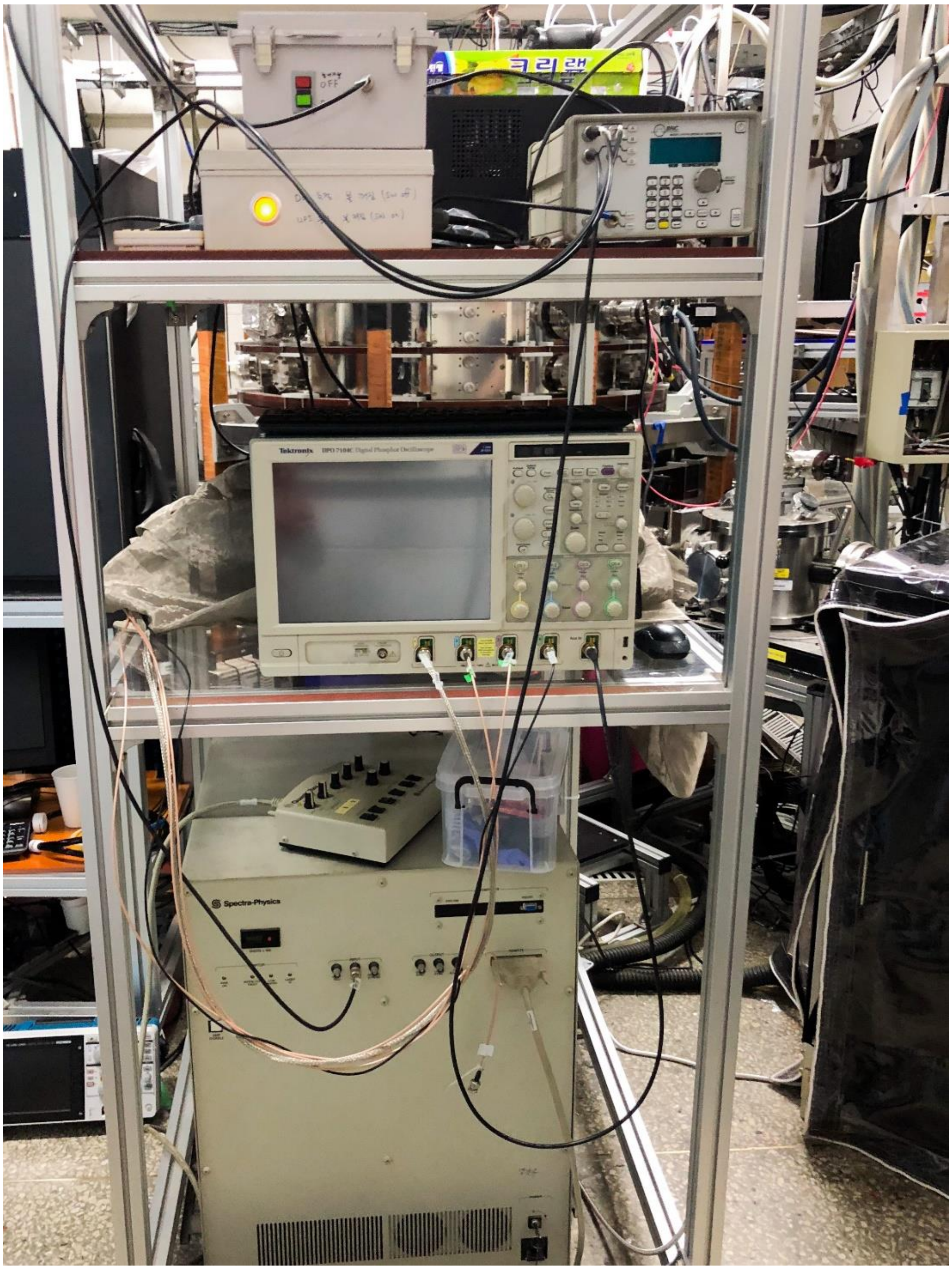

Figure 2.21 Data acquisition system consists of an oscillator, a pulse generator, relay, and an oscilloscope.

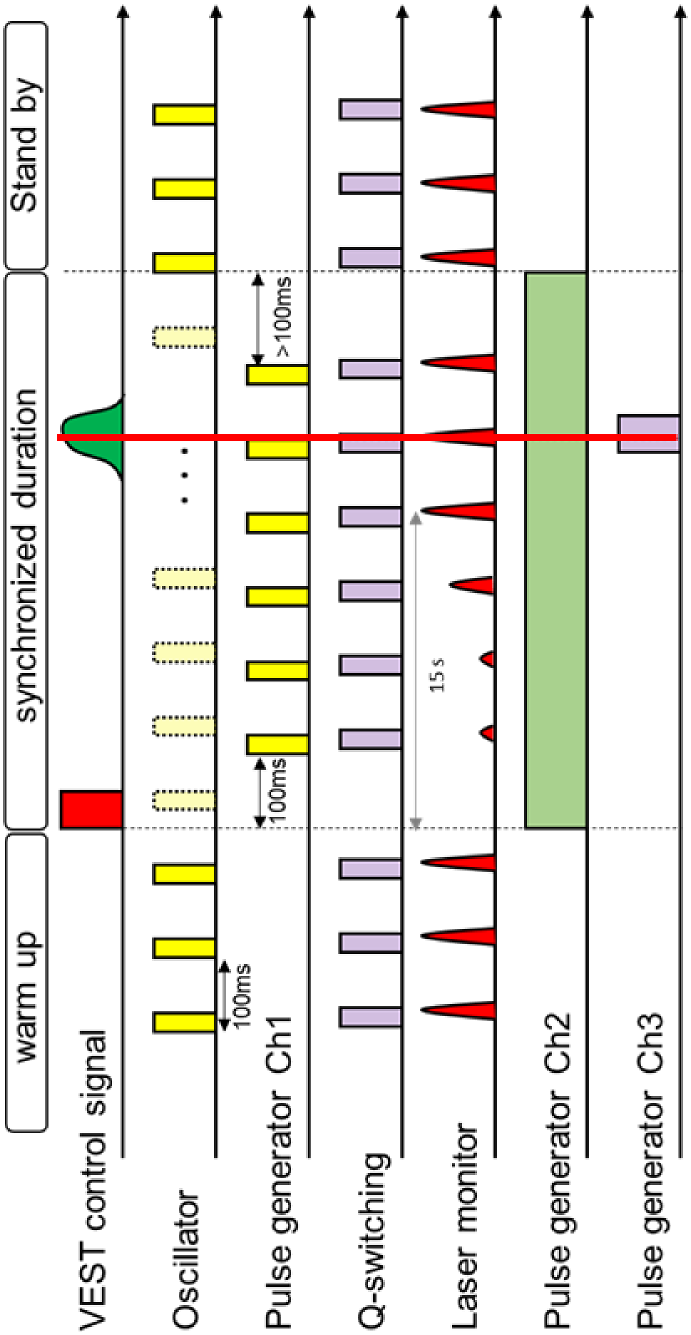

Figure 2.22 The time sequence of the Thomson scattering system on VEST.

2.3. Evaluation of the system

To check the number of collected photons is enough to satisfy the requirements computed in section 2.1, the numbers of photons are theoretically estimated as shown in Table 2.5 [30]. Referring the estimation, about one thousand photons would be detected by each APD, in case of the electron density is 5×10^{18} m^{-3}. Therefore, the plasmas with the electron density of 2.5×10^{18} m^{-3} may be detected with signal-to-noise of 1.

Table 2.5 The number of photons estimated at the electron density of 5×10^{18} m^{-3} with assumptions that the photons are uniformly distributed to the APDs.

Number of photons	Equation	Values
Laser	$\frac{E_L}{h\nu}$	4.55×10^{18}
Thomson scattering	$n_e\frac{E_L}{h\nu}\Delta L\int_{4\pi}\left(\frac{d\sigma_{TS}}{d\Omega}\right)d\Omega$	7.57×10^{6}
Collected	$n_e\frac{E_L}{h\nu}\Delta L\int_{d\Omega}\left(\frac{d\sigma_{TS}}{d\Omega}\right)d\Omega$	29577
Polychromator	$N_{collected}\int S_{TS}(T_e,\lambda)T(\lambda)d\lambda$	19750
APD	$N_{Polychromator}\times T\times R_f\times\frac{1}{2}\times\frac{1}{\#_{ch}}$	1129

Chapter 3. Improvement of signal-to-noise ratio

The interference filters have deficiencies in the transmittance, the reflectance, and the bandwidth. In this chapter, the efforts to overcome the problem related with the poor pass band and to improve a photon-to-electron conversion efficiency are described. In addition, the reduction of the stray light and the noise for improving signal-to-noise are presented.

3.1. Optimization of polychromator

The specification of the filters, summarized in Table 2.4, is illustrated in the left of Figure 3.1. The optical density at the right side of the figure is obtained by a log of the inverse of the transmittance. It shows two problems; one is the pass bands of the filters are seriously overlapped, and another one is the optical density at the laser wavelength is too low to block the stray light. To reduce the bandwidth of filter 4, a short pass filter (SPF) has been installed whose cutoff wavelength is about 1040 nm. Consequently, the usable pass band and the optical density at the laser wavelength has been obtained. In this thesis, filter 4 means the combination of filter 4 and the short pass filter.

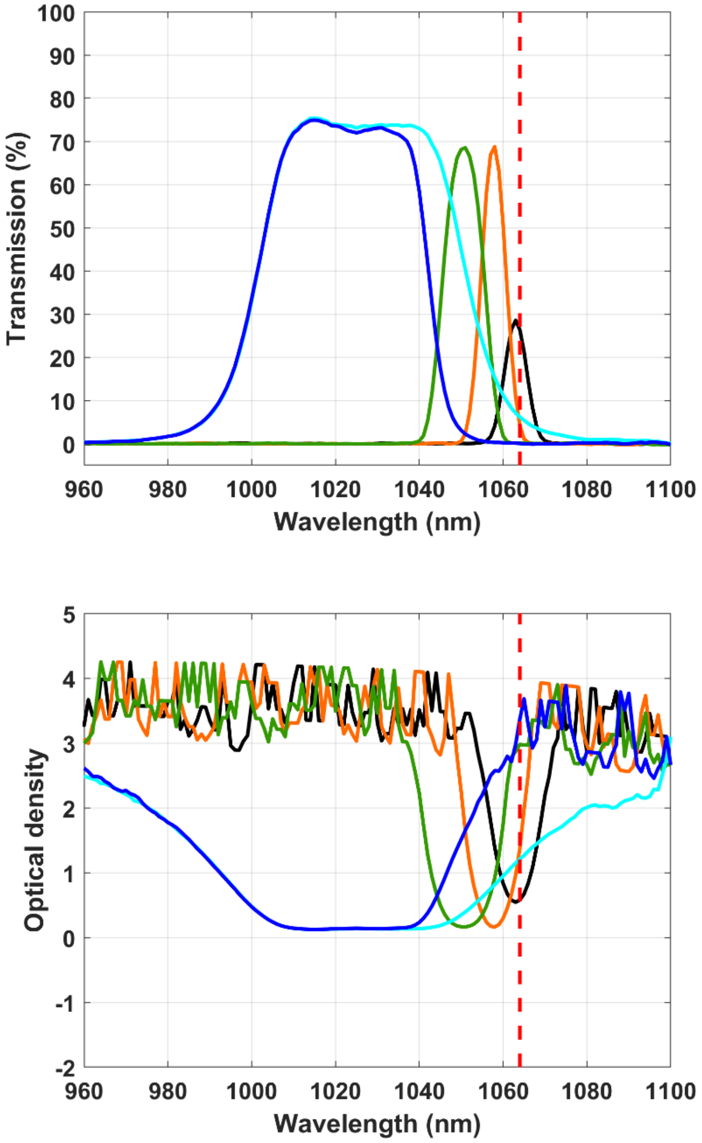

Figure 3.1 (Top) The transmittance of the interference filters. (Bottom) The optical density of the filters.

3.1.1. Placement order of filters

To find the best placement order of the filters, three candidates are chosen by experiments that the measuring the responsivity for possible combinations. The first combination is 1-2-3-4 depicted in red curve in Figure 3.2 (a). It minimizes the total loss of the photons inside the polychromator, since the filter of higher reflectance is placed first and the lower is the later. However, since filter 4 placed at the end measures the tail region of the TS spectrum, the signal amplitude of filter 4 was often buried in the noise level in actual measurements. Moreover, the high responsivity of the filter 1 is not useful for the spectral analysis, because it is for the absolute calibration. On the contrary, the reversed arrangement 4-3-2-1 is tested to give a priority to measure the tail region. However, filter 3 becomes obsolete due to the pass band is overlapped by filter 4. In this case, since the photons near 1050 nm transmit filter 4 in advance, the amount of photons reaching to filter 3 is decreased. As a result, the relative error of both low and high temperature regions increased, and measurable range gets narrower as depicted in Figure 3.2 (b). As a compromise, the measurement with the filter set 3-4-2-1 is conducted. Like the set 4-3-2-1, filter 2 and filter 1 are placed on the rear to preserve the photons in the short wavelength region. Moreover, filter 3 is arranged in front of filter 4 so that the bandwidth of both filters can be used. The relative error calculation, as illustrated in the Figure 3.2 (b), supports that this placement order is the best in the given resources. The relative errors are calculated by Monte-Carlo simulation for the position of R = 0.35 m using the parameters such as laser energy of 0.65 J, electron density of 5×10^{18} m^{-3}, solid angle of 50 msr, and scattering angle of 131.9 degree, by assuming the Gaussian noise composed of the Johnson noise, the shot noise, and the dark current [31]. In this thesis, I define the interval where the error is lower than 10% as the measurable temperature range.

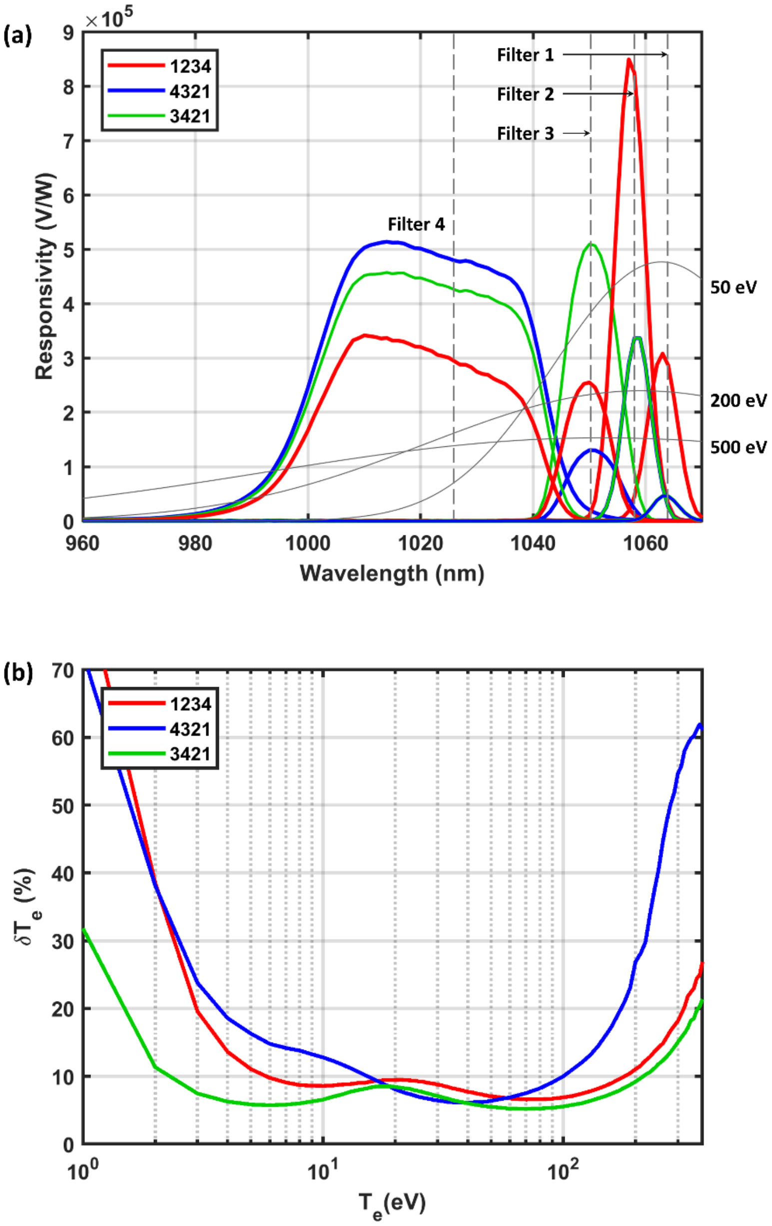

Figure 3.2 (a) The responsivity of the polychromator and (b) the relative errors about the electron temperature.

3.1.2. Photon-to-electron conversion efficiency

The polychromator equips the infrared enhanced APD, S11519-30 from Hamamatsu photonics [23], which is highly sensitive to the light with the wavelength > 1000 nm. Since both the electron multiplication and the dark current in APD have dependence on the reverse bias voltage [32], there should be an optimum voltage for each APD. Therefore, the bias voltage is scanned from 0 to 300 V to find the optimal. The experimental results of the APD at channel 3 are presented in Figure 3.3.

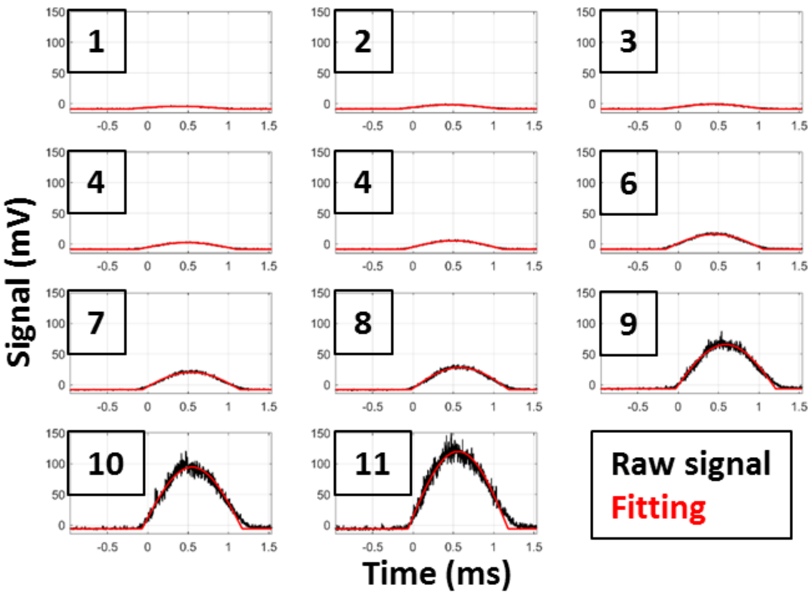

Figure 3.3 The signals of the APD equipped with the filter 3. The larger data number is the signal measured in higher voltage.

As a result, the optimum bias voltage that maximizes the signal-to-noise ratio of each APD is found. The voltages are usually higher than the voltage that makes the multiplication of 100, therefore the actual multiplication would be higher than 100. In addition to this, to suppress the perturbation of the sensitivity and the dark current caused by the temperature changes, the room temperature is maintained at 27 ºC by the air conditioners during the campaigns.

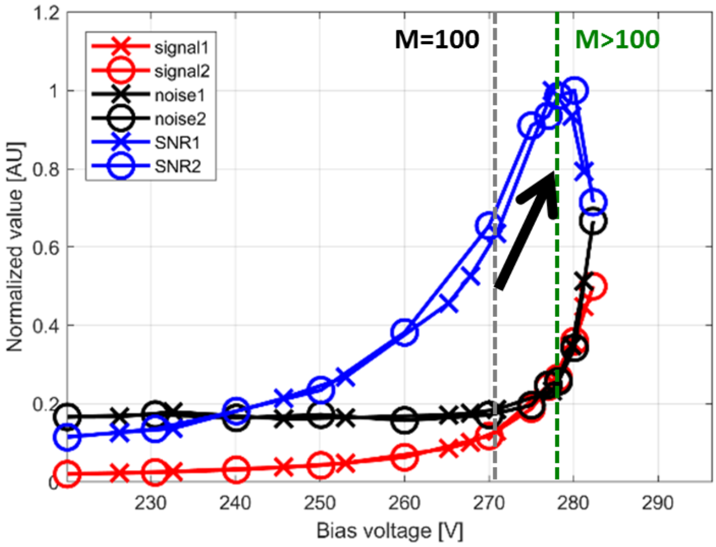

Figure 3.4 (Red) the signal level, (black) the noise level, and (blue) the signal-to-noise ratio about the bias voltage

3.2. Stray light reduction

The stray light reduction is one of the important issues in the Thomson scattering system on VEST, because the measured waveform of the stray light and the scattered light are overlapped in the time domain due to the small size of the vacuum vessel. However, the optical density of the filters is lower than 3 or 4 which are not high enough to block the stray light penetration. Even in case of filter 4 of which the bandwidth is the farthest from the laser wavelength, its transmission at 1064 nm is10% without the short pass filter.

The stray light is typically generated during the penetration of the vacuum windows or the incident rays outside the main beam path. Therefore, the optical alignment of between the laser injection optics and the chamber is important to remove the dominant source. For this reason, the large bellows with 10-inch CF flanges is inserted between the laser guiding tube and the vacuum window at the beam exit. The design and the installation are shown in Figure 3.5. The alignment of the beam with the dump is also important to reduce the stray light.

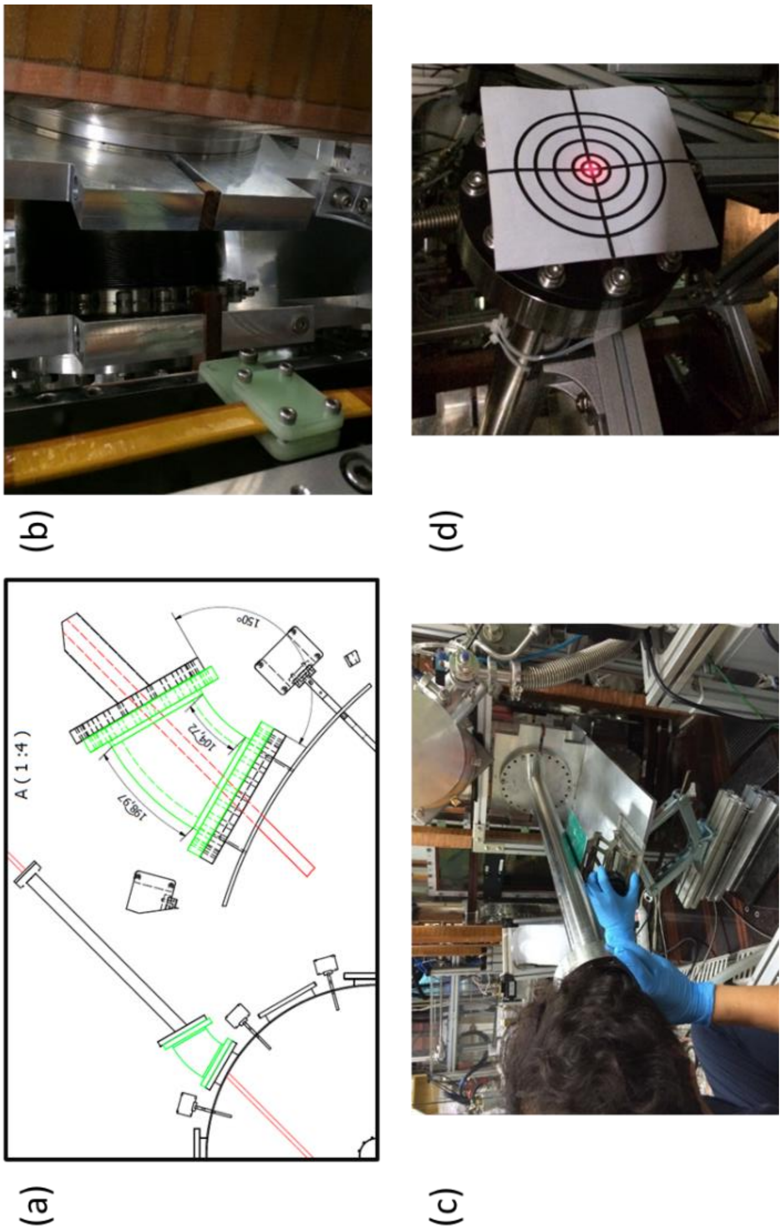

Figure 3.5 (a) The design of the bellows, (b) the bellows installed between the VEST (left side of the figure) and the guiding tube (right), (c) check of the beam path with naked eye, and (d) check of the beam path with accurately attached beam target.

In addition to the bellows and the dump, the in-vacuum components have been developed to reduce the reflections inside the stainless steel chamber [33]. Double-edged baffles [34, 35], a louvre [36], and a viewing dump [37] are illustrated in Figure 3.6, Figure 3.7, and Figure 3.8, respectively. The baffles were made by aluminum with black anodization and installed along the laser guiding tubes to trap the scattered light generated at the vacuum window. The inner diameter and the angle of the blades were optimized using LightTools program with the Gaussian beam that is modelled based on the measurement. In addition, the louvre made with a stack of hundreds of blades (OLFA BS-10B and SKB-7) was installed to prevent the reflection of the halo beam on the exit-side chamber wall. Similarly, the viewing dump, a crescent-shape blade of 130 layer, was installed behind the center stack limiter to reduce the direct reflection along the line of sight. The thickness of the each blade is 1 mm, and it was designed to cover an azimuthal angle of 52 degree of the center stack around the mid-plane. The 316 stainless steel was chosen as a material to minimize the perturbations on the magnetic field.

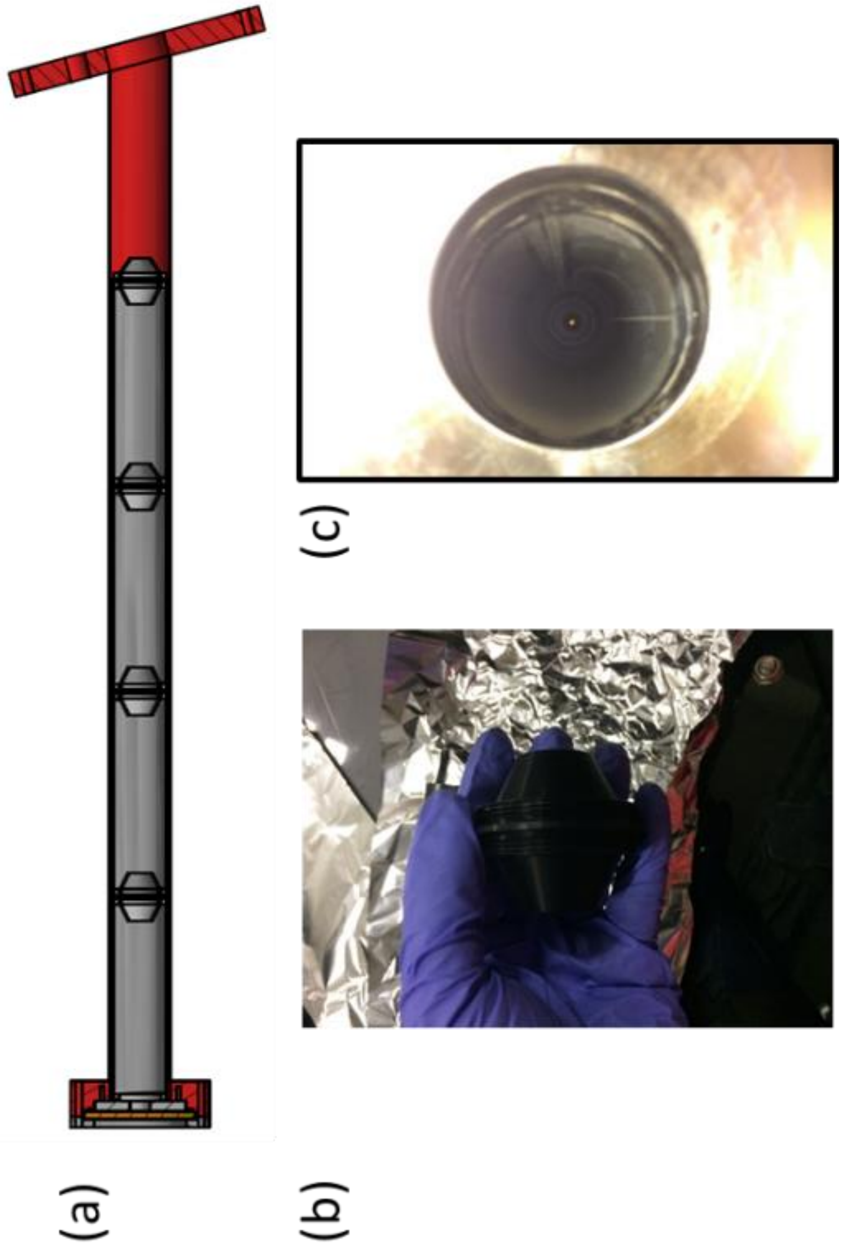

Figure 3.6 (a) The cross sectional view of the design of the double edged baffle, (b) the photo of the double edged baffle, and (c) the view along the beam path.

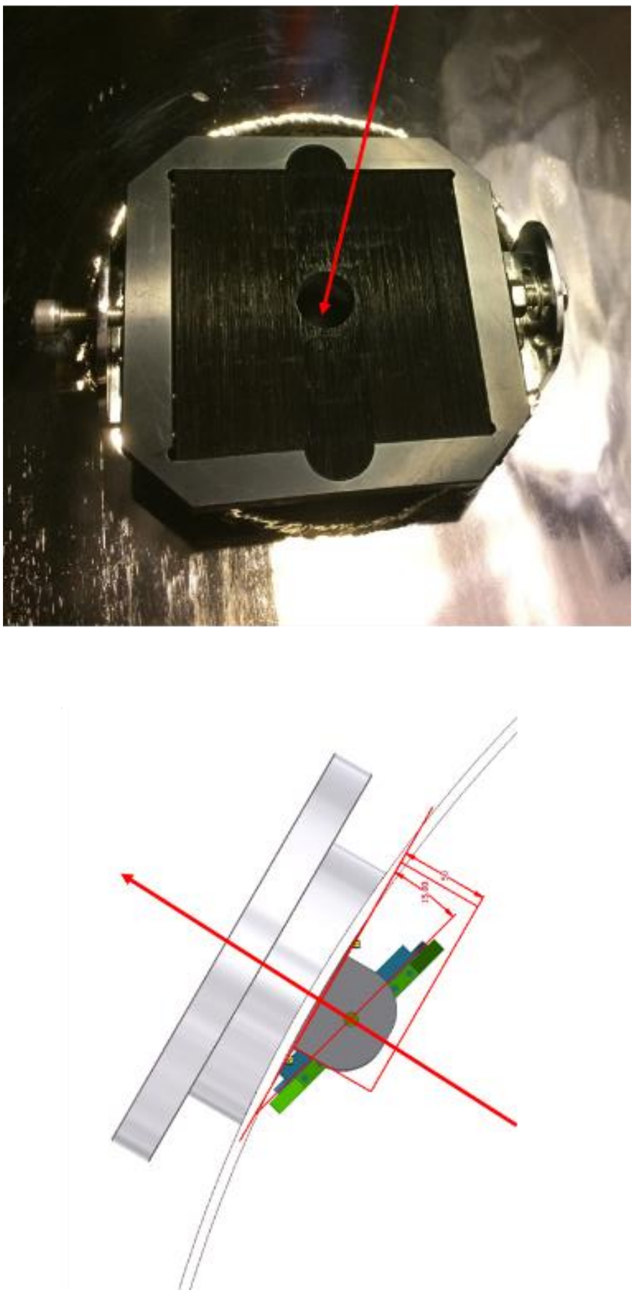

Figure 3.7 (Left) The design of the louvre and (right) the louvre.

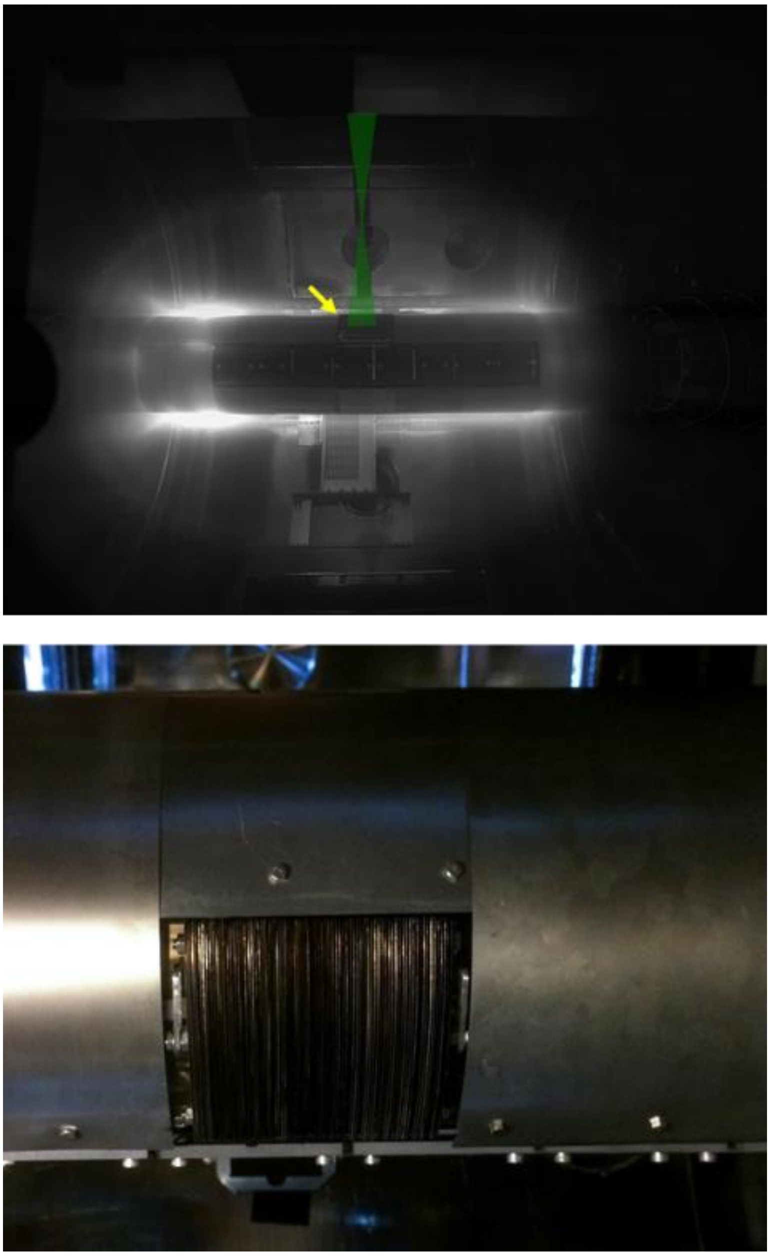

Figure 3.8 (Left) the viewing dump installed on the center stack and (right) the typical image of the fast camera during discharges. The yellow arrow indicates the viewing dump.

Although it is difficult to evaluate the performance separately, the amplitude of the measured stray light is reduced about two orders of magnitudes compared to the initial state of the stainless steel walls as depicted in Figure 3.9. As a result, the amplitude of the stray light penetrating filter 2, 3, and 4 became comparable to the TS signals so that the proper bit resolution could be used. Installation of the polarizing film was tried to filter out the randomly polarized stray light in front of the optical fiber. However, the use of the film was dismissed because the signal was lowered together due to the transmittance while the electrical noise remained the same.

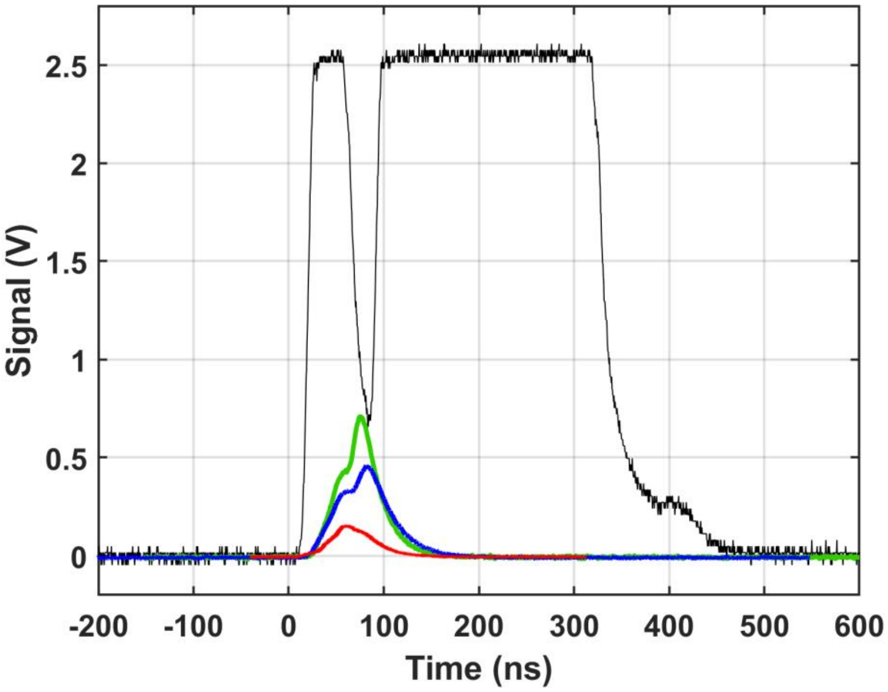

Figure 3.9 History of the signal of the stray light measured by an APD equipped with filter 1. Time flow is black-green-blue-red in order.

3.3. Noise reduction

The noise appeared in the Thomson scattering system on VEST could be categorized according to the type: DC offset, random noise, and pulse noise, as summarized in Table 3.1. Firstly, DC offset appeared in measuring plasmas has been removed by installation of the high pass filters behind the amplifier. Thus, it has been possible to use the maximum bit-resolution of the oscilloscope that was limited by the offset. Secondly, the main source of the pulse noise was Q-switching noise generated from the laser power supply. Due to the limited size of the laboratory, the distance between the laser power supply and the polychromator was shorter than 50 cm. Therefore, in order to reduce the intensity of the Q-switching noise, the length of the signal and power cables were shortened. In addition, the interference has been decreased after installation of the metal fabrics as a faraday shield, which is evident in Figure 3.10.

Table 3.1 Classification of the noises appeared in the Thomson scattering system on VEST

Type	Source	Solutions
DC offset	Plasma emission Electronics	Using batteries instead of power supply High pass filter (circuit) Fitting parameter
Random noise	Thermal noise Dark current Shot noise	Temperature control Multi-pulse averaging
Pulse noise	Electromagnetic interference	Shorten signal and power cables Using batteries Faraday shielding

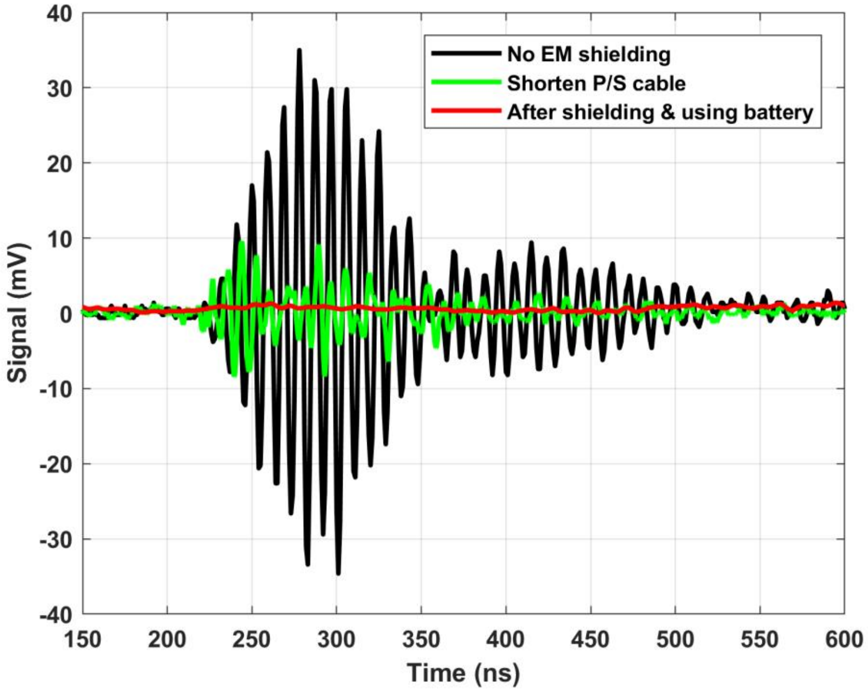

Figure 3.10 The typical Q-switching noise generated from the laser power supply (black) with no treatment, (green) with shortening cables, and (red) with shortening cables and the Faraday shielding.

Lastly, the random noises are decreased by averaging the multiple signals. It was checked that the random noise measured by the APDs with the same experimental setup as the Thomson scattering measurement is proportional to the square root of the number of averaging pulses as seen in Figure 3.11.

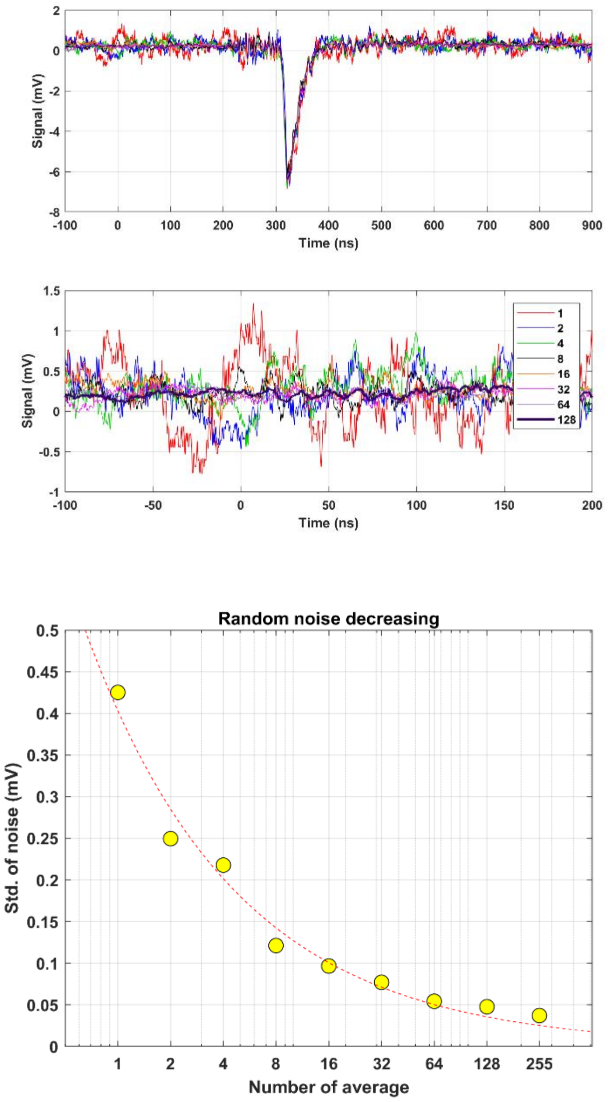

Figure 3.11 (Top) The total and (middle) noise part of the raw signals. (Bottom) The relation between the noise level and the number of average.

Chapter 4. Calibration of developed system

4.1. Spectral calibration

The electron temperature is determined by the measurement of Doppler broadening caused by the electron velocity distribution. Therefore, accurate spectral calibration is necessary to analyze the correct electron temperature of the measured plasmas. The spectral calibration is performed by using a stable tungsten lamp and a grating monochromator that is controllable by a computer. The responsivity is typically scanned from the wavelength of 800 nm to 1200 nm with 0.1 nm interval for the VEST polychromator. In order to compensate the spectral difference of the tungsten lamp, once again, the spectrum of the lamp is measured by a primarily calibrated spectrometer. Before the measurements, the bias voltage of each APD is optimized to have the maximum signal-to-noise ratio as mentioned in 3.1.2. The solid lines in Figure 4.2 represent the responsivity of each APD and the dashed lines are the normalized TS spectrum at the scattering angle of 130 degree for the electron temperature of 50 eV and 200 eV.

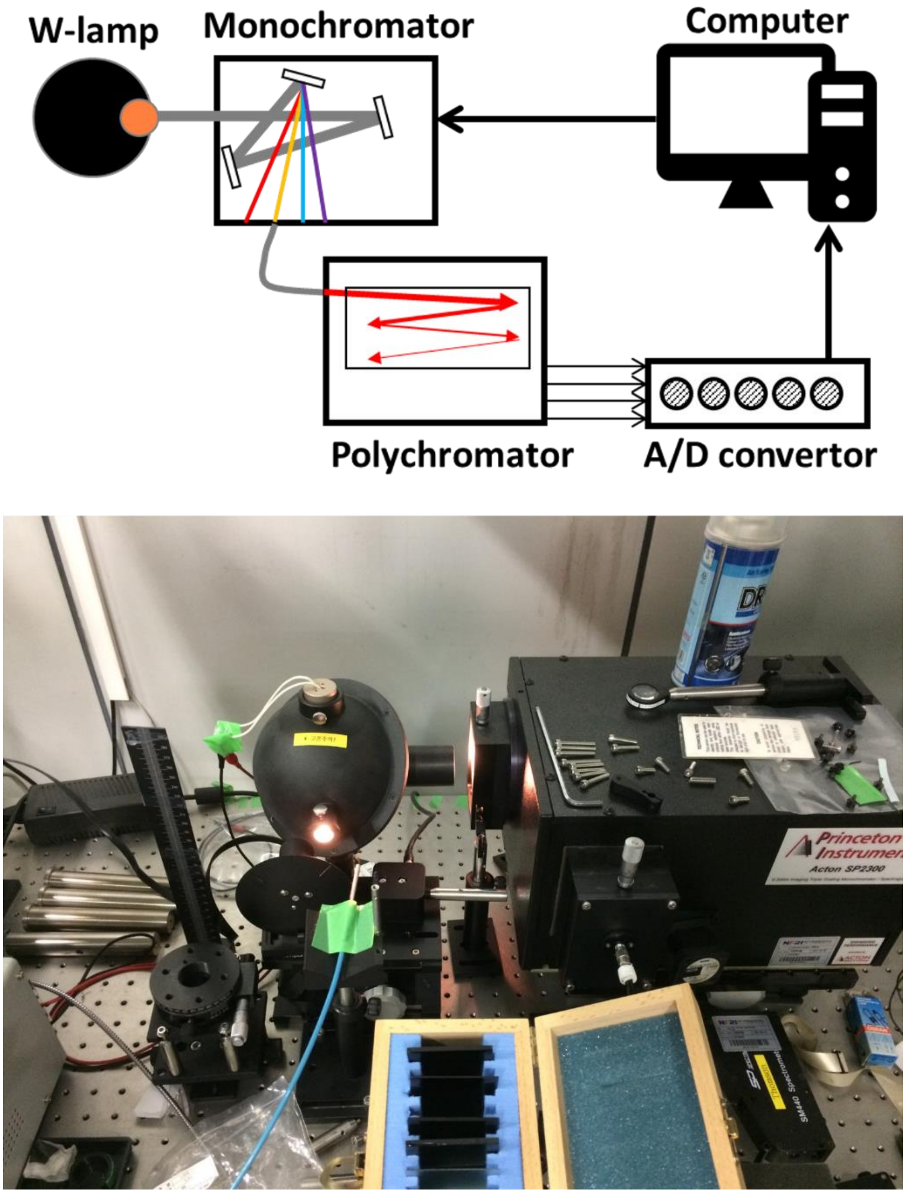

Figure 4.1 (Top) Schematic and (bottom) the photo of experimental set-up for the spectral calibration

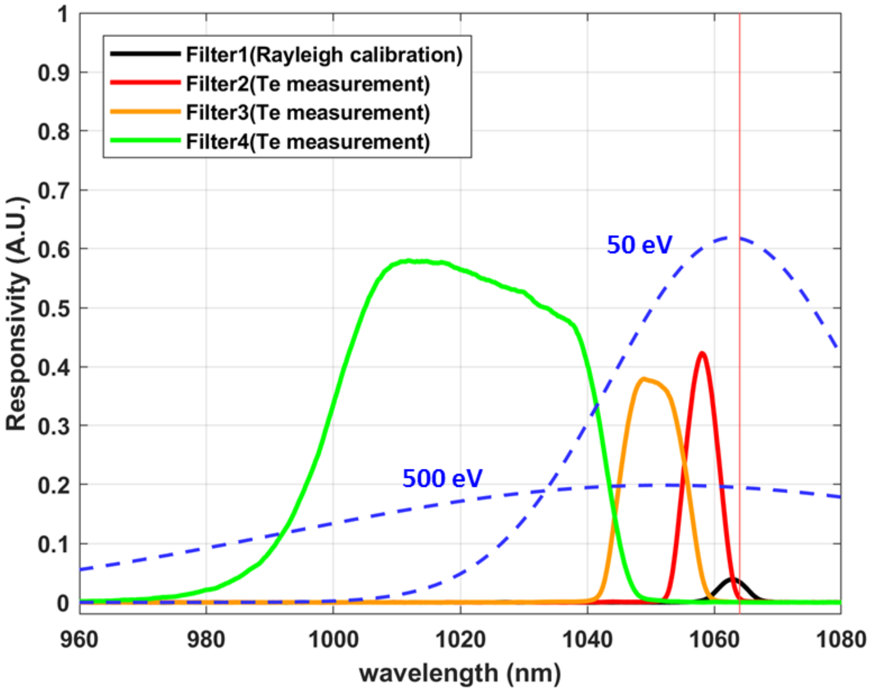

Figure 4.2 The results of the spectral calibration: the responsivity of the polychromator

4.2. Absolute calibration

Basic principle of the Thomson scattering diagnostic system is analyzing the ratio between the spectral channels. Therefore, absolute calibration of the system is necessary to obtain the absolute values of the electron density from the measured data. In other words, if the electron temperature and the density are given, the signal level of the Thomson scattering can be predicted after both the spectral and the absolute calibration.

Firstly, the theoretical system efficiency is estimated using the information of the APD and the amplifier. Figure 4.3 is the circuit diagram of the amplifier. The theoretical photon-to-voltage efficiency is calculated as following equations,

$$S_{out} = (N_{photon}\ \text{Q.E.})\ eMR_2G\frac{R_{osc}}{R_{osc}+R_5}$$

$$= 6.928\times10^{-5} N_{photon}(nV\cdot s)\ , \tag{4.1}$$

$$V_{out} = 6.928\times10^{-5} N_{photon}(nV\cdot s)\times 30.45(mV/nV\cdot s) = 0.0021N_{photon}\ . \tag{4.2}$$

From the result of (4.2), a quantum efficiency of 40% is used. And, the multiplication of the APD is set as 100 because it is difficult to measure the actual multiplication after optimization. According to a result of the estimation, 1 mV signal can be appeared with more than 474 photons.

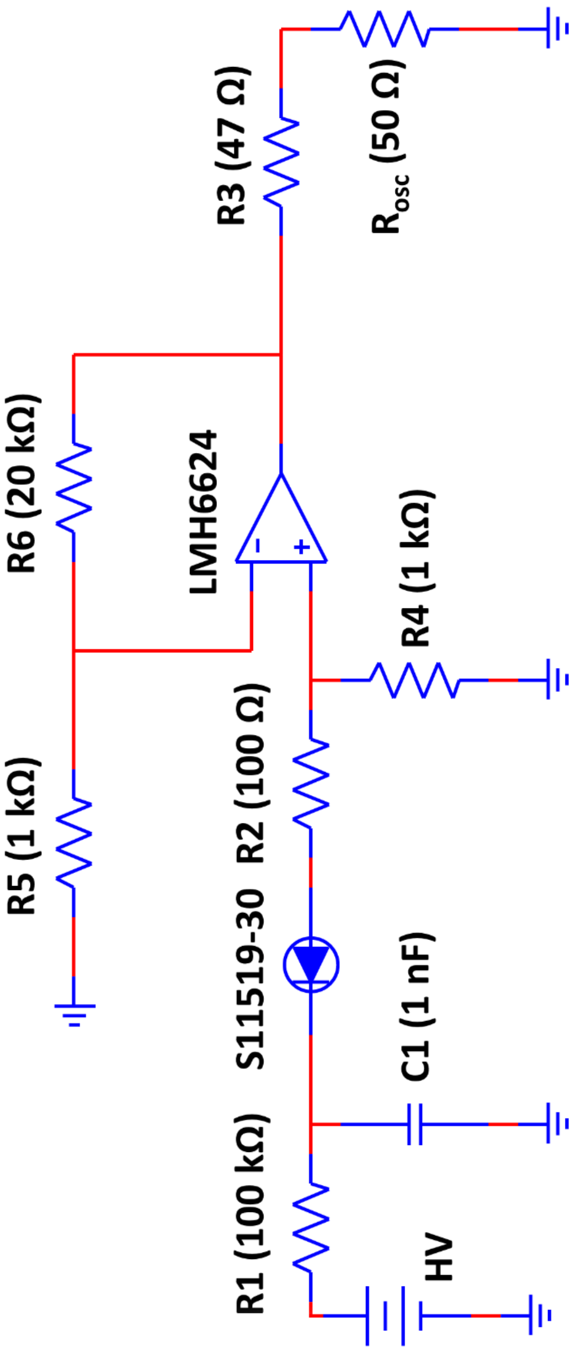

Figure 4.3 The circuit diagram of an amplifier for the APD.

Secondly, Rayleigh scattering is measured. Rayleigh scattering and rotational Raman scattering are typically used for the alignment and the calibration of the Thomson scattering systems by filling the vacuum chamber with the nitrogen gas. For example, KSTAR used Rayleigh scattering [13] and NSTX used both scatterings [38] for the absolute calibration. Generally, the Rayleigh scattering has the difficulty in measuring the scattering signals, since the wavelength of Rayleigh scattering is the same as that of the stray light, the laser wavelength. However, in the Thomson scattering system on VEST, the Rayleigh scattering signals and the stray light have been clearly distinguished, although they are overlapped. Since the stray light is quite reproducible, the subtracting the stray light is used to find the scattering signals like as removing the background light. Therefore, the Rayleigh scattering experiments are conducted to calibrate the total efficiency of the system. Besides, the raw signals could be used to find the waveform of the scattering signals. Left hand side of Figure 4.4shows the Rayleigh scattering signals measured for the various nitrogen pressures. The right figure shows linear increase of the peak voltage of the Rayleigh scattering signals about the pressure changes. In addition, it has been observed that the measured efficiency is about 60% higher than the theoretical efficiency calculated with M = 100. Note that the ratio of the peak voltage to the time-integral of the signal, η in Eq. (2.1), is a constant, since the pulse shapes of the normalized signals obtained from the different pressures are fitted with an identical function.

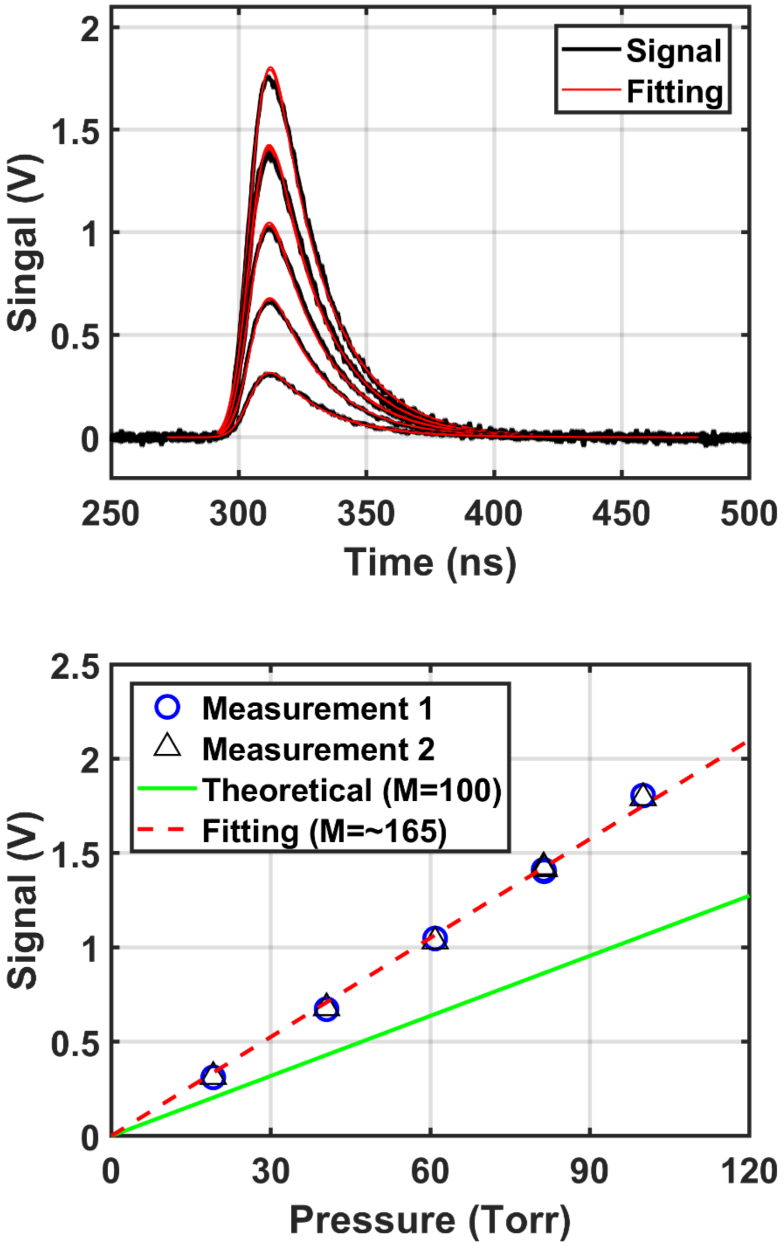

Figure 4.4 (Top) The Rayleigh scattering signals obtained by the stray light subtractions and the fittings. (Bottom) The linear fitting of the peak voltage of the scattering signals about the pressure in Torr.

The result of the Rayleigh scattering measurement is a ratio of a signal to the nitrogen pressure. In order to apply the result to Thomson scattering, the total cross section of the Rayleigh scattering is required. However, it cannot be found that the Rayleigh scattering cross section measured in the wavelength of 1064 nm. Therefore, the total cross section of the Rayleigh scattering was used as the value obtained by extrapolating the data measured at shorter wavelengths, as shown in Figure 4.5. [38, 39, 40, 41]. As an example, Figure 4.6 is the estimation of the expected signals for the given electron densities. The ratio of two scatterings used in computation is about 2030.

$$\frac{\sigma^{TS}}{\sigma^{RS}} = \frac{6.65\times10^{-29}}{3.28\times10^{-32}} \cong 2030 \,. \tag{4.3}$$

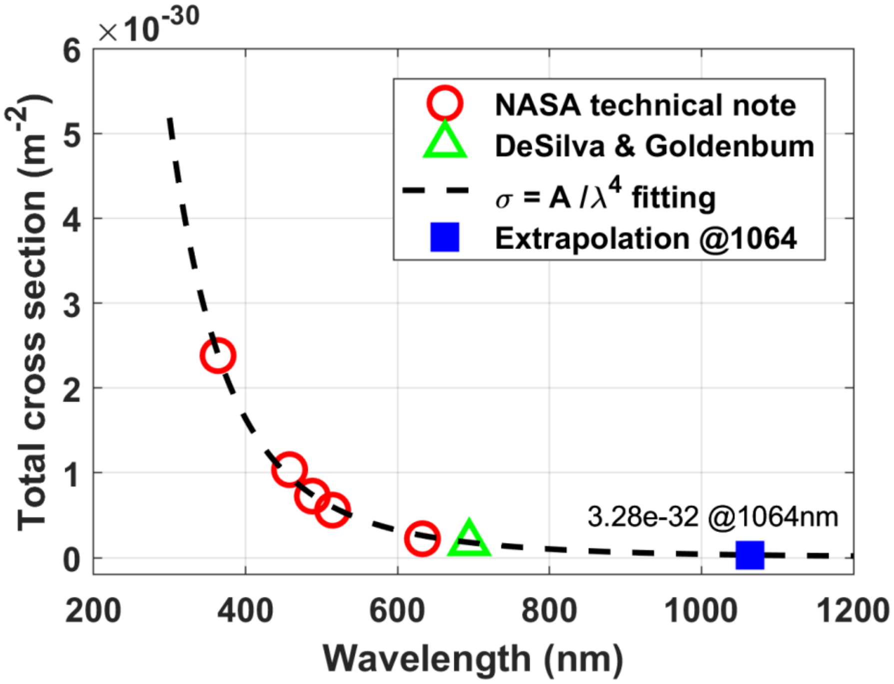

Figure 4.5 Extrapolation to the laser wavelength to find the total cross section of Rayleigh scattering.

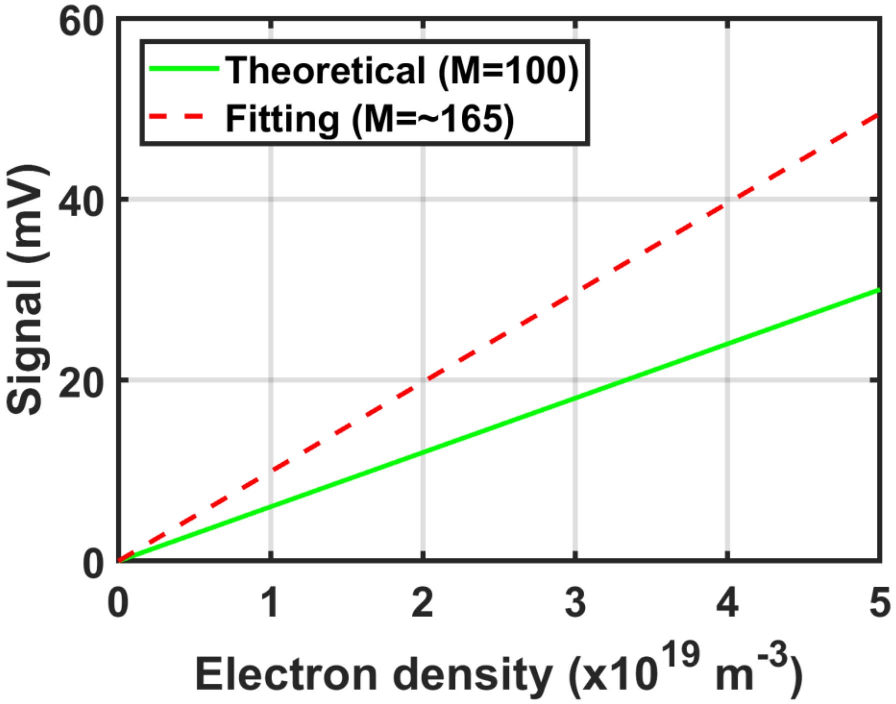

Figure 4.6 Expected signals for the electron density. Conversion from the pressure to the electron density is based on the ratio of the total cross section of Thomson scattering and Rayleigh scattering.

The Thomson scattering signals of *i*-th channel (i = 2-4) and the Rayleigh scattering signal of 1st channel are calculated theoretically as Eq. (4.4) and Eq. (4.5), respectively.

$$V_i^{TS}(t) = P_L^{TS}(t) n_e \Delta l \times \iint \frac{d\sigma_{TS}}{d\Omega} T(\lambda,\theta,d\Omega) R_i(\lambda) S(\lambda,T_e,\theta) d\lambda d\Omega \,. \qquad (4.4)$$

$$V_1^{RS}(t) = P_L^{RS}(t) n_{N_2} \Delta l \times \int \frac{d\sigma_{RS}}{d\Omega} T(\lambda_0, \theta, d\Omega) R_1(\lambda_0) d\Omega \,. \qquad (4.5)$$

P_L^{TS} and P_L^{RS} are the laser power of the incident laser of Thomson scattering and Rayleigh scattering, respectively. ΔL is the scattering length, and T is the total optical efficiency including the transmittance or the reflectance of the laser injection optics, collecting optics, and the optical fiber. In particular, T of the vacuum windows and the collecting lens are compensated using the measured results, shown in Figure 2.15, with interpolation. T_e is the electron temperature, λ is the wavelength, and λ_0 is the wavelength of the incident laser. n_e and n_{N2} are the density of the electron and nitrogen, respectively. $\frac{d\sigma_{TS}}{d\Omega}$ and $\frac{d\sigma_{RS}}{d\Omega}$ indicate the differential cross section of the Thomson scattering and Rayleigh scattering, respectively, where Ω is the solid angle of the collection lens. θ is the scattering angle and S is the sepctral density function which is the function of the electron temperature and the scattering angle. The integral over the wavelength of S is unity. Finally, R_i represents the responsivity of i-th channel considering the spectral sensitivity and multiplicatio of the APD with the amplifier gain. Here, the geometircal factors such as ΔL, θ, and Ω are common in the equations, the absolute values of the Thomson scattering signals can be calculated by dividing Eq. (4.4) by the time integral of Eq. (4.5).

$$V_i^{TS}(t,T_e,n_e) = \frac{\int V_1^{RS} dt}{n_{N2}} \frac{P_L^{TS}(t)}{\int P_L^{RS}(t)dt} \frac{\int \frac{d\sigma_{TS}}{d\Omega} d\Omega}{\int \frac{d\sigma_{RS}}{d\Omega} d\Omega} n_e \frac{\int R_i(\lambda) S(\lambda,T_e,\theta) d\lambda}{R_1(\lambda_0)} . \quad (4.6)$$

The first three terms of the right hand side of Eq. (4.6) are related with the absolute calibration. And, the terms behind the electron density is related with the spectral calibration. The integral over the solid angle is canceled out using the ratio of cross sections. The last term can be numerically calculated using the results in section 4.1. In conclusion, the expected signals for the APDs that measuring Thomson scattering at the plasma with given electron temperature and density are illustrated in Figure 4.7.

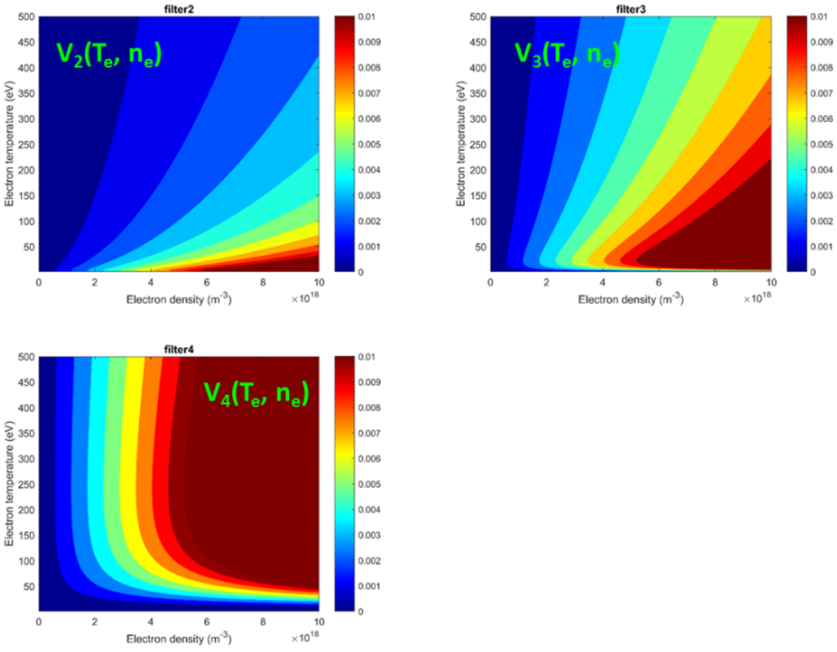

Figure 4.7 The estimation of the Thomson scattering signals in the unit of *V* for the filter channel 2, 3, and 4.

Since the APDs are coupled with the certain band pass filters, each channel has the sensitive range of the electron temperature corresponding to its own pass band at the fixed electron density. For instance, as the pass band of filter 2 is near 1064 nm, it responses to the low temperature range well. Unlike channel 2 and channel 3, channel 4 intensively responds to the far wavelength from the laser wavelength. Obviously, in the fixed electron temperature, the signals are proportional to the electron density and it is consistent to that the deduction of the electron temperature only depends on the ratio between the signals of the channels.

Chapter 5. Results of measurement

In this chapter, how to obtain the Thomson scattering signal from the measured raw signals would be explained. Then, the method to determine the most likely electron temperature and density from the intensities of the signal would be described. Finally, the measured results in KSTAR and VEST are presented in section 5.2 and section 5.3.

5.1. Extraction of Thomson scattering signals

Despite efforts to reduce the noise and the stray light, both the stray light and the Q-switching noise were still measured with the signal. In case of the stray light, it could be subtracted from the raw signals because the waveforms of the stray light remain almost same at the conditions with or without plasmas. On the other hand, the intensity and the phase of the Q-switching noise were not maintained. Therefore, it should be measured before every Thomson scattering signal measurement to minimize the difference between the signals and the background noise.

The signals measured in the APD with the filter 2, 3, and 4 are illustrated in Figure 5.1 (a). Blue curves are the raw signals containing the Thomson scattered photons, the random fluctuation of the plasma emission, the stray light, and the Q-switching noise. Red curves are the background signals; the signals measured under the same conditions in a vacuum environment instead of plasma. Subtracting the background signals from the raw signals yields signals with only the Thomson scattering components remaining, as shown by the black curve in Figure 5.1 (b). To find the accurate pulse waveform, the signal with high signal-to-noise ratio, which is measured from the Rayleigh scattering experiment, is used. As the pulse waveform function, a convolution of a Gaussian function and low pass filter characteristic of the amplifier circuit is employed as following [42],

$$V_{out}(t) = \int_{-\infty}^{t} \exp\left(\frac{(t - t_L)^2}{{\tau_L}^2} \right) \exp\left(-\frac{t - t'}{\tau_{amp}} \right) dt' \,. \tag{5.1}$$

The time constants of the Gaussian function and low pass filter characteristic of the amplifier are $\tau_L = 7.8\,ns$ and $\tau_{amp} = 20.3\,ns$, respectively.

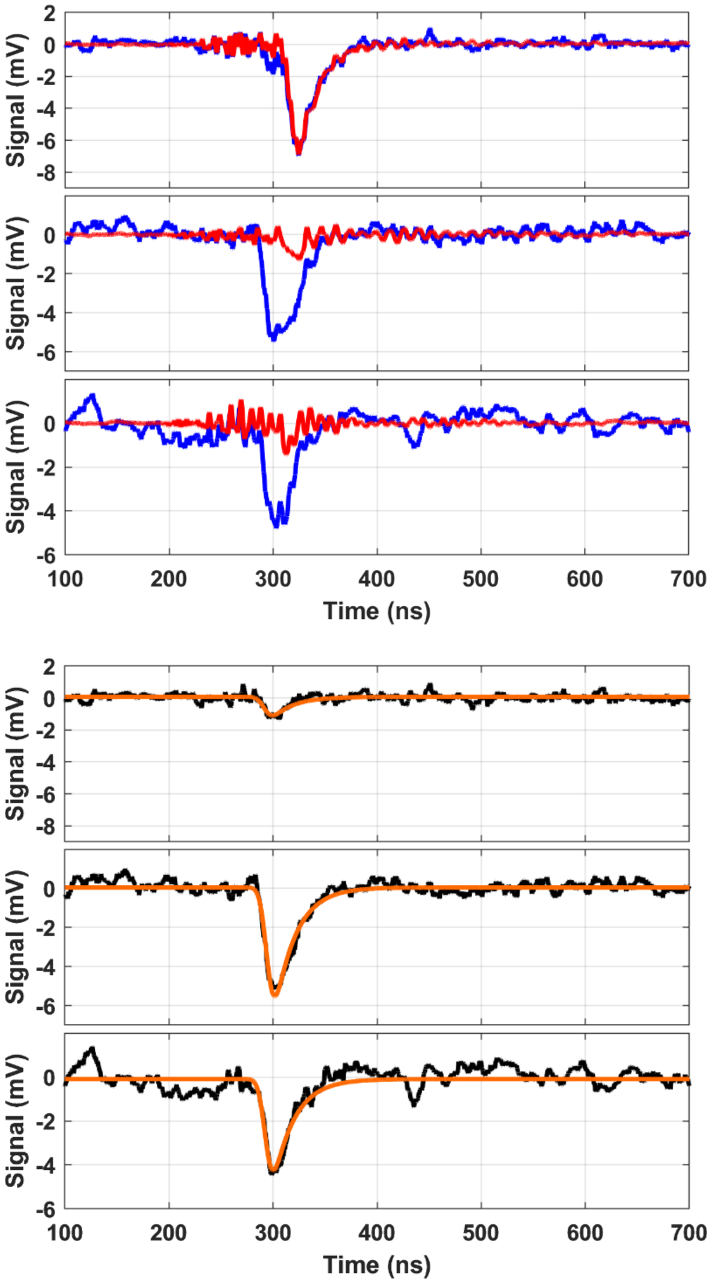

Figure 5.1 (Tob) The raw signals of the APDs measuring Thomson scattering signals. (Bottom) The background subtracted signals and fitting.

In case of low signal-to-noise ratio, the multi-pulse averaging is used to measure the signal by reducing the random noise level. As seen in the upper box of Figure 5.2, a meaningful signal could not be obtained from the raw signals because of the similar intensity of the scattering signal and the noise. Thus, the several plasma discharges of same scenario were repeated to accumulate the signals. After the averaging the signals, three pulses in this case, it was able to get the processed signal as shown in blue curves in the middle box of the figure. It can be found that the phase and the intensity of the Q-switching noise were slightly different between the averaged signal and the background signal. Similar to the analysis above, black curves could be obtained by subtracting the background signal from the averaged signals. Since not only the pulse waveform, but also the timing that the scattering signal should appears have been already known, the signal as low as $< 1\ mV$ could be found by the fitting.

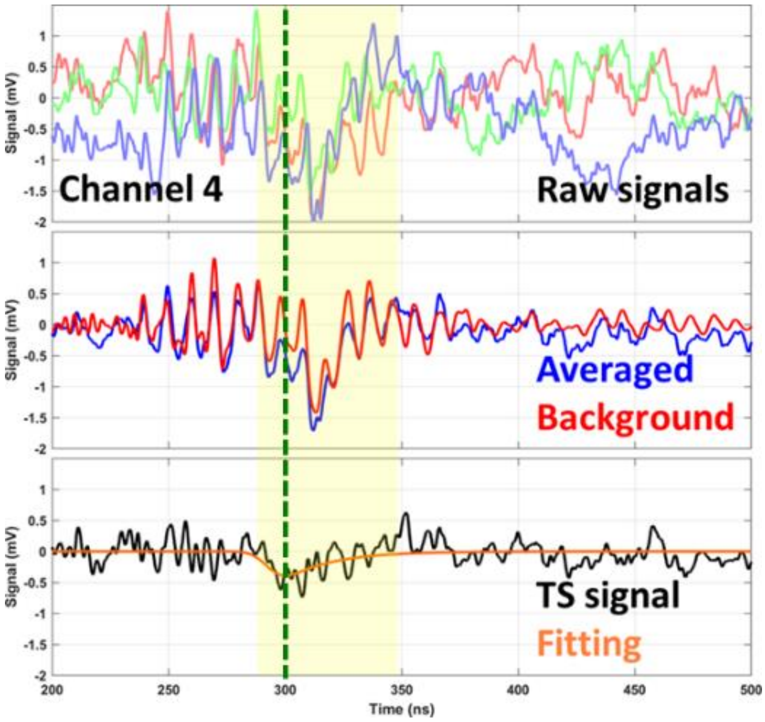

Figure 5.2 Extraction of the Thomson scattering signal by multi-pulse averaging in low signal-to-noise case

5.2. Determination of electron temperature and density

There are several ways to find the electron temperature and density: ratio evaluation method [11], minimum chi-squared [24, 31], neural network [43], and Bayesian statistical analysis [11, 44]. Among the methods, the Bayesian analysis method is chosen, since it has been considered that the analysis can handle the information as many as possible including the system performance and the noise. According to Bayes' theorem, the posterior probability is proportional to the likelihood function [45].

$$P(T_e, n_e \mid \{data\}, I) = \frac{P(\{data\} \mid T_e, n_e, I) P(T_e, n_e \mid I)}{P(\{data\} \mid, I)}, \tag{5.2}$$

The left hand side of Eq. (5.2) is the probability distribution function of the posterior and the first term of the numerator is the likelihood. The former is the probability to find the electron temperature and the density from the measured data with additional information such as the uncertainties. Similarly, the latter is the probability to find the measured data where the electron temperature, the density, and additional information are known. . In this method, T_e and n_e are determined by finding T_e and n_e that maximize the product of the likelihoods of channel 2, 3, and 4. As an example, assume that the signals are measured at the three channels: $V_2 = 1.5\, mV$, $V_3 = 2.8\, mV$, and $V_4 = 1.2\, mV$. Then, a contour can be determined from Figure 4.7 (a) so that the value is same as V_2. In the same way, contours for channel 2 and channel 3 can be determined. If the uncertainty is neglected, i.e. noise is zero, the possible electron temperature and density can be determined from a point of intersection like as Figure 5.3. However, because the signals contain the uncertainty as they are obtained from the noisy environments, the curves are not share at a certain single point.

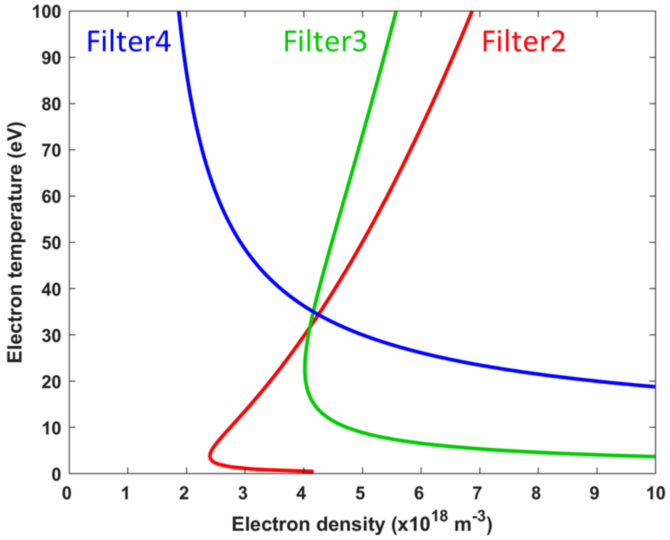

Figure 5.3 The contours that indicating the possible electron temperature and density with the given signals without noise.

In the real measurement, the signal is always contaminated by the noise. And, the distribution of the noise affects the analysis results. The histogram of the noise that measured by the APD is obtained as shown in Figure 5.4. The distributions of the noise amplitude have been well fitted to the normal distribution, and a standard deviation presents as a noise level. In Bayesian analysis of the VEST Thomson scattering diagnostic system, the standard deviations obtained from the noise distributions have been calculated by assuming the noises are Gaussian noise that following the normal distribution. Then, the probability density function of the noise can be combined as following

$$P(\{data\}|T_e,n_e,I) \propto \exp\left[-\frac{(V_{TS}^{measured}-V_{TS}^{theory})^2}{2\sigma_{noise}^2}\right], \tag{5.3}$$

where P is the probability distribution function of the likelihood. $V_{TS}^{measured}$, V_{TS}^{theory}, and σ_{noise} are the measured Thomson scattering signals, the theoretically expected signals using Eq. (4.6), and the measured noise distribution, respectively.

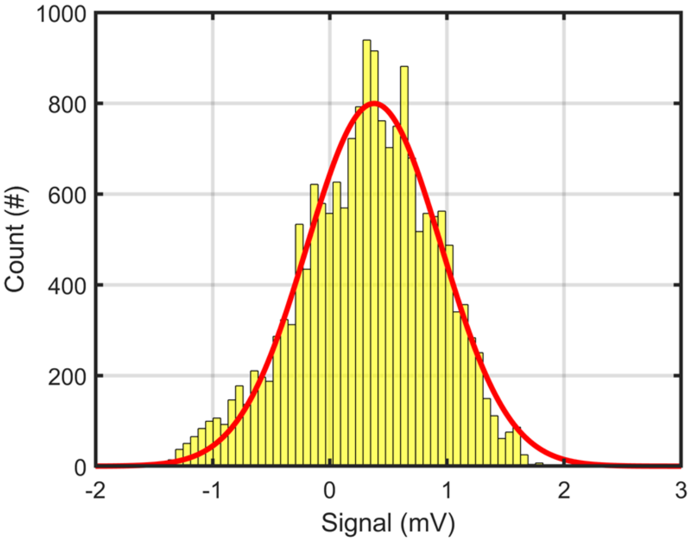

Figure 5.4 The histogram of the noise measured by an APD of the Thomson scattering system on VEST

Figure 5.5 represents the probability distribution function of the three channels expressed as two-dimensional plot. Because of the existence of the noise, the contours of Figure 5.3 have uncertainty region rather than the line with zero width. Similar to the point of intersection, the overlapped region of the probability density functions indicates the possible region of the electron temperature and density exist. From the Eq. (5.3), the total probability function combined with the functions of three channels can be expressed by following equation.

$$P(\{data\}\,|\,T_e,n_e,I)=\prod_{i=2}^{4}P(\{data_i\}\,|\,T_e,n_e,I)\propto\exp\left[-\sum_{i=2}^{4}\frac{(V_{TS,i}^{measure}-V_{TS,i}^{theory})^2}{2\sigma_{noise}^2}\right]. \quad (5.4)$$

The most likely electron temperature and density could be found from the result of Eq. (5.4), which is illustrated in Figure 5.6. When the noise level of certain channels increases, the region of each channel will be broader. At the same time, it affects the probability distribution function of the total likelihood to be broader, i.e. it means that the error bar or the measurement error become larger.

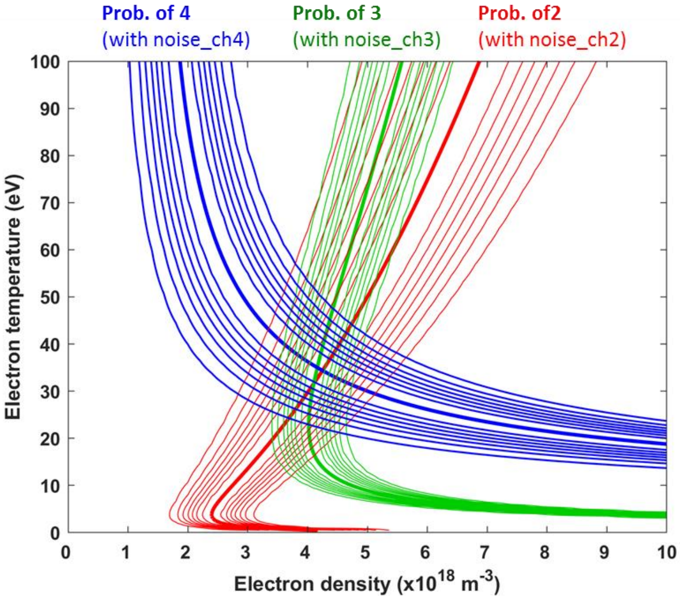

Figure 5.5 The possible regions that indicating the electron temperature and density exists

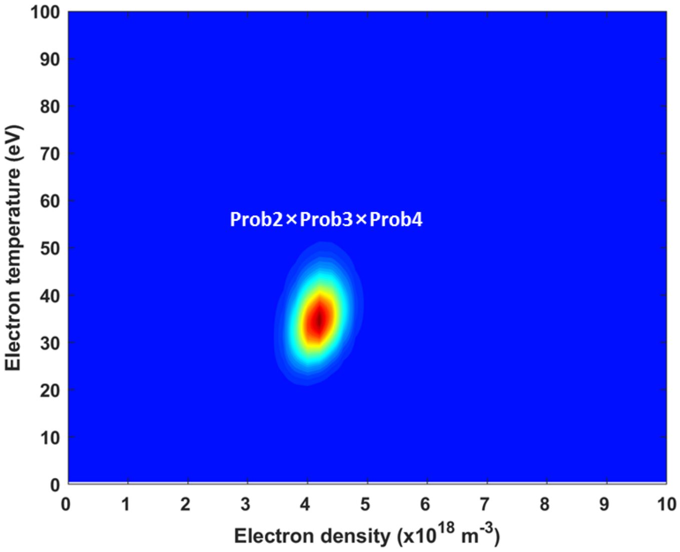

Figure 5.6 The normalized distribution function of the total likelihood that calculated with the TS signals and the measured noise distribution. (Lower at blue and higher at red)

The error region of the measurement is determined by integration of the normalized distribution function with the electron temperature and density. The most confident method is the two-dimensional integration of the distribution function as shown in Figure 5.7. However, in many cases it is difficult to determine an error bar of a single parameter, because the error region is correlated each other. Therefore, in the Thomson scattering system on VEST, the relatively simple method is usually interested to find the error bar of the distribution function.

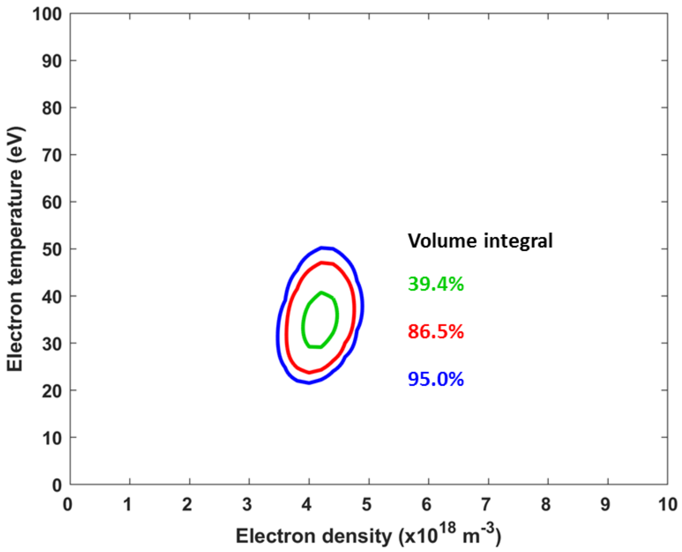

Figure 5.7 The contours of the confident levels of 39.4% (one standard deviation), 86.5% (two standard deviation), and 95%.

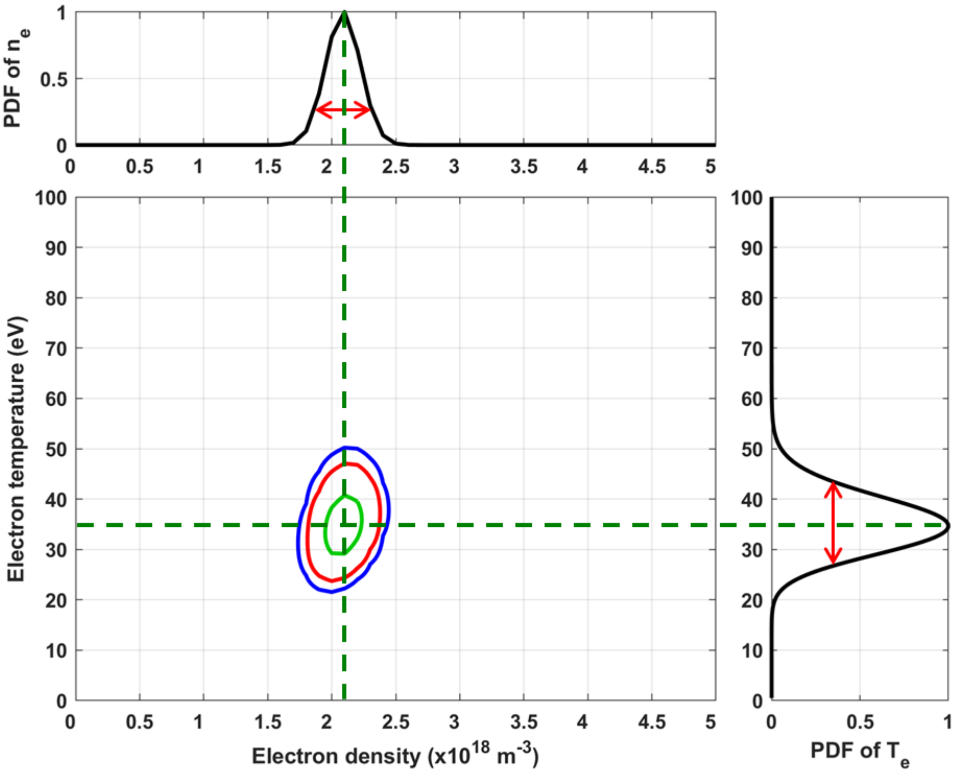

Figure 5.8 Integration to find the error bar of the single parameter. (Top) The probability distribution function of the electron density and (right) the function of the electron temperature.

To validate the performance of the polychromator and the determination method using Bayesian analysis, the measurement of Thomson scattering using the VEST polychromator is conducted at KSTAR. In case of KSTAR Thomson scattering system, the repetition rate of the laser is 20 Hz. Besides, not only a laser energy, but also electron densities of the plasmas are much higher than VEST plasma. Thus, it was possible to obtain a sufficient number of data with high SNR at a single discharge. One snapshot of the number of raw signal is illustrated in Figure 5.9. At the time of the measurement in

KSTAR, a new digitizer had been tested for upgrade the data acquisition systems [46]. Therefore, the unit of the ordinate of the figure is not *V*. The hundreds of signals are fitted with the same waveform function Eq. (5.1) with the similar time-constants of the laser. According to the measured results as shown in Figure 5.10, the plasma current is controlled to maintain the target current. In addition, the plasma position and size are well controlled which are evident in the equilibrium reconstruction results such as the minor and major radii. It means that the Thomson scattering system measured a plasma being held in a fixed position. The electron temperature measured by the KSTAR polychromator depicted with green in the figure is distributed at 100-200 *eV* with the quite large number spikes. The electron temperature measured by VEST polychromator is also distributed within 100-200 e*V*, but, with relatively smaller perturbation than KSTAR. This result is attributed to that the VEST polychromator has been designed to operate in lower temperature regions than the KSTAR polychromator.

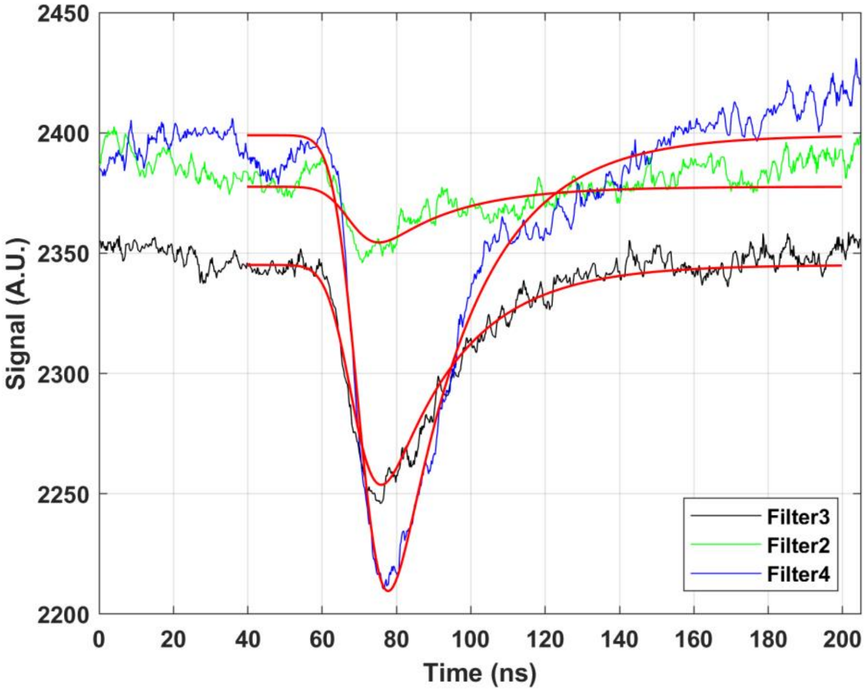

Figure 5.9 Raw signals measured by the VEST polychromator at the KSTAR Thomson scattering system

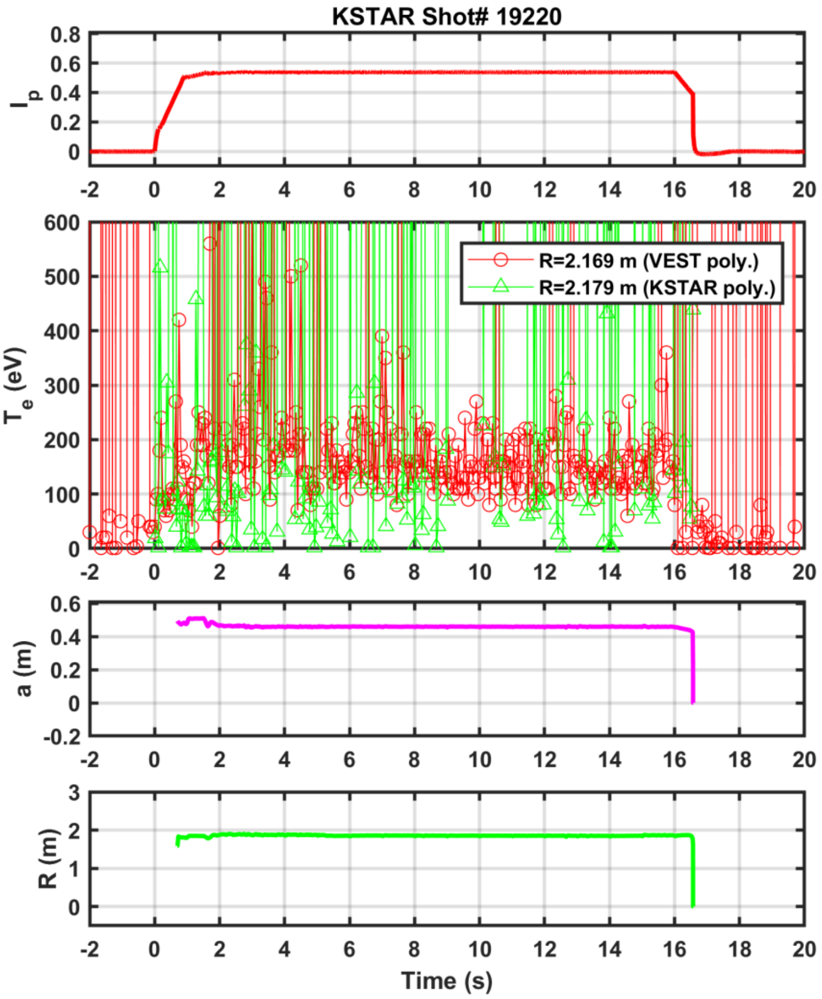

Figure 5.10 (a) The Plsama current, (b) the electron tempreature measured by Thomson scattering diagnostics, (c) the minor radius, and (d) the major radius of shot# 19220.

5.3. Measurement on VEST

For measuring the electron temperature and density, the Thomson scattering diagnostics on VEST requires shot-to-shot measurement of multiple discharges since the pulse duration of the plasmas are shorter than the repetition period of the laser. For that reason, the experiments are performed repetitively with an identical shot scenario. Firstly, the discharge is initiated by the pre-ionization using 6 kW electron cyclotron (EC) wave with the trapped particle configuration [47]. Then, the plasma current is ramped up by the loop voltage up to 80 kA, and it is slowly ramped down after t = 309 ms as seen in Figure 5.11(a). The size and the position of the plasmas are controlled by the pre-set poloidal field coil currents. In this scenario, the plasma boundary is determined by outboard limiters at the low filed side, R = 0.76 m. The time evolution of the global parameters such as a major radius, a minor radius and an elongation (κ) can be calculated by VFIT, an EFIT-like equilibrium reconstruction code with considerations for VEST. It can be seen that the overlaps of the radii and the elongation obtained from the multiple experiments exhibit similar trends in the figure (b) and (c). In addition, the overlapped diamagnetic flux signals depicted in the figure (d) also support the reproducibility of the experiments. The stored energy can be estimated from the diamagnetic flux measurement using the additional equilibrium parameters such as magnetic fields and shaping factors [48]. Since the ohmic heating power (> 400 kW) was much higher than the EC heating power (6 kW), in the scenario, the plasma could be considered as ohmic plasmas. Thus, it can be expected that both the diamagnetic flux and the stored energy would change following the plasma current.

The Thomson scattering measurements at this discharge yielded two conclusions. The first is that when the electron density is higher than about 2×10^{18} m^{-3}, meaningful results can be obtained through one experiment. At lower densities, signals have been obtained by averaging various experimental results to reduce the background noise. The second is that the internal stored energy measured through a diamagnetic loop is consistent with the results of the Thomson scattering measurements. Although it is difficult to compare the absolute value between the volume-averaged properties measured by the diamagnetic loop and the local information obtained by the Thomson scattering diagnostic system, both measurements tend to increase as the plasma current increases.

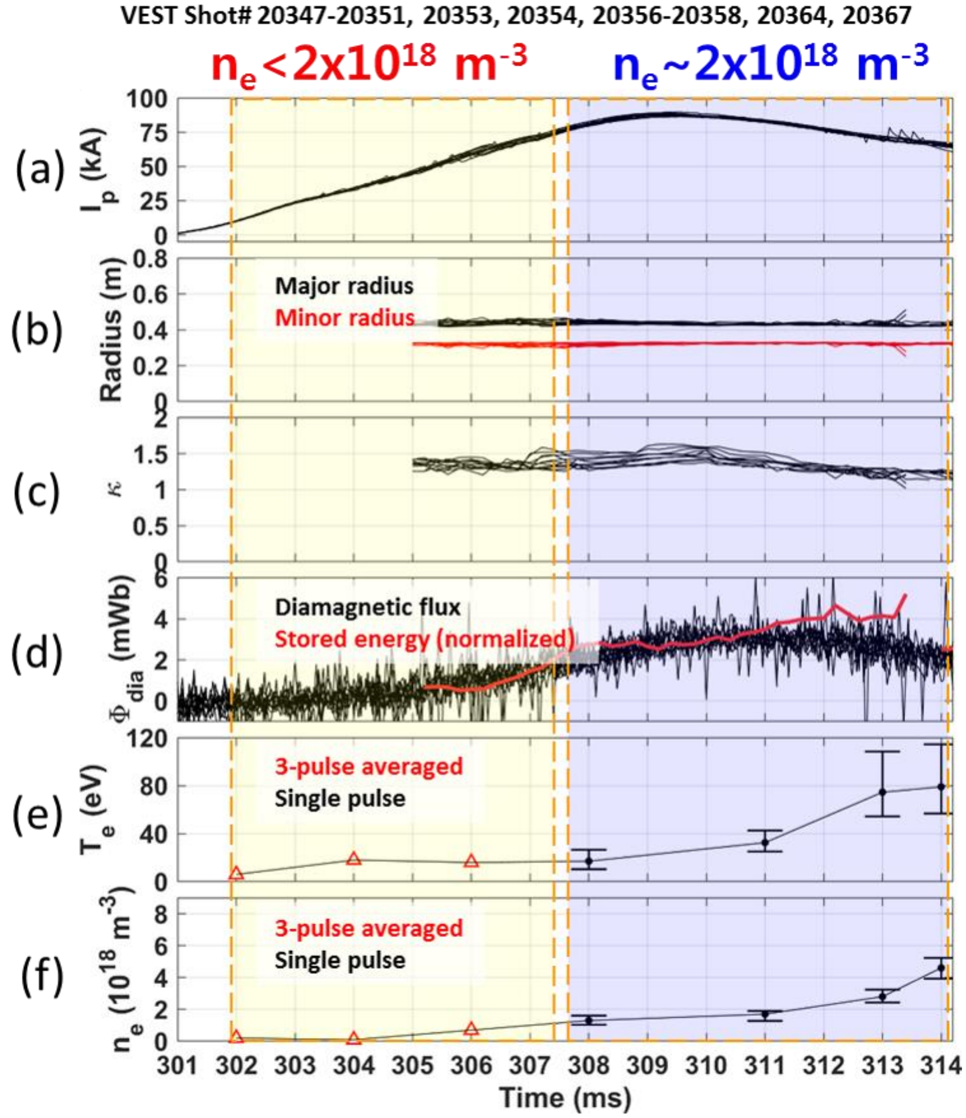

Figure 5.11 (a) The plasma current, (b) the major and minor radii, and (c) the elongation analyzed by equilibrium reconstruction. (d) The diamagnetic measursement results and the normalized stored energy. (e) The electron temperature and (f) the electron density measured by the Thomson scattering diagnostic system.

Chapter 6. Conclusion

The design, development, and optimization of the Thomson scattering diagnostic system on VEST was investigated in this dissertation. The study was quite challenging, because it utilized the laser with the energy of 0.85 J and there were compromises due to the limited budget. Therefore, the study was focused on maximizing SNR to increase the feasibility of the measurement. Each part of the system is carefully developed to minimize the optical loss and maximize the optical efficiencies. The fundamental wavelength of the laser was used to avoid the frequency doubling. And, the large collecting optics is developed to measure the core plasmas around the major radius of 0.23-0.5 m with the similar performance. In the polychromator, the APDs with high sensitivity near the laser wavelength are adopted and operated in the optimum bias voltage. The low cost commercial band pass filters that penetrating the stray light and having poor bandwidth make difficult to analyze the measured signals. However, they were overcome by development of the components for the stray light reduction and by optimizing the filter placement order with the relative error analysis. In the meantime, various noises appeared with the scattering signals were reduced after classifying it with the offset, the random noise, and the electromagnetic interference. The absolute calibration of the system was performed by Rayleigh scattering experiments with the nitrogen pressure up to 100 Torr. The developed system successfully measured the Thomson scattering signals from the VEST ohmic plasmas, and the measured electron temperature and density were consistent to the time trend of the stored energy.

The developed system cannot provide the radial profiles and the time evolution without repetitive experiments so far. It is necessary to be improved to provide the time evolution of the profiles of the single discharge. The upgrade plans and directions towards the advanced TS diagnostic system for VEST are described in Chapter 7.

Chapter 7. Future work

The current TS diagnostic system was developed with a focus on building infrastructures and acquiring signals processing and analysis techniques. However, the ultimate role of the system is to provide the time evolution of the radial profile of the electron temperature and density for the interpretation of the experimental results. Therefore, the system needs to be improved both the time resolution and the spatial resolution.

First, the time resolution is limited by the repetition rate of the pulse laser. Recently, pulse lasers with the repetition rate of > 20-50 Hz have been developed. But, they are still insufficient to measure the VEST plasmas with the pulse duration of 10-20 ms. To overcome the limitations, we planned to introduce a new customized laser: bust mode Nd:YAG laser produced by BeamTech, China. It generates 10 sub-pulses every 2 s with the repetition rate of 1 kHz. The energy of each sub-pulse is 2 J, which is over twice of that of the current laser. Therefore, it is expected that the utilizing this laser not only improves the time resolution, but also increases SNR. To measure the burst signals of the laser, an upgrade of the digitizer is also required. It is planned to test the same model as the digitizer (CAEN V1742 5 GS/s, 12-bit switched capacitor digitizer with 32 channels) that was equipped on KSTAR TS system [46], so that the signals of 100 ns can be recorded 10 times every 1 ms.

It is relatively simple to measure the radial profile as it depends on the number of the measurement location with additional optical fibers and the polychromators. However, it will be difficult to increase the polychromators in a short time, because the APDs and the interference filters are expensive. As shown in this dissertation, maximizing the efficiency of each APD and optimizing the placement order of commercial filter sets will reduce the required costs. Currently, it is planned to increase the number of polychromators, one polychromator per a year. For the electron temperature up to 200 eV, a polychromator requires 4 channels of digitizer, therefore, the new digitizer can cover up to 8 polychromators.

In addition, a method of increasing the scattering length by using optical fiber bundles can be proposed when if the low target electron density is expected due to the edge measurement or discharge scenarios.

Bibliography

[1] K. Chung, Y. An, B. Jung, H. Lee, J. Dang, J. Lee, J. Yang, J. Jo, D. Choi, Y.-G. Kim, Y.-S. Na and Y. Hwang, “Initial plasma start-up using partial solenoid coils in Versatile Experiment Spherical Torus (VEST),” *Fusion Engineering and Design,* vol. 88, pp. 787-790, 2013.

[2] Y. An, J. Lee, H. Lee, J. Jo, B. Jung, K. Chung, Y.-G. Kim, J. Jo, J. Yang, Y.-S. Na, T. Hahm and Y. Hwang, “Plasma start-up design and first plasma experiment in VEST,” *Fusion Engineering and Design,* Vols. 96-97, pp. 274-280, 2015.

[3] J. Lee, K. Chung, Y. An, J. Yang, Y.-G. Kim, B. Jung, Y. Hwang and Y.-S. Na, “Design and commissioning of magnetic diagnostics in VEST,” *Fusion Engineering and Design,* vol. 88, pp. 1327-1331, 2013.

[4] Y. Kim, Y.-J. Shi, J. Yang, S. Kim, Y.-G. Kim, J. Dang, S. Yang, J. Jo, S.-G. Oh, K. Chung and Y. Hwang, “Electron density profile measurements from hydrogen line intensity ratio method in Versatile Experiment Spherical Torus,” *Review of Scientific Instruments,* vol. 87, p. 11E540, 2016.

[5] D. J. Griffiths, Introduction to electrodynamics 3rd edition, New Jersey: Prentice Hall, 1999.

[6] K. Warner and G. M. Hieftje, “Thomson scattering from analytical plasmas,” *Spectrochimica Acta,* vol. 57, pp. 201-241, 2002.

[7] I. H. Hutchinson, Principles of Plasma diagnostics, 2nd ed., Cambridge University Press, 2005.

[8] D. H. Froula, S. H. Glenzer, N. C. Luhmann, Jr. and J. Sheffield, Plasma Scattering of Electromagnetic Radiation: Theory and Measurement Techniques, Elsevier Inc., 2011.

[9] S. L. Prunty, “A primer on the theory of Thomson scattering for high-temperature fusion plasmas,” *Physica Scripta,* vol. 89, p. 128001, 2014.

[10] T. Matoba, T. Itagaki, T. Yamauchi and A. Funahashi, “Analytical Approximatinos in the Theory of Relativistic Thomson Scattering for High Temperature Fusion Plasma,” *Japanese Journal of Applied Physics,* vol. 18, no. 6, pp. 1127-1133, 1979.

[11] R. Fischer, C. Wendland, A. Dinklage, S. Gori, V. Dose and W7-AS team, “Thomson scattering analysis with the Bayesian probability theory,” *Plasma Physics and Controlled fusion,* vol. 44, pp. 1501-1519, 2002.

[12] N. J. Peacock, D. C. Robinson, M. J. Forrest, P. D. Wilcock and V. V. Sannikov, “Measurement of the Electron Temperature by Thomson Scattering in Tokamak T3,” *Nature,* vol. 224, p. 488, 1969.

[13] J.-H. Lee, S. Oh, H. Wi, W. Lee, K. Kim, KSTAR team, I. Yamada, K. Narihara and K. Kawahata, “Tangential Thomson scattering diagnostic for the KSTAR tokamak,” *Journal of Instrumentation,* vol. 7, p. C02026, 2012.

[14] T. Yamaguchi, A. Ejiri, J. Hiratsuka, M. Hasegawa, Y. Nagashima, K. Narihara, Y. Takase, H. Zushi and the QUEST group, “Electron Temperature Measurement on QUEST Spherical Tokamak by Thomson Scattering System,” *Plasma and Fusion Research,* vol. 8, p. 1302001, 2013.

[15] H. Togashi, PhD Thesis, University of Tokyo, 2017.

[16] R. Scannell, M. J. Walsh, P. G. Carolan, A. C. Darke, M. Dunstan, R. B. Huxford, G. McArdle, D. Morgan, G. Naylor, T. O'Gorman, S. Shibaev, N. Barratt, K. J. Gibson, G. J. Tallents and H. R. Wilson, “Design of a new Nd:YAG Thomson scattering system for MAST,” *Review oF Scientific Instruments,* vol. 79, p. 10E730, 2008.

[17] D. J. Schlossberg, N. L. Schoenbeck, A. S. Dowd, R. J. Fonck and J. I. Moritz, “A Thomson scattering diagnostic on the Pegasus Toroidal experiment,” *Review of Scientific Instruments,* vol. 83, p. 10E336, 2012.

[18] E. Yatsuka, M. Bassan, T. Hatae, M. Ishikawa, T. Shimada, G. Vayakis, M. Walsh, R. Scannell, R. Huxford, P. Bilkova, P. Bohm, M. Aftanas and K. Itami, “Progress in development of the ITER edge Thomson scattering system,” *Journal of Instrumentation,* vol. 8, p. C12001, 2013.

[19] H. Tojo, T. Hatae, T. Sakuma, T. Hamano, K. Itami, Y. Aida, S. Suitoh and D. Fujie, “Design of collection optics and polychromators for a JT-60SA Thomson scattering system,” *Review of Scientific Instruments,* vol. 81, p. 10D539, 2010.

[20] R. Pasqualotto, P. Nielsen and L. Giudicotti, “The new RFX Thomson scattering system,” *Review of Scientific Instruments,* vol. 72, p. 1134, 2001.

[21] L. A. Berni and B. F. C. Albuquerque, “Stray light anlysis for the Thomson scattering diagnostic of the ETE Tokamak,” *Review of Scientific Instruments,* vol. 81, p. 123504, 2010.

[22] L. Frassinetti, M. N. A. Beurskens, R. Scannell, T. H. Osborne, J. Flanagan, M. Kempenaars, M. Maslov, R. Pasqualotto, M. Walsh and JET-EFDA Contributors, “Spatial resolution of the JET Thomson scattering system,” *Review of Scientific Instruments,* vol. 83, p. 013506, 2012.

[23] H. photonics, *"IR-enhanced Si APD" S11519 series datasheet, update: Nov. 2013.*

[24] J. Hiratsuka, PhD Thesis, University of Tokyo, 2013.

[25] S. A. Self, “Focusing of spherical Gaussian beams,” *Applied Optics,* vol. 22, no. 5, p. 658, 1983.

[26] R. Scannell, PhD Thesis, University College Cork, 2007.

[27] K. T. Y. Liao, Phd Thesis, The University of Texas at Austin, 2014.

[28] J.-H. Lee, S. Oh, H. Wi, Y. Oh, I. Yamada, K. Narihara, K. Kawahata and J. Jeon, "Conceptual design of new polychromator on Thomson scattering system to measure Zeff," *Review of Scientific Instruments,* vol. 83, p. 10E334, 2012.

[29] Y.-G. Kim, J.-H. Lee, J. Lee, Y. An, J. Dang, J. Jo, H. Lee, K.-J. Chung, Y. Hwang and Y.-S. Na, “Design of a Thomson scattering diagnostic system for VEST,”

Fusion Engineering and Design, Vols. 96-97, pp. 882-886, 2015.

[30] L. Yang, B. Wan, J. Zhao, Q. Hu, Y. Jia, X. Xi, X. Han and Q. Zang, “Design of Thomson Scattering Diagnostic System on EAST,” *Plasma Science and Technology,* vol. 3, p. 12, 2010.

[31] M. Maslov, M. N. A. Beurskens, J. Flanagan, M. Kempenaars and JET-EFDA Contributors, “Note: Statistical errors estimation for Thomson scattering diagnostics,” *Review of Scientific Instruments,* vol. 83, p. 096106, 2012.

[32] Characteristics and use of Si APD (Avalanche Photodiode), Vols. Technical Information SD-28, HAMAMATSU.

[33] M. P. Alonso, L. A. Berni, J. H. Severo, F. O. Borges, J. I. Elizondo, M. Machida, C. A. F. Varandas and R. M. O. Galvao, “Multipoint Thomson Scattering Diagnostic For The TCABR Tokamak With Centimeter Spatial Resolution,” *AIP Conference Proceeding,* vol. 192, p. 996, 2008.

[34] S. Xiao, A. Hu, H. Chen, X. Han, T. Wang, Q. Zang and Z. Zhao, “Analysis of baffles for stray light reduction in the Thomson scattering diagnostic on EAST,” *Fusion Engineering and Design,* vol. 105, pp. 33-38, 2016.

[35] D. G. Nilson, D. N. Hill, J. C. Evans, T. N. Calstrom, C. L. Hsieh and R. E. Stockdale, “Thomson scattering stray light reduction techniques using a CCD camera,” *Review of Scientific Instruments,* vol. 68, p. 704, 1997.

[36] D. J. Schlossberg, M. W. Bongard, R. J. Fonck, N. L. Schoenbeck and G. R. Winz, “Progress on Thomson scattering in the Pegasus Toroidal Experiment,” *Journal of Instrumentation,* vol. 8, p. C11019, 2013.

[37] R. Kumar, R. Singh and A. Kumar, “Studies on scattering of laser radiation from viewing dump in tokamak Thomson scattering system,” *Applied Physics B,* vol. 108, pp. 325-333, 2012.

[38] B. P. LeBlanc, “Thomson scattering density calibration by Rayleigh and rotational Raman scattering on NSTX,” *Review of Scientific Instruments,* vol. 79, p. 10E737, 2008.

[39] Shardanand and A. D. P. Rao, “Absolute Rayleigh scattering cross sections of gases and freons of stratospheric interest in the visible and ultraviolet regions,” National Aeronautics and Space Administration, Washington D. C., 1977.

[40] H. R. Griem, R. H. Lovberg and L. Marton, Plasma Physcis (Methods of Experimental Physics), vol. 9, Academic Press, 1970, p. 107.

[41] Y.-G. Kim, J.-H. Lee, D. Kim, M.-G. Yoo, H. Lee, Y. Hwang and Y.-S. Na, “Calibration of Thomon scattering system on VEST,” *Journal of Instrumentation,* vol. 12, p. C12013, 2017.

[42] B. Kurzan, M. Jakobi, H. Murmann and ASDEX Team, “Signal processing of Thomson scattering data in a noisy environment in ASDEX Upgrade,” *Plasma Physics and Controlled Fusion,* vol. 46, pp. 299-317, 2004.

[43] S. Lee, J.-H. Lee, I. Yamada and J. Park, “Development of a neural network

technique for KSTAR Thomson scattering diagnostics," *Review of Scientific Instruments,* vol. 87, p. 11E533, 2016.

[44] J.-S. Yoon, R. Fischer, S. Gori and J. Knauer, "Bayesian Data Analysis for Fusion Diagnostics," *Journal of the Korean Physical Society,* vol. 45, pp. 1544-1552, 2004.

[45] D. S. Sivia and J. Skilling, Data analysis: A Bayesian tutorial second edition, New York: Oxford University Press Inc., 2006.

[46] J.-H. Lee, H. Kim, I. Yamada, H. Funaba, Y.-G. Kim and D. Kim, "Research of Fast DAQ system in KSTAR Thomson scattering diagnostic," *Journal of Instrumentation,* vol. 12, p. C12035, 2017.

[47] Y. An, J. Lee, J. Jo, B. Jung, H. Lee, K. Chung, Y.-S. Na, T. Hahm and Y. Hwang, "Efficient ECH-assisted plasma start-up using trapped partical configuration in the versatile experiment spherical torus," *Nuclear Fusion,* vol. 57, p. 016001, 2017.

[48] M. W. Bongard, J. L. Barr, R. J. Fonck, J. A. Reusch and K. E. Thome, "On virial analysis at low aspect ratio," *Physcis of Plasmas,* vol. 23, p. 072508, 2016.

[49] A. Alfier and R. Pasqualotto, "New Thomson scattering diagnostic on RFX-mod," *Review of Scientific Instruments,* vol. 78, p. 013505, 2007.

[50] T. Yamaguchi, A. Ejiri, J. Hiratsuka, Y. Takase, Y. Nagashima, O. Watanabe, T. Sakamoto, T. Ohsako, B. I. An, H. Kurashina, H. Kobayashi, H. Hayashi, H. Matsuzawa, K. Yamada, H. Kakuda, K. Hanashima and T. Wakatsuki, "Development of a Thomson scattering system in the TST-2 Spherical Tokamak," *Plasma and Fusion Research,* vol. 5, p. S2092, 2010.

[51] D. W. Johnson, B. P. LeBlanc and D. L. Long, "APD detector electronics for the NSTX Thomson scattering system," *Review of Scientific Instruments,* vol. 72, p. 1129, 2001.

[52] J. Yang, Y. Kim, W. Jeong and Y. Hwang, "Simple and accurate method of diamagnetic flux measurement in Versatile Experimental Spherical Torus," *Review of Scientific Instruments,* vol. 89, p. 103508, 2018.

국문초록

VEST 장치의 톰슨 산란 진단 장치 개발

김 영 기
에너지시스템공학부
(핵융합 및 플라즈마 공학 전공)
서울대학교 대학원

VEST 장치의 중심부 플라즈마를 측정하기 위한 톰슨 산란 진단 장치를 개발하여 Ohmic 플라즈마의 전자 온도 및 밀도를 측정하였다. VEST는 국내 최초로 제작된 구형 토러스 (spherical torus) 장치로 다양한 플라즈마 시동 방법, 가열 및 전류 구동 연구를 통해 고온-고밀도의 고성능 플라즈마를 생성하기 위한 연구를 수행 중이다. VEST의 연구를 수행하기 위한 가열 장치로 electron Bernstein wave (EBW), lower hybrid fast wave (LHFW), 중성입자빔 (NBI) 등과 플라즈마 물리량의 공간 분포를 측정하기 위한 톰슨 산란 진단계, 분광기, 다채널 간섭계 등의 진단 장치들이 개발되어왔다. 본 연구에서는 가열 효율이나 플라즈마의 수송 현상을 이해하는데 가장 중요한 정보인 전자 온도와 밀도를 측정하기 위한 효율적인 톰슨 산란 진단계의 설계 및 개발에 대해 탐구하였다.

톰슨 산란 진단계는 플라즈마에 고출력의 펄스 레이저 입사시 전자에 의해

산란된 빛의 파장 변화로부터 전자의 온도를 측정하고, 진단계의 절댓값 보정이 되어있다면 빛의 세기로부터 전자 밀도를 결정한다. 특히, 톰슨 산란은 완전탄성충돌 현상이므로 탐침법이나 다른 빔 진단법들과 달리 측정 대상 플라즈마에 전혀 영향을 주지 않는다는 강점이 있다. 게다가 mm 단위의 뛰어난 공간 분해능을 갖기 때문에 대부분의 tokamak이 가동하고자 하는 진단 장치이다.

톰슨 산란 진단계는 일반적으로 레이저 입사계, 집광계, 폴리크로미터 (polychromator)로 구성되어있다. VEST의 톰슨 산란 진단계는 잘 알려진 장치들의 톰슨 산란 진단계에 비하면 상당히 낮은 에너지인 0.85 J의 레이저와 약 6천만 원의 저 예산을 사용하여 개발되었기 때문에 신중한 설계가 요구되었다. 적은 광량으로부터 충분한 신호 대 잡음비(signal-to-noise ratio, SNR)를 얻기 위해 각 부분의 성능을 극한까지 최적화하는 방법을 연구했고, 동시에 적절한 노이즈 제거를 위한 원인 분석이 수행되었다. 레이저 입사계는 Nd:YAG 레이저의 주 파장인 근적외선 1064 nm의 파장을 사용하여 파장 변환 과정에서 발생할 수 있는 에너지 손실을 피했다. 그리고 측정 목표 지점 근방에 가우시안 빔(Gaussian beam)의 레일리 범위 (Rayleigh range)가 형성되도록 광학계를 설계하여 집광계의 수집 효율을 높였다. 집광계와 폴리크로미터 개발 사이에는 제한된 예산 내에서 요구조건을 만족하기 위한 성능의 타협이 필요했다. 폴리크로미터의 파장 분해능이 높아도 수집된 광량이 모자라면 신호 해석이 불가능하므로 집광계 성능을 더

우선시하였다. 집광계는 VEST 진공 용기에 설치되었을 때 입체각이 최대가 되고, 폴리크로미터에 빛을 전달하는 과정에서 손실이 최소화 되도록 설계했다. 집광계는 유효 직경 109 mm의 대형 비구면 렌즈 2매와 코어 직경 1500 μm, 개구수(numerical aperture, NA) 0.39의 고성능 광섬유로 이루어져있다. 그리고 수집 입체각과 산란 길이의 곱이 약 300 mm msr 으로 유지되는 주반경 0.23-0.5 m 구간에서 측정이 가능하다. 폴리크로미터 내부의 광 전달부는 국가핵융합연구소 KSTAR에서 사용하는 것을 본 따서 제작하였다. 하지만 분광부의 대역 필터(band pass filter)는 측정 대상 온도 영역 1-200 eV 에 적합하도록 설계되었다. 이 때, 예산 절감을 위해 투과율과 차단율이 설계보다 낮고 투과폭의 겹침에 의해 파장 분해능도 부족한 저가의 상용 필터를 구입했다. 필터의 낮은 차단율에 의해 필터를 투과해 측정되는 레이저 파장의 미광(stray light)을 줄이기 위해 VEST 진공 용기 안팎에 미광 감소용 부품을 개발 및 설치하여 초기의 1/100배 이하로 낮추는데 성공하였다.

VEST 진공 용기에 플라즈마 대신 질소의 압력을 변화시켜가며 레일리 산란(Rayleigh scattering) 신호의 변화를 측정했고 톰슨 산란과의 산란단면적 비교를 통해 절댓값 보정을 했다. 그리고, VEST ohmic 플라즈마 발생과 톰슨 산란 진단계 사이의 시간 동기화를 위한 회로를 개발했다. 그 결과 전자 밀도가 2×10^{18} m^{-3} 이상일 때 톰슨 산란 신호를 측정할 수 있었다. 기록된 톰슨 산란 신호들은 베이지안 분석법(Bayesian analysis)을 통해 전자 온도와

밀도를 동시에 결정하였다. 전자 밀도가 2×10^{18} m^{-3} 보다 낮을 때는 1회의 측정으로는 충분한 SNR을 확보할 수 없었기 때문에 같은 조건에서 3회 이상의 누적 실험을 통해 산란신호를 얻었다. 반복적인 실험을 통해 톰슨 산란 진단계로 측정한 전자 온도와 밀도의 시간 변화가 반자성 루프(diamagnetic loop)와 평형해석을 통해 계산된 플라즈마 에너지의 변화 경향과 일관성을 나타내는 것을 확인했다.

VEST의 톰슨 산란 진단 장치는 주요 부위들의 접근성이 좋고 수정하기 쉽도록 개발하였기 때문에 부분적인 업그레이드를 통한 성능 개선을 기대할 수 있다. 우선, 계획중인 버스트 레이저(burst laser)가 기존 레이저를 대체하면 한 번의 방전에서도 1 ms 간격으로 10회 측정이 가능해지며, 에너지 증가에 의해 SNR의 증가도 뒤따를 것이다. 이 레이저 신호를 측정하기 위해서는 고속 디지타이저(digitizer)의 도입이 필요하므로 KSTAR에서 사용중인 것과 동일한 디지타이저의 설치도 계획되어있다. 추가적인 신호 향상이 필요하다면 공간 분해능을 손해 보더라도 광섬유 묶음(optical fiber bundle)을 활용할 수도 있다. 그리고, 폴리크로미터의 수가 점진적으로 증가될 것이므로 중요한 위치 위주로 반경분포가 측정될 것이다.

주요어: 톰슨 산란, 톰슨 산란 진단, 플라즈마 진단, 구형 토러스, VEST
학 번: 2012-20992